Sedimentary Architecture and Links to Carbonate Cementation in the Hibernia Formation, Hibernia Field, Offshore Newfoundland

by

© Mateo Acuna Uribe

A thesis submitted to the School of Graduate Studies in partial fulfillment of the requirements for the degree of Master of Science

Department of Earth Sciences
Memorial University of Newfoundland

August 2024

St. John's, Newfoundland and Labrador

Abstract

Carbonate cements filling intergranular pores in siliciclastic reservoirs dramatically reduce porosity and permeability, representing baffles and flow barriers that impact reservoir performance and drilling operations. Understanding the origin and controls of carbonate cementation allows deciphering and predicting carbonate-cemented intervals in the reservoir stratigraphy. Sedimentologic and diagenetic studies of the Lower Cretaceous Hibernia Formation in the Jeanne d'Arc basin, Newfoundland, Canada, were performed to test links between carbonate cements, facies associations and sea-level fluctuations. The Lower Hibernia zone records the transition from a deltaic to an estuarine environment characterized by two regressive sequence boundaries and comprising fluvial, tidal-fluvial, and tidal facies associations. Petrographic analyses revealed three main pervasive carbonate cements: early calcite, early dolomite and late ferroan calcite. The $\delta^{18}O$ ($\delta^{18}O_{calcite}$= -7.6 to -4.2 ‰ VPDB; $\delta^{18}O_{dolomite}$= -4.1 to -1.6 ‰ VPDB) and trace element geochemistry of calcite and dolomite suggest that parent fluids were influenced by mixing of marine-meteoric water under relatively reducing conditions at shallow depths. Dolomite cementation is linked with seawater retention within in sediments during sea level regressions and fluid expulsion due to compaction of the underlying shales. Conversely, calcite cements are associated with transgressions and an increased marine water flux into the recently deposited sediments. The percolation of acidic pore waters promoted the dissolution of early carbonate cements and the development of secondary porosity, predating ferroan calcite cementation. Finally, the common distribution of ferroan calcite in the overall stratigraphy, and depleted $\delta^{18}O$ composition ($\delta^{18}O_{ferroancalcite}$= -10.2 to -9.1 ‰ VPDB) and high Fe and Mn concentrations, suggests that ferroan calcite cementation occurred during early burial.

Acknowledgements

Firstly, I extend my gratitude to my supervisors, Dr. David G. Lowe, and Dr. Karem Azmy. Both, David and Karem were essential in providing invaluable feedback, guiding and support throughout the planning, presentation and writing of this entire thesis. I am grateful for their mentorship and encouragement over the past two years. Thanks to my committee member, Dr. James Conliffe for his assistance during the fluid inclusion hunting in the fall of 2021.

Thanks to Hilary Corlett for their valuable feedback and insights on carbonate cement formation. Thanks to Dylan Gouide, Dr. Markus Wälle and Bruce Barnett for their support during the data collection with the scanning electro microscope and mass spectrometry instruments at Memorial University of Newfoundland and University of Kansas. I would like to thank David Mills and Mike Walsh from the Canada-Newfoundland and Labrador Offshore Petroleum Board (C-NLOPB) for their assistance during the core examination sessions at the Core Storage and Research Centre. I also thank the Hibernia Management and Development Company (HMDC) and the School of Graduate Studies (SGS), without their financial support this project would not be feasible. Thanks to Memorial University of Newfoundland for facilitating access to petrotechnical software and graphic suites, and C-NLOPB and Natural Resources Canada for providing access to the wellbore data through the Data and Information Hub and Basin Database.

Finally, I express my sincere and heartfelt gratitude to my parents, sister, and brother for their constant support and encouragement, despite the physical distance. Their belief in me has been a constat source of motivation. I also want to thank the friends I have made at Memorial University over the past two years during my graduate studies. Their companionship, fun times and advice have made this journey more enjoyable.

Table of Contents

List of Figures

List of Tables

Chapter 1: Introduction and Overview

1.1. Motivation

Carbonate minerals are one of the most common cements in clastic reservoirs, significantly controlling porosity and permeability (Macaulay et al., 2009). Carbonate cements function as fluid flow barriers, baffles, and hard-to-drill intervals, adding complexity to hydrocarbon production, water/gas injection and drilling operations. The chemical composition of carbonate cements also has considerable implications for enhanced oil recovery (EOR) because ferroan carbonates may react with injected acid fluids and precipitate iron oxides and oxyhydroxides (Morad, 1998; Graham et al., 2020). Conversely, carbonate cements that precipitate in pore space before significant burial, preserve the intergranular porosity, and their subsequent dissolution develops high porosity and permeability trends.

Sandstone strata of the Hibernia Formation in the Hibernia field comprise the most significant reservoirs of the Jeanne d'Arc Basin (Brown et al., 1989; Magoon et al., 2005). Here, calcite, dolomite and siderite cements are crucial in influencing porosity and permeability in sandstone intervals, leading to poor reservoir quality and heterogeneity. Initial insights about the paragenesis of carbonate cements in the Hibernia Formation were addressed by Brown et al., (1989) and Hesse and Abid (1998), however the overall cement distribution across the reservoir stratigraphy and details of their timing and genesis are still poorly understood. Furthermore, our understanding of the stratigraphic and structural controls on carbonate cementation remains elusive.

This thesis aims to develop a better understating of the stratigraphic or structural controls on carbonate cements using a combined approach of facies analysis, sequence stratigraphy, petrography, and geochemistry to define links between cement formation and stratal evolution.

This aims to reduce uncertainties associated with the carbonate cementation mechanisms of the Hibernia Formation and hence predict hard-to-drill, low porosity, and permeability intervals. Additionally, the carbonate cementation model of the Hibernia Formation may be employed as an analog for carbonate cementation in clastic reservoirs in the Hibernia field and worldwide. Consequently, the primary objective of this research is to investigate the genesis of carbonate cements and their structural and stratigraphic controls in the Hibernia Formation at the Hibernia field.

1.2 Geological Background

1.2.1 North Atlantic Rift Evolution

Offshore Newfoundland and Labrador stands out as a significant hydrocarbon-producing region in Canada (Enachescu, 1987). This area is located on the Eastern Continental Margin of Canada, which developed during the Mesozoic extension that led to the opening of the Atlantic Ocean (Grant et al., 1986). The Grand Banks margin consists of a series of half-grabens bounded by listric faults that sole out along a main crustal detachment, developing failed rift basins underlying the Grand Banks region (e.g., Jeanne d'Arc and Flemish Pass basins; Figure 1). The Grand Banks was affected by three Mesozoic rift stages: (1) the Tethys rift stage (Late Triassic – Early Jurassic) coinciding with the separation of the Scotian and North African margins; (2) the North Atlantic rift or Iberia-Northern Europe rift stage (Late Jurassic – Early Cretaceous); and finally (3) the Late Cretaceous Labrador rift stage resulting in the break-up of Europe and North America (Grant et al., 1986; Enachescu, 1987; Tankard and Welsink, 1987; Sinclair, 1988; Tankard and Balkwill, 1989; Sinclair, 1992; Driscoll et al., 1995; Sinclair et al., 1999; Withjack and Schlische, 2005). During

the Late Triassic, the Tethys rift stage developed a series of northeast-southwest trending rift valleys (e.g., Jeanne d'Arc, Flemish Pass, and Orphan basins). Subsequently, the separation between the Grand Banks of Newfoundland and Iberia occurred during the North Atlantic rift stage. The transition from rift to drift during the Late Cretaceous until the Paleocene coincided with gradual regional subsidence overprinted by the deposition of multiple transgressive and regressive sequences (Arthur et al., 1982; Magoon et al., 2005). Finally, deep marine clastics, mainly mudstone, dominated the passive margin sedimentary record throughout the Cenozoic in the Grand Banks (Magoon et al., 2005).

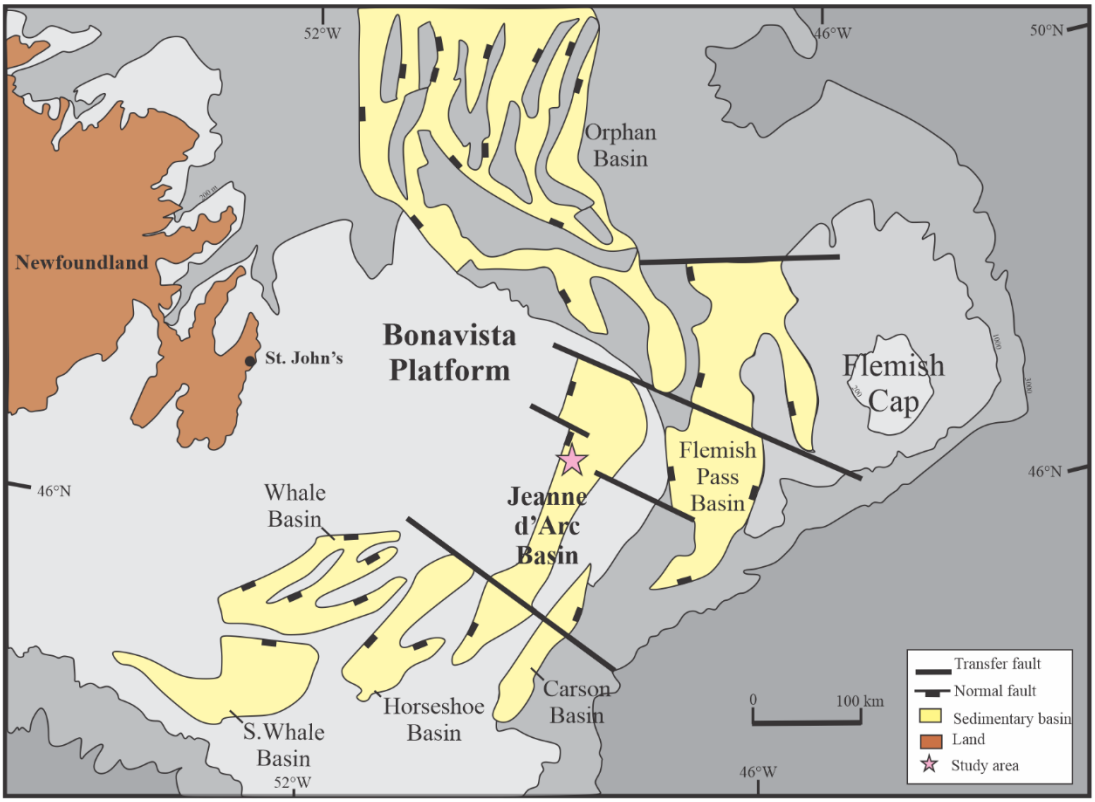

Figure 1. Location of the Jeanne d'Arc basin, Grand Banks of Newfoundland. Modified after Tankard and Welsink (1987).

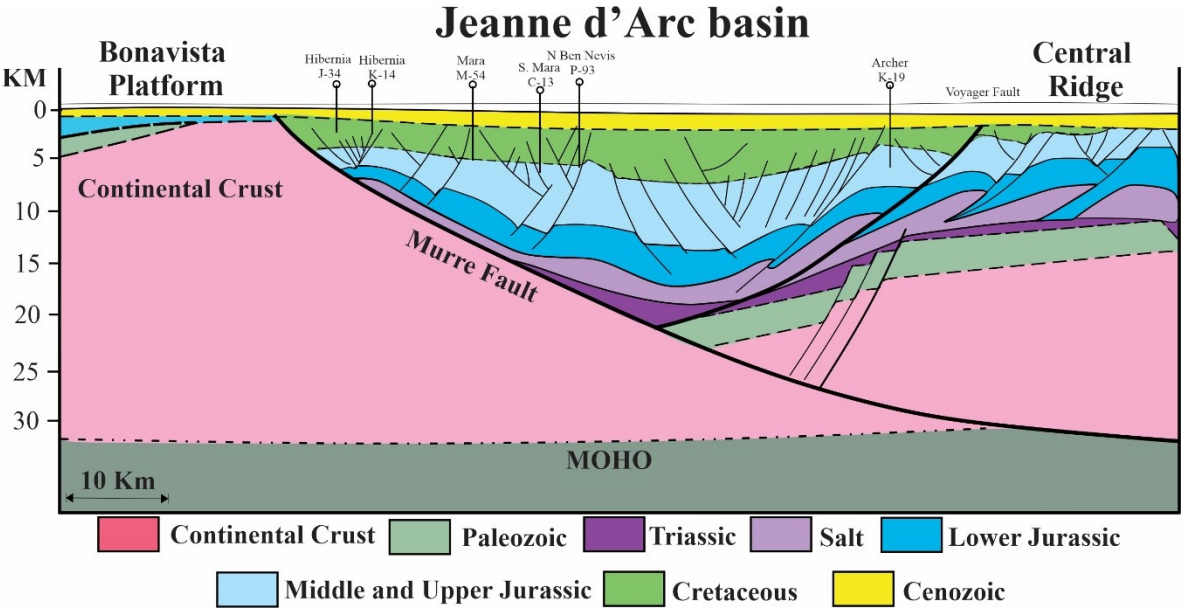

Figure 2. SW-NE cross section of the Jeanne d'Arc Basin illustrating the major structural features of the basin. Modified after Enachescu, (1987).

1.2.2 Jeanne d'Arc basin stratigraphy

The Jeanne d'Arc basin (JDB) contains the majority of the identified petroleum resources within Grand Banks basins (CNLOPB, 2022). Tankard and Welsink (1987) describe the JDB as a funnel-shaped basin, structurally characterized as a half-graben and bounded by southwest-northeast-trending listric faults. The western boundary of the basin is delineated by a primary listric detachment composed of the Murre and Mercury faults, adjacent to the Bonavista Platform (Figure 2). The eastern boundary of the basin is defined by the Voyager fault and the Central Ridge Complex (CRC), the southern boundary is constrained by the Egret fault and the northern boundary by the Cumberland Belt Transfer Zone (CBTZ) and the Orphan Basin (Enachescu and Fagan, 2005; Lethbridge, 2012; Macdougall et al., 2021).

The Jeanne d'Arc Basin is the deepest basin and preserves the most complete stratigraphic record of the interconnected rift basins beneath the Grand Banks (Figure 3; Brown et al., 1989; McAlpine,

1990). The sedimentary infill within the Jeanne d'Arc basin thickens to the north, overlying Paleozoic basement rocks of the Avalon terrane (McAlpine, 1990; Tankard and Welsink, 1987). Each major depositional sequence of the Jeanne d'Arc basin correlates with specific tectonic events of the Grand Banks region, during the evolution of the North Atlantic Ocean and the Labrador Sea (e.g., transition to passive continental margin subsidence episode and rift subsidence episodes, Figure 3) (McAlpine, 1990). The JDB sedimentary record begins with Late Triassic – Early Jurassic red beds, salt, and carbonate rocks from the Eurydice, Argo, and Iroquois Formations, respectively, all associated with the Tethys rift stage. Subsequent to the Tethys rift the deposition of the Downing, Whale Member, Voyager, and Rankin Formations took place during the Early to Late Jurassic post-rift subsidence phase (McAlpine, 1990; Sinclair, 1992). The heterogeneous Rankin Formation consists of massive limestone, mudstone, carbonate-cemented sandstone, and shale deposited in a shallow marine shelf environment with poor clastic input (McAlpine, 1990). The Late Jurassic Egret member of the Rankin Formation, an organic-rich shale, represents the primary source rock across the Grand Banks (Magoon et al., 2005; McAlpine, 1990; Tankard and Welsink, 1987).

The Tithonian - Early Valanginian period resulted in the deposition of the Jeanne d'Arc, Fortune Bay, and Hibernia Formations during the North Atlantic Rift (Sinclair, 1988, 1992). The B marker member, Catalina, and Whiterose Formations represent a regional thermal subsidence period following the Iberia-Gran Banks break-up event (Sinclair, 1988). The Avalon Formation prograded northward over the A marker member in the Barremian during a regional warping event related to the renewed arching of the Avalon Uplift area (Sinclair, 1988). The new period of crustal extension in the Aptian-Albian period (Labrador Sea rift) resulted in the deposition of the Ben Nevis and Nautilus Formations (McAlpine, 1990; Sinclair, 1988). The Jeanne d'Arc, Hibernia, Catalina, Avalon, and Ben Nevis Formations serve as the hydrocarbon-bearing reservoir units in the

Hibernia, Hebron, Terra Nova, and Whiterose oilfields of the JDB (CNLOPB, 1997; Enachescu and Fagan, 2005). The late Cretaceous – Cenozoic sedimentary record consists of interstratified shale, sandstone (Ottey May and Fox Harbour members), and limestone (Petrel and Wyandot members) of the Dawson Canyon Formation and shale of the Banquerau Formation (Sinclair, 1992).

The petroleum system of the Jeanne d'Arc Basin is known as the Egret-Hibernia system, where the Egret member serves as the primary source rock, and the sandstone units of the Jeanne d'Arc, Hibernia, Catalina and Ben Nevis Formations function as reservoir rocks. The Fortune Bay, White Rose, and Nautilus Formations are principal seal rocks. The Hibernia and Avalon Formations are the major reservoirs of the petroleum system, containing 44 and 28% of the known petroleum reserves, 969 and 620 million barrels of oil equivalent, respectively (Magoon et al., 2005). The Egret source rock generated hydrocarbons as early as 120 Ma , reaching peak petroleum generation and expulsion at about 100 Ma (Williamson, 1992; Magoon et al., 2005). Fault geometries and structural traps formed during the Aptian-Albian at approximately 100 Ma before hydrocarbon expulsion (McAlpine, 1990; Magoon et al., 2005; Richards, et al. 2010). Hydrocarbon migration occurred mainly by buoyancy of gas-saturated oil. Additionally, trans-basin faults facilitated the vertical migration of hydrocarbons to younger sandstone units in the Catalina, Avalon and Ben Nevis Formations (Magoon et al., 2005). Consequently, the largest oil pool occurs in reservoirs where the northwest-trending faults exist, parallel to the Nautilus fault (e.g., Hibernia and Hebron fields; Magoon et al., 2005).

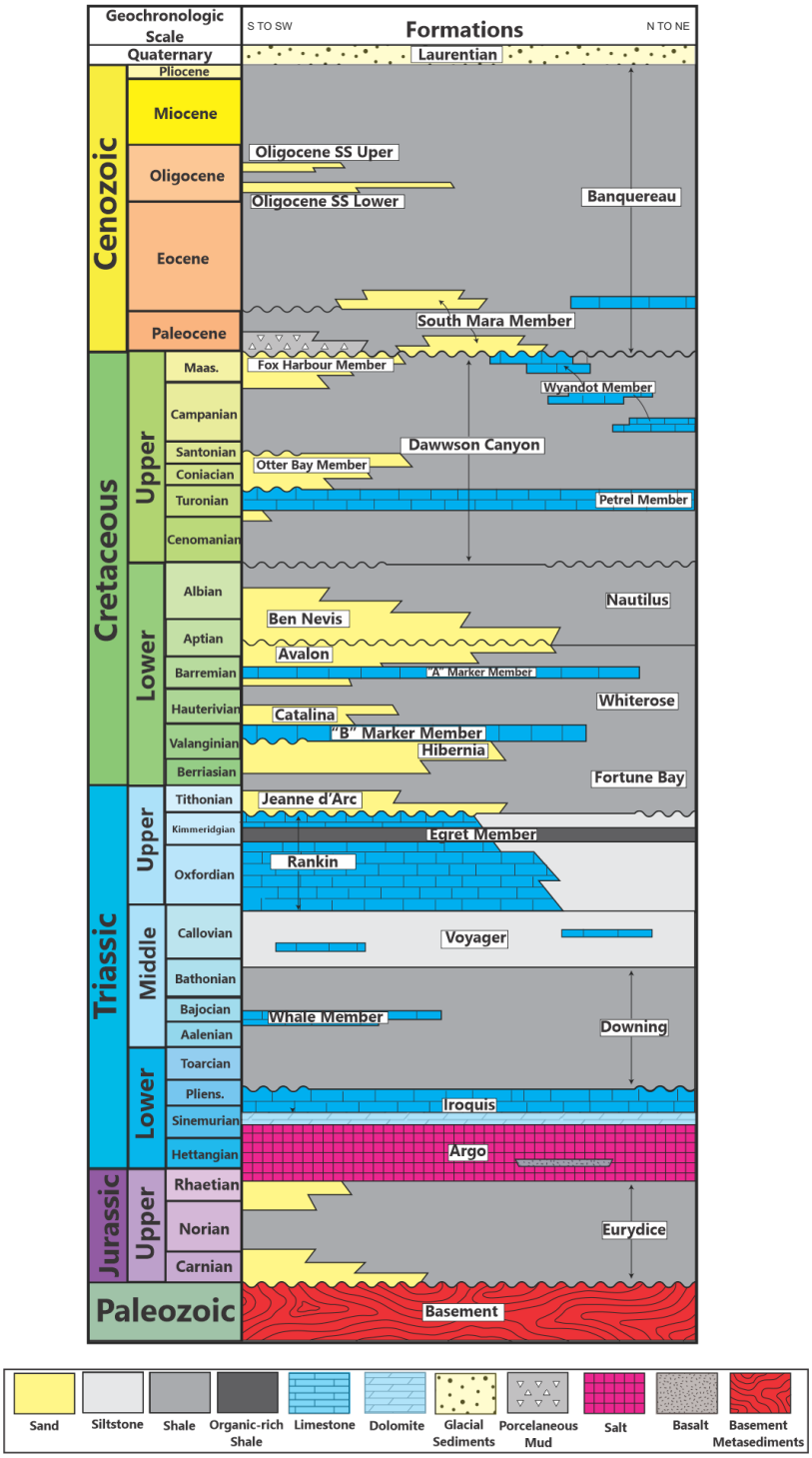

Figure 3. Lithostratigraphy of the Jeanne d'Arc Basin. Modified after Sinclair (1992).

1.2.3 Hibernia field

The Hibernia field was the first development in the Grand Banks Area, with production beginning in November 1997, employing an ice-resistant, gravity-based platform on the seabed in 80 meters of water (Arthur et al., 1982; Magoon et al., 2005; Sinclair et al., 1999). The Hibernia field has produced 1812 million barrels of crude oil as of June 2022, and reserves are 1335 million bbl (CNLOPB, 2022). The primary reservoir is the fluvio-deltaic Hibernia Formation, and the Ben Nevis, Avalon, and Catalina Formations are the secondary reservoirs. Structural traps formed within these reservoirs with the development of a fault-segmented, south-plunging rollover anticline at the intersection of the basin-bounding Murre fault and the trans-basinal Nautilus fault (Hurley et al., 1992). Salt diapirism along the Murre fault deformed the rollover anticline in its west flank (Hurley et al., 1992; Tankard and Welsink, 1987). Two sets of faults are interpreted in the Hibernia structure. The north-striking fault sets subparallel to the Murre fault and the NW-SE striking fault system parallel to the Nautilus fault (Figure 4). Sinclair et al. (1999) established three episodes of fault genesis in the Hibernia field. The normal listric Murre fault was formed in response to NW extension during the Late Triassic - Early Jurassic Tethys rift. Subsequently, the north-striking faults, subparallel, synthetic, and antithetic to the Murre fault, were formed during Late Jurassic – Early Cretaceous rifting (Hurley et al., 1992; Sinclair et al., 1999). Finally, the Late Cretaceous Labrador Sea rifting resulted in the development of the Nautilus, Rankin, and the NW-SE striking normal faults. These faults are interpreted as the main boundaries of six reservoir compartments in the Hibernia reservoir (Figure 4; Sinclair et al., 1999).

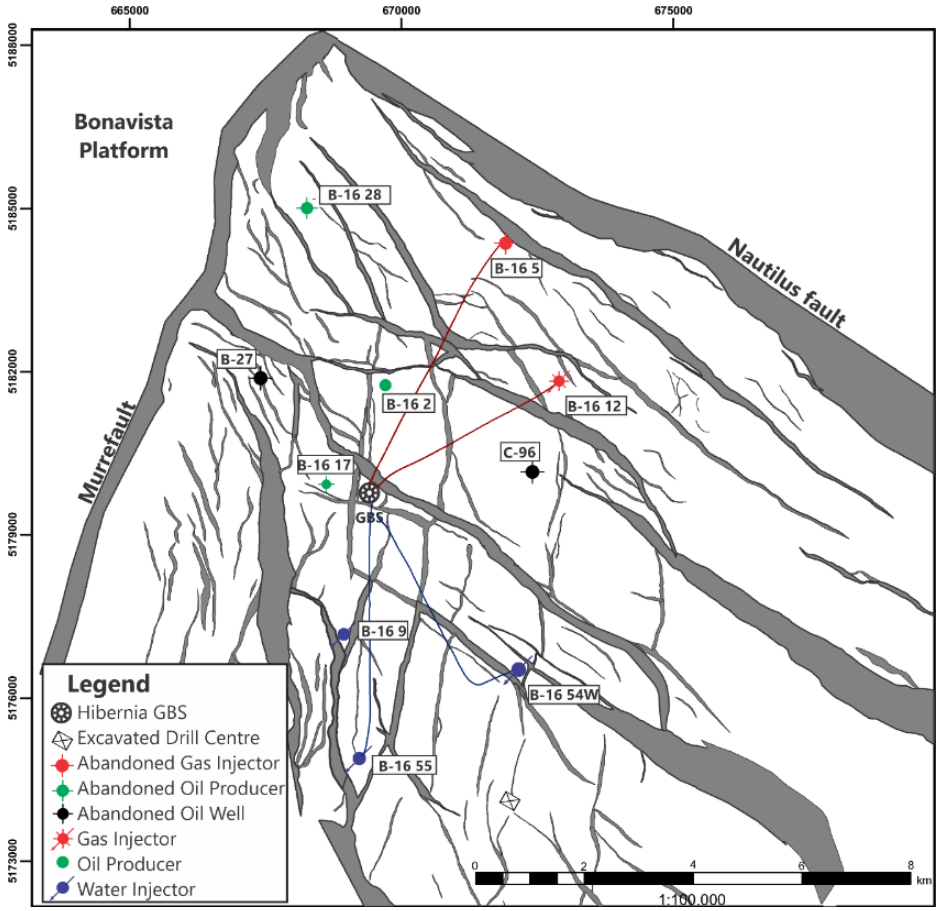

Figure 4. Location of the Hibernia fault trends at the top of the Layer 3 sandstone. Gravity based structure (GBS). Modified after CNLOPB (2021b)

1.2.4 Hibernia Formation: lithostratigraphy

The Upper Jurassic – Lower Cretaceous Hibernia Formation has been intercepted by drilling across the Jeanne d'Arc basin during the last four decades. Initially, the medium-grained and well-sorted Hibernia sandstones were described by Arthur et al. (1982) as a member of the Mississauga Formation. However, McAlpine (1990) subsequently redefined the sandstone-dominated unit overlaying the Fortune Bay Formation and underlying the White Rose Formation as the Hibernia Formation. In the Hibernia field, the thickness of the Hibernia Formation is approximately 200 meters, increasing towards the south and the west.

Brown et al. (1989) divided the Hibernia Formation into two stratigraphic members: the Main Hibernia Zone (MHZ) member and the Upper Hibernia Zone (UHZ) member. The principal reservoir strata occur in the MHZ member, also known as the Lower Unit (McAlpine, 1990) or Lower Zone (Sinclair et al., 2005). Well-sorted, medium to very coarse-grained quartz arenite defines approximately three-fourths of the MHZ member, and the remainder consists of mudstone and siltstone (Brown et al., 1998). Common carbonaceous stringers occur locally in sandstone and mudstone, consisting of fossilized plant detritus. Sedimentary structures in the sandstone include cross-stratification, planar lamination, and symmetric and asymmetric ripple stratification (Figure 5; McAlpine, 1990). Additionally, the field operator also informally divided the MHZ member into four lithostratigraphic layers (Figure 5; Sinclair et al., 2005). Layer 3 comprises incised valley-fill fluvial channel facies at the bottom of the member. The Medial Shale is a shale-dominated unit that separates Layers 2 and 3 (Sinclair et al., 2005). The sand-rich Layer 2 consists of fluvial-dominated sheet sandstone, and Layer 1 is characterized by marine delta front strata.

The UHZ Member, known as the Upper Unit by McAlpine (1990) and the Upper Zone by Sinclair et al. (2005), is composed of very fine- to medium-grained quartz arenite, interbedded with mudstone and siltstone (Brown et al., 1989). Low- to high-angle planar cross-stratification and asymmetrical ripple stratification are the most common sedimentary structures (McAlpine, 1990). Bioturbation, gastropods, ostracods, pelecypods, carbonaceous detritus, and stringers are also common. In the context of this study, the MHZ and the UHZ are referred as Lower Hibernia zone and Upper Hibernia zone, respectively.

McAlpine (1990) interpreted the Hibernia Formation sandstone and siltstone as deposits of a prograding delta fed by large fluvial systems that drained the surrounding Avalon uplift, Bonavista Platform, and Outer Ridge Complex during the Early Cretaceous subsidence of the Jeanne d'Arc

Basin. Based on sedimentary structures, petrography, and stratification, Brown et al. (1989) proposed the sedimentation environment associated with the Lower Hibernia zone as a deltaic plain, whereas the Upper Hibernia zone was deposited in a transgressive, shallow-marine upper delta-front environment.

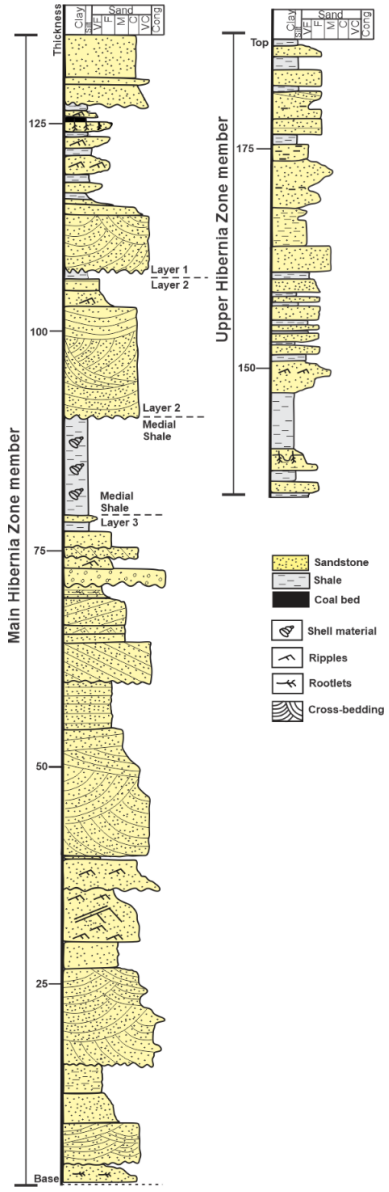

Figure 5. Generalized stratigraphic section of the Hibernia Formation. VF: Very fine, F: fine, M: Medium, C: Coarse, VC: Very Coarse, Cong: Conglomerate Modified after Brown et al. (1989).

1.2.5 Hibernia Formation: diagenesis

Sedimentary processes and tectonic deformation control fluid formation, migration, and modification in sedimentary basins (Kyser and Hiatt, 2003; Gaupp et al., 2008). Under certain conditions, carbonate-bearing fluids may precipitate carbonate minerals in pore spaces of sedimentary strata, modifying their permeability and porosity framework. Regional subsidence in the Jeanne d'Arc Basin from the Late Cretaceous until the Cenozoic resulted in the slow deposition of large volumes of sediments, burial, diagenesis, thermal maturation, and expulsion of hydrocarbons (Magoon et al., 2005). The sedimentary units of the Jeanne d'Arc basin record past fluid-rock interactions associated with hydrocarbons, super-saturated saline, and carbonate-bearing fluids.

Carbonate-cemented beds have been reported in the Hibernia, Ben Nevis and Avalon reservoir units at different locations Jeanne d'Arc Basin (Hibernia, Hebron, Terranova and Whiterose fields; Brown et al., 1989; Welsford, 1993; Fidan, 1996; Albrechtsons and Sinclair, 1997; Hesse and Abid, 1998; Normore, 2006). Olanipekun and Azmy (2022) analyzed carbonate cements in sandstone of the Jeanne d'Arc Formation in the Terra Nova field and summarized the carbonate cement paragenesis to include: (1) early near-surface dolomite cementation from seawater and meteoric porewater mixing; (2) local dolomite dissolution from acidic meteoric waters; (3) calcite cementation formed from diagenetic pore fluids prior to burial, and (4) mesogenetic dissolution of calcite cement post-dating mechanical compaction. Similarly, Hesse and Abid (1998), based on petrography and SEM analyses, proposed the paragenetic sequence of the Avalon, Ben Nevis, Catalina, and Hibernia Formations in the Hibernia field to include: (1) mechanical compaction; (2) precipitation of clay coatings of framework grains; (3) various quartz and carbonate cementation episodes, and (4) hydrocarbon migration.

Brown et al. (1989) documented in-situ ironstone concretions and siderite micro concretions of less than 1 mm, within mudstones predominantly, with a less frequent occurrence in sandstones of the Hibernia Formation. Additionally, authigenic minerals, such as quartz overgrowths, calcite, kaolinite, illite, sericite, and pyrite, occur mainly in carbonate-cemented strata. They concluded that the most common cements are quartz overgrowths and carbonate cements. The morphology of the carbonate-cemented beds in the Hibernia Formation was also described by Brown et al. as scattered patches of remnant cement to relatively well-preserved carbonate cement zones less than 1 meter thick within sandstones of the Lower Hibernia and Upper Hibernia zones. Although calcite cements become prevalent over thin reservoir intervals, constituting up to 25% of the total rock. Fidan (1996) states that the two major carbonate cements in the Hibernia Formation are siderite in very fine to lower medium-grained sandstone and calcite in carbonaceous fine-grained sandstone.

The diagenetic sequence and carbonate paragenesis of the Hibernia Formation was initially proposed by past authors (e.g., Brown et al., 1989; Hesse and Abid, 1998). The first cementation episodes involve chlorite coating and siderite precipitation, followed by the earliest quartz overgrowth and a minor pyrite cementation episode. Brown et al. suggested four possible origins of silica-rich pore fluids: (1) meteoric ground waters and dewatering of muds during initial burial; (2) deeply buried shales during the smectite-illite transition; (3) siliceous microfauna and microflora, and (4) pressure dissolution. However, the abundance of quartz overgrowth indicates that the third and fourth silica sources could be less likely to have occurred in the Hibernia Formation. Intergranular and framework grain-replacing carbonate cementation postdate silica precipitation (Brown et al., 1989). The formation of the early ferroan and non-ferroan calcite occurred during early mesogenesis prior to significant burial, as indicated by the preservation of high intergranular space and the absence of pressure solution features. Nevertheless, this early

carbonate cementation episode was not uniform throughout the Hibernia Formation. Tight siliceous-cemented and matrix-rich sandstone with reduced porosity and permeability must have impeded the infiltration of carbonate-bearing fluids (Brown et al., 1989).

According to Brown et al. (1989), carbonate cements precipitated from carbonate-saturated pore fluids that first corroded and replaced silicate minerals in the Hibernia Formation. $\delta^{13}C$ composition of early carbonate cements reported by Hesse and Abid, indicate that marine carbonate dissolution represents the main carbon source (Table 1). Furthermore, the $\delta^{18}O$ values reflect a possible influx of meteoric waters and seawater into the pore fluids and carbonate cements with $\delta^{18}O$ and $\delta^{13}C$ values near 0‰ are attributed to the dissolution of marine shells and seawater (e.g., Odigi and Amajor, 2010; García-García et al., 2013; Ma et al., 2016; Olanipekun and Azmy, 2022).

A major carbonate dissolution event generated secondary porosity, resulting in corroded grain boundaries, elongated and oversized pores, moldic porosity related to dissolved shell material, remnant patches of carbonate cements, gradational and sharp dissolution fronts. Organic matter reactions might have occurred in the Egret member before hydrocarbon expulsion around 120 Ma (Magoon et al., 2005). Consequently, decarboxylation processes and overpressure would have generated acid fluids that migrated to the upward section and promoted the dissolution of early carbonate cements (Brown et al., 1989). The second event of quartz overgrowth, grain fracturing, and minor compaction episodes occurred after the carbonate dissolution. Late ferroan calcite and late pyrite precipitated in secondary pores (Brown et al., 1989). Lighter carbon and oxygen isotopic signatures in late carbonate cements indicate precipitation at burial depths and carbon contribution from organic matter decomposition by decarboxylation processes (Table 1; Hesse and Abid, 1998). Similar $\delta^{13}C$-values between -5 to -15‰ have been reported from carbonate cements elsewhere and were attributed to thermal decarboxylation processes of organic-rich shales (Estupiñan et al.,

2007; Hodson et al., 2016; Xiong et al. 2016; Olanipekun and Azmy, 2022). Kaolinite and illite postdate the later carbonate cementation, occurring as intergranular cements and replacing altered feldspars (Brown et al., 1989). Finally, hydrocarbon migration and emplacement most likely occurred after the dissolution and cementation events in the Hibernia Formation, as evidenced by the presence of organic matter in secondary pore spaces.

Table 1. Oxygen and carbon signatures of different carbonate generation cements in the Hibernia Formation. After Hesse and Abid, (1998).

Cement Type	$\delta^{18}O$ ‰ (PDB)	$\delta^{13}C$ ‰ (PDB)
Early Calcite	-8.5 to -6.8	5.9 to -1.3
Early Dolomite	-3.6 to -2.5	-4.3 to -2.4
Late Calcite	-9.3 to -6.9	-12.3 to -7.5
Late Dolomite	-9.1	-6.1
Siderite	-6.5 to -3.9	-10.2 to -5.7

1.3 Thesis Objectives

Despite previous studies having outlined the paragenesis of authigenic minerals in the Hibernia Formation (Brown et al., 1989; Hesse and Abid, 1998), an understanding of the carbonate cement genesis and correlations with reservoir stratigraphy and sea-level fluctuations remains elusive. Stratiform re-precipitation of detrital marine biogenic carbonate could be the source of early carbonate cementation (Brown et al. 1989; Hesse and Abid, 1998; Welsford, 1993; Normore 2006; Xiong et al., 2016; Olanipekun and Azmy, 2022). Furthermore, carbonate cements may be linked to sea level fluctuations, as reported in past studies (Gibbons et al., 1993; Bakke, 1996). Early carbonate cements might precipitate in particular reservoir facies, which could be predicted by facies analysis. Additionally, the carbon source of carbonate cements and the influence of marine and meteoric waters in the carbonate-bearing fluids can be tested by petrography and stable

isotopes (e.g., Chowdhurry and Noble 1996; Colquhoun, 1998; Garcia-Garcia et al., 2013; Luan et al., 2023). Trace elements such as Mn, Fe, Mg, and Sr function as a proxy to understand the redox conditions and influence of marine water during carbonate formation (e.g., Xiong et al., 2016; Lanz et al., 2021). This work combines sedimentological, petrographic, and geochemical studies to understand the sequence stratigraphic framework, relative timing and mechanisms of carbonate cementation of the Lower Hibernia zone. Finally, carbonate cementation and pore water evolution will be linked to the sequence stratigraphic model, which will aid reservoir geologists in assessing risks associated with pervasive carbonate cementation.

The following objectives are defined for this master's thesis:

1. Define facies associations, stratal evolution and a sequence stratigraphic model of the Lower Hibernia zone.
2. Reconstruct the paragenetic sequence of the Lower Hibernia zone and propose a relative timing for carbonate cement formation.
3. Define the carbon sources and pore fluids involved in the pervasive carbonate cementation and the redox conditions of precipitation.
4. Propose hypothetical links between early carbonate cement formation and stratal and pore water evolution of the Lower Hibernia zone.

1.4 Methods and Materials

This master's thesis was developed through four progressive phases of investigation to explore the link between carbonate cements and the depositional and diagenetic history of the Lower Hibernia zone.

1.4.1 Analysis of Facies Associations

The objective of this phase was to provide a detailed description and interpretation of the reservoir facies, with a primary focus on the lithology and sedimentary structures. Subsequently, sedimentary processes and environmental conditions of sedimentation were proposed based on sedimentary facies (e.g., Dalrymple et al., 2010). Sedimentary facies were analyzed employing borehole data: conventional core, thin sections, and downhole petrophysical data. Core descriptions include lithostratigraphic logs covering key sedimentary aspects such as lithology, grain size, bedding, bedding contacts relationships, stratification, detrital composition, and biogenic structures. In addition, facies associations were proposed and linked to depositional macroforms representing unique depositional environments (e.g., fluvial bar, overbanks, interdistributary bay deposits). Finally, carbonate cements and their micromorphology were identified, including features such as massive bodies, lenses, nodules, beds, filled fractures, which were identified employing conventional cores. This process involved detailing the relationship with the stratigraphy, examining their lithological associations, mineralogy and evidence of dissolution.

1.4.2 Optical Petrography

Representative carbonate-cemented zones were sampled to examine microscopic details of their composition, texture, and paragenesis using optical and scanning electron microscopy. Polished thin sections were prepared and impregnated with blue epoxy (porosity recognition) and stained with Alizarin Red and Potassium Ferricyanide solution to facilitate the identification of carbonate cement type and iron concentrations (Lindholm and Finkelman, 1972). These thin sections were

first analyzed using a polarizing Zeiss Axioscope 5 petrographic microscope at Memorial University of Newfoundland. Observations of carbonate mineral textures, textural relationships, and authigenic mineralogy were employed to constrain the paragenetic sequence. In addition, backscattered electron imaging was used on an FEI Quanta 400 scanning electron microscope (SEM) equipped with an energy dispersive X-ray (EDX) microanalytical system (Bruker AXS, XFlash Detector 4010) at Memorial University of Newfoundland for representative mineral phase identification and characterization of detrital and authigenic fine-grained textures. Lastly, site selection for micro-sampling and trace element analysis was determined using BSE imaging to ensure precision in the investigation process.

1.4.3 Stable Isotope Analysis

In order to propose and test potential links between early carbonate petrogenesis and sedimentary environments of deposition, stable isotopes (^{13}C and ^{18}O) were employed in past studies to constrain carbonate sources and physicochemical conditions of precipitation (e.g., Hesse and Abid, 1998; Xiong et al. 2016; Ma et al., 2016; Olanipekun and Azmy, 2022). Analyzing $\delta^{13}C$ of carbonate cements, the diagenetic processes and carbon source involved during carbonate cement formation can be constrained (e.g., organic material oxidation, microbial methanogenesis, microbial sulphate reduction, fermentation, and abiotic CO_2 formation; Irwin et al., 1977; Hoefs, 2006). The $\delta^{18}O$ composition of carbonate cements provides insights into the composition of the parent carbonate fluid and an approximate precipitation temperature of carbonate cements (Hoefs, 2006). Samples with a high volume of carbonate cements were micro-drilled under a binocular microscope. Then, 75 μg of carbonate cements were reacted with orthophosphoric acid using a Thermo Scientific Kiel IV Carbonate Device interfaced to the inlet of a Thermo Finnigan MAT

253 dual inlet mass spectrometer at University of Kansas. The generated carbon dioxide was measured by its $\delta^{13}C$ and $\delta^{18}O$ signatures. The isotope ratios are calibrated relative to the VPDB scale through analysis of primary standards NBS-18 and NBS-19 and additional analysis of secondary standards TSF-1, Sigma Calcite, and 88b Dolomite. Repeated measurements of standards determined uncertainties better than 0.1‰ for analyses during each run of samples.

1.4.4 Minor and Trace Element Geochemistry

Major, minor and trace elements of carbonate cements were analyzed using a laser ablation inductive-coupled plasma mass spectrometer (LA-ICP-MS) at Memorial University trough the CREAIT network. This analytical technique provides a measurement of key trace element concentrations, such as Sr, Mn, Fe, and U. These concentrations function as proxies for carbonate parent fluids and redox conditions precipitation (e.g., Xiong et al., 2016; Lanz et al., 2021; Olanipekun and Azmy, 2022). Shale-normalized rare earth element (REE_{SN}) concentrations of carbonate cement are also employed to constrain patterns of pore fluids during carbonate precipitation (Azmy et al., 2011). In addition, this approach aids in investigating the influence of diagenetic or hydrothermal fluids in the basinal sediments, contributing to a comprehensive understanding of the processes involved during diagenesis. (e.g., Bolhar and Vankarnendonk, 2007; Olanipekun and Azmy, 2022).

1.4.5 Available data

The Canada – Newfoundland and Labrador Offshore Petroleum Board (C-NLOPB) facilitated access to the core-shed facilities and the sampling of cemented intervals. Drill cores were logged

to describe the sedimentary facies and the morphology of carbonate-cemented intervals in the Lower Hibernia zone reservoir units. Additionally, a 3D 2017 post-stack depth-migrated seismic survey and downhole petrophysical logs were obtained through the C-NLOPB.

1.5 Thesis presentation

This thesis consists of three stand-alone chapters in a manuscript style. Chapter one serves as an introduction, offering an overview of the geological background, motivation, objectives, and research methods. The second chapter, intended for submission to a peer-reviewed journal, constitutes the core of the thesis. This chapter describes and interprets sedimentary facies, facies associations, carbonate cement petrography, paragenesis, isotope and trace element geochemistry and further discusses links between carbonate cementation and reservoir facies associations. Finally, chapter three unites all the material present in the chapter one and two and summarizes the most relevant conclusions of this study.

1.6 References

Albrechtsons, E., and Sinclair, L. K. (1997). Representative Core Samples from the Hibernia and Avalon Reservoirs, Hibernia Field, Offshore Newfoundland, Canada.

Arthur, K. R., Cole, D. R., Henderson, G. G. L., and Kushnir, D. W. (1982). Geology of the Hibernia Discovery.

Azmy, K., Brand, U., Sylvester, P., Gleeson, S. A., Logan, A., Bitner, M. A. (2011). Biogenic and abiogenic low-Mg calcite (bLMC and aLMC): evaluation of seawater-REE composition, water masses and carbonate diagenesis. Chemical Geology 280, 180-190.

Bolhar, R., and Vankarnendonk, M. (2007). A non-marine depositional setting for the northern Fortescue Group, Pilbara Craton, inferred from trace element geochemistry of stromatolitic carbonates. Precambrian Research, 155(3–4), 229–250.

Brown, D. M., Mcalpine, K. D., and Yole, R. W. (1989). Sedimentology and Sandstone Diagenesis of Hibernia Formation in Hibernia Oil Field, Grand Banks of Newfoundland^ modeling constrains the interpreted time and depth of hydrocarbon generation and accumulation in the sand-stone reservoirs.

CNLOPB. (1997). Properties of Oil-Bearing Reservoirs.

CNLOPB. (2022). Petroleum Resources and Reserves Newfoundland Area. Canada Newfoundland and Labrador Offshore Petroleum Board - Report.

Driscoll, N. W., Hogg, J. R., Christie-Blick, N., and Karner, G. D. (1995). Extensional tectonics in the Jeanne d'Arc Basin, offshore Newfoundland: implications for the timing of break-up between Grand Banks and Iberia. In R. A. Scrutton, M. S. Stoker, G. B. Shimmield, and A. W. Tudhope (Eds.), The Tectonics, Sedimentation and Paleoceanography of the North Atlantic Region. Geological Society Special Publication.

Enachescu, and Fagan. (2005). Call for Bids 2005 NL05-01.

Enachescu, M. E. (1987). Sedimentary Basins and Basin-Forming Mechanisms. In Memoir (Vol. 12). Canadian Society of Petroleum Geologists.

Estupiñan, J., Marfil, R., Delgado, A., and Permanyer, A. (2007). The Impact of carbonate cements on the reservoir quality in the Napo Fm sandstones (Cretaceous Oriente Basin, Ecuador) The impact of carbonate cement on the Napo Cretaceous sandstones. Geologica Acta, 5, 89–107.

Fidan, E. (1996). Reservoir Characterization of the Hibernia Formation, Jeanne d'Arc Basin, Gran Banks, Newfoundland. Memorial University of Newfoundland.

García-García, F., Marfil, R., De Gea, G. A., Delgado, A., Kobstädt, A., Santos, A., and Mayoral, E. (2013). Reworked marine sandstone concretions: A record of high-frequency shallow burial to exhumation cycles. Facies, 59(4), 843–861.

Gaupp, R., Moller, P., Luders, V., di Primio, R., and Littke, R. (2008). Fluids in sedimentary basins: an overview.

Grant, A. C., McAlpine, K. D., and Wide, J. A. (1986). The Continental Margin of Eastern Canada: Geological Framework and Petroleum Potential. In M. T. Halbouty (Ed.), Future Petroleum Provinces of the World. AAPG Memoir.

Hesse, R., and Abid, I. A. (1998). Carbonate cementation-the key to reservoir properties of four sandstones levels (Cretaceous) in the Hibernia Oilfield, Jeanne d'Arc Basin, Newfoundland, Canada. Spec. Publs Int. Ass. Sediment., 26, 636–393.

Hodson, K. R., Crider, J. G., and Huntington, K. W. (2016). Temperature and composition of carbonate cements record early structural control on cementation in a nascent deformation band fault zone: Moab Fault, Utah, USA. Tectonophysics, 690, 240–252.

Hoefs, J. (2006). Stable Isotope Geochemistry (6th Edition). Springer.

Hurley, T. J., Kreisa, R. D., Taylor, G. G., and Yates, W. R. L. (1992). The Reservoir Geology and Geophysics of the Hibernia Field, Offshore Newfoundland.

Irwin, H., Curtis, C., and Coleman, M. (1977). Isotopic evidence for source of diagenetic carbonates formed during burial of organic-rich sediments. Nature, 269(5625), 209–213.

Kyser, K., and Hiatt, E. E. (2003). Fluids in sedimentary basins: An introduction. Journal of Geochemical Exploration, 80(2–3), 139–149.

Lanz, M. del R., Azmy, K., Cesaretti, N. N., and Fortunatti, N. B. (2021). Diagenesis of the Vaca Muerta Formation, Neuquén Basin: Evidence from petrography, microthermometry and geochemistry. Marine and Petroleum Geology, 124.

Lethbridge, G. D. (2012). A Geological Model of the Hibernia Formation in the Vicinity of the Terra Nova and Hebron Field [MSc thesis]. Memorial University of Newfoundland.

Lindholm, R. C., and Finkelman, R. B. (1972). Calcite Staining: Semiquantitative Determination of Ferrous Iron. Journal of Sedimentary Research, 2(1), 239–242.

Ma, B., Cao, Y., Wang, Y., and Jia, Y. (2016). Origin of carbonate cements with implications for petroleum reservoir in Eocene sandstones, northern Dongying depression, Bohai Bay Basin, China. Energy Exploration and Exploitation, 34(2), 199–216.

Macaulay, C., Fallick, A. E., Mclaughlin, O., Haszeldine, R., and Pearson, M. (1998). The Significance of 13C of Carbonate Cements in Reservoir Sandstones: A Regional Perspective from the Jurassic of the Northern North Sea (Vol. 26, pp. 395–408).

Macdougall, M. D. J., Braun, A., and Fotopoulos, G. (2021). Evidence of lithospheric boudinage in the grand banks of newfoundland from geophysical observations. Geosciences (Switzerland), 11(2), 1–20.

Magoon, L. B., Hudson, T. L., and Peters, K. E. (2005). Egret-Hibernia(!), a significant petroleum system, northern Grand Banks area, offshore eastern Canada. American Association of Petroleum Geologists Bulletin, 89(9), 1203–1237.

McAlpine, K. D. (1990). Mesozoic stratigraphy, sedimentary evolution, and petroleum potential of the Jeanne d'Arc Basin, Grand Banks of Newfoundland. Geological Survey of Canada.

Odigi, M. I., and Amajor, L. C. (2010). Geochemistry of carbonate cements in Cretaceous sandstones, southeast Benue Trough, Nigeria: Implications for geochemical evolution of formation waters. Journal of African Earth Sciences, 57(3), 213–226.

Olanipekun, B., and Azmy, K. (2022). Carbonate cementation in the Tithonian Jeanne d'Arc sandstone, Terra Nova Field, Newfoundland: Implications for reservoir quality evolution. Sedimentology, 69(2), 461–500.

Richards, F. W., Vrolijk, P. K., and Gordon J. D. (2010). Reservoir connectivity analysis of a complex combination trap: Terra Nova Field, Jeanne d'Arc Basin, Newfoundland, Canada. Geological Society, London, Special Publications, 347(1), 333-355.

Sinclair, I. K. (1988). Evolution Of Mesozoic-Cenozoic Sedimentary Basins in The Grand Banks Area of Newfoundland and Comparison with Falvey's (1974) Rift Model. Bulletin Of Canadian Petroleum Geology, 36(3).

Sinclair, I. K. (1992). Tectonism: the dominant factor in mid-Cretaceous deposition in the Jeanne d'Arc Basin, Grand Banks. Marine and Petroleum Geology.

Sinclair, I. K., Evans, J. E., Albrechtsons, E. A., and Sydora, L. J. (1999). The Hibernia Oilfield-effects of episodic tectonism on structural character and reservoir compartmentalization. In A. J. Fleet and S. A. R. Boldy (Eds.), Petroleum Geology of the Northwest Europe: Proceedings of the 5th Conference (pp. 517–528). Geological Society.

Sinclair, I. K., Flint, S., Stokes, R., and Bidgood, M. (2005). Hibernia Formation (Cretaceous) Sequences and Breathitt Group (Pennsylvanian) Analogue-Implications for Reservoir Compartmentalization and Modelling, Offshore Newfoundland.

Tankard, A. J., and Balkwill, H. R. (1989). Extensional Tectonics and Stratigraphy of the North Atlantic Margins: Introduction: Chapter 1.

Tankard, A., and Welsink, H. J. (1987). Extensional Tectonics and Stratigraphy of Hibernia Oil Field, Grand Banks, Newfoundland. The American Association of Petroleum Geologist Bulletin, 71(10).

Williamson, M. A. (1992). The subsidence, compaction, thermal and maturation history of the Egret Member source rock, Jeanne d'Arc Basin, offshore Newfoundland. Bulletin of Canadian Petroleum Geology, 40(2), 136-150.

Withjack, M. O., and Schlische, R. W. (2005). A Review of tectonic events on the passive margin of Eastern North America.

Xiong, D., Azmy, K., and Blamey, N. J. F. (2016). Diagenesis and origin of calcite cement in the Flemish Pass Basin sandstone reservoir (Upper Jurassic): Implications for porosity

Chapter 2: Carbonate cement genesis and links to siliciclastic environments of deposition: Hibernia Formation, Jeanne d'Arc Basin, offshore Newfoundland.

2.1 Introduction

Primary porosity and permeability are typically a function of the grain size and sorting of sandstones, reflecting the sedimentary processes and conditions of sedimentation (Molenaar, 1998). Permeability and porosity may be affected by post-depositional processes that occur during diagenesis, such as cementation. Authigenic carbonates are among the most common cements in shallow-marine sandstones and cemented beds may affect the internal connectivity of a reservoir, leading to compartmentalization and higher-pressure intervals (Hesse and Abid, 1998; Morad, 1998). Carbonate cemented beds also represent hard-to-drill intervals impacting drilling operations. Additionally, their chemical composition has considerable implications for enhanced oil recovery due to the cyclic CO_2 injection that might dissolve calcite, dolomite, and siderite (Worden and Smith, 2004). Iron-rich carbonate cements may react with injected acid fluids and precipitate iron oxides and oxyhydroxides in the pore throats (Morad, 1998). On the other hand, early carbonate cements may retain high intergranular volumes, and their dissolution develops significant porosity and permeability trends (Hesse and Abid, 1998). Therefore, the distribution patterns and genesis of carbonate cements in siliciclastic reservoirs play an essential role in their quality evaluation and prediction.

Carbonate cementation is a common diagenetic feature in cretaceous shallow-marine reservoirs of the JDB, such as the Hibernia, Catalina and Ben Nevis formations (Brown et al., 1989; Fidan, 1996;

Hesse and Abid, 1998; Normore, 2006; Olanipekun and Azmy, 2022).Past studies reported the presence of carbonate cements filling intergranular porosity and leading to permeability reduction at various intervals of the Hibernia Formation in the Hibernia field (Brown et al., 1989; Hesse and Abid, 1998). However, details about the genesis of carbonate cements, distribution patterns and stratigraphic and structural controls are still poorly understood.

This study aims to elucidate the morphology, mineralogy and geochemical composition of carbonate cements and the factors that control their distribution in the fluvial and shallow-marine sandstones of the Hibernia Formation. This multidisciplinary approach employs sedimentary facies associations, optical and analytical petrography, stable isotope analysis and trace elements geochemistry to constrain the relative timing and physicochemical conditions of cement precipitation. Furthermore, facies associations analysis and sequence stratigraphy are used to constrain changes in the environment of deposition over time and their relationships with near-surface pore fluid conditions. This combined approach can provide valuable insights into the controls on carbonate cement distribution in the Hibernia Formation and shallower cemented reservoirs at Hibernia by linking stratigraphy with early cement formation. The specific objectives of this study are: (1) to define facies associations, stratal evolution and a sequence stratigraphic model of the Lower Hibernia zone, (2) to reconstruct the paragenetic sequence of the Lower Hibernia zone and propose a relative timing for carbonate cement cementation, (3) Define the carbon sources and pore fluids involved in the pervasive carbonate cementation and the redox conditions of precipitation, and (4) propose hypothetical links between early carbonate cement formation, pore water evolution and stratal evolution.

2.2 Geological Framework

Offshore Newfoundland is a significant hydrocarbon-producing region located on Canada's Eastern passive continental margin (Enachescu, 1987). The Grand Banks of Newfoundland consists of a series of half-grabens bounded by listric faults that sole out along a main crustal detachment, developing failed half-graben rift basins such as the Jeanne d'Arc and Flemish Pass basins. These basins record the evolution of the Newfoundland-Ibera magma-poor rift system formed during the opening of the North Atlantic Ocean. Three main Mesozoic rift stages characterize the Newfoundland continental margin: (1) the Late Triassic – Early Jurassic Tethys rift stage, coinciding with a series of northeast-southwest trending rift valleys (e.g., Jeanne d'Arc, Flemish Pass and Orphan Basins) and culminating in the separation of the Scotian and North African margins; (2) the Late Jurassic – Early Cretaceous North Atlantic rift or Iberia-Northern Europe rift stage culminating in the separation between the Grand Banks of Newfoundland and Iberia; and finally (3) the Late Cretaceous Labrador rift stage resulting in the breakup of Europe and North America (Grant et al., 1986; Enachescu, 1987; Tankard and Welsink, 1987; Tankard and Balkwill, 1989; Sinclair, 1988, 1992; Driscoll et al., 1995; Sinclair et al., 1999; Withjack and Schlische, 2005b).

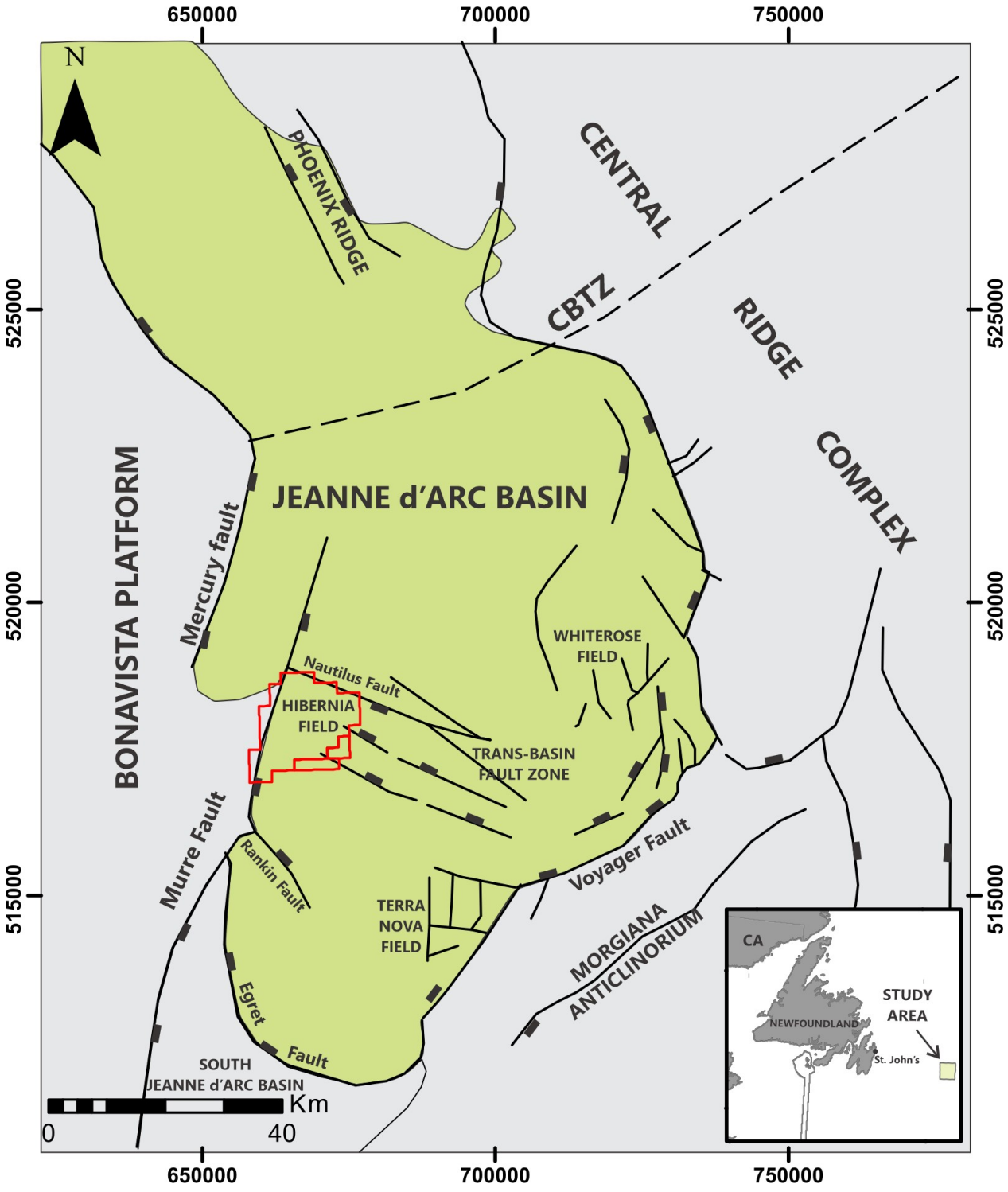

Figure 6. Location of the Hibernia field in the Jeanne d'Arc basin. Modified after Baur et al., (2009).

The Jeanne d'Arc Basin is located approximately 300 km southeast of St. John's in the Grand Banks of Newfoundland (Figure 6). It contains up to 18 km of syn-rift and post-rift strata and most of the known petroleum resources of all the Grand Banks basins (Enachescu, 1988; CNLOPB, 2022). Tankard and Welsink (1987) describe the JDB as a funnel-shaped half-graben bounded by the northeast-trending Murre and Mercury faults, a composite listric detachment that bounds the JDB west to the east against the unextended Bonavista Platform (Figure 6). The JDB is bounded to the east by the Voyager fault and Central Ridge Complex (CRC), to the south by the Egret fault, and to the north by the Cumberland Belt Transfer Zone (CBTZ) and the Orphan Basin (Enachescu and Fagan, 2005; Lethbridge, 2012; Macdougall et al., 2021).

The Hibernia oilfield was the first development in the JDB, with production beginning in November 1997, employing an ice-resistant, gravity-based platform on the seabed in 80 meters of water (Arthur et al., 1982; Sinclair et al., 1999; Magoon et al., 2005). The Hibernia field has produced 1812 million barrels of crude oil as of June 2022, and reserves are 1335 million bbl (CNLOPB, 2022). Structural traps of the Hibernia oilfield include fault segments of a south-plunging rollover anticline at the intersection of the basin-bounding Murre fault and the trans-basinal Nautilus fault (Figure 3; Hurley et al., 1992). Two sets of normal faults are interpreted in the Hibernia structure, a set of north-striking faults subparallel to the Murre fault, and NW-SE-striking faults parallel to the Nautilus fault. Sinclair et al. (1999) established three episodes of fault genesis in the Hibernia field. The normal listric Murre fault was formed in response to NW extension during the Late Triassic - Early Jurassic Tethys rift stage. Subsequently, the north-striking faults, subparallel, synthetic, and antithetic to the Murre fault, were formed during Late Jurassic – Early Cretaceous rifting of the North Atlantic rift stage (Hurley et al., 1992; Sinclair et al., 1999). Finally, the Late Cretaceous Labrador Sea rifting resulted in the development of the Nautilus,

Rankin, and the NW-SE-striking normal faults. The primary reservoir is the basal sandstone intervals of the Hibernia Formation. The secondary reservoirs are Ben Nevis/Avalon and Catalina Formations (Figure 7).

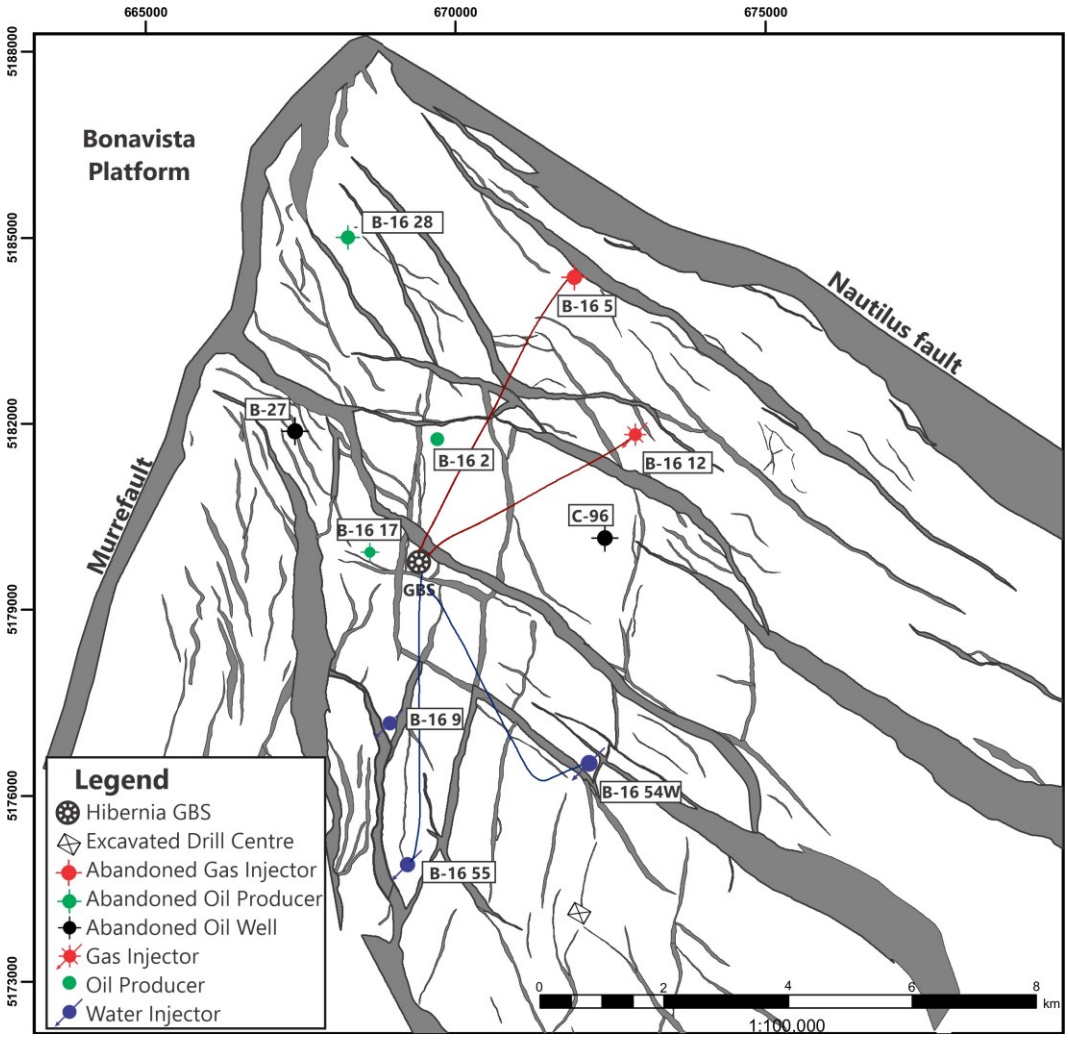

Figure 7. Location of the delineation/development wellbores employed for the present study at the top of the L3b sandstone. GBS: Gravity Base Structure. Modified after CNLOPB (2021)

The Lower Cretaceous Hibernia Formation is the primary target at the Hibernia oilfield, and it has also been intercepted across the JDB during the last four decades. The Hibernia Formation is stratigraphically divided into two members or zones: the Upper Hibernia zone and the Lower Hibernia zone (Brown et al., 1989; McAlpine, 1990; Sinclair et al., 2005). The main reservoir strata

occur in stacked fluvial channels of the Lower zone, which are mostly composed of well-sorted, medium to very coarse-grain quartz arenite. The sandstone beds display various sedimentary structures, such as cross-stratification, planar lamination, and symmetric and asymmetric ripple stratification. The Lower Hibernia zone was deposited in a prograding deltaic plain environment fed by large fluvial systems that drained the surrounding Avalon uplift, Bonavista Platform and the Outer Ridge Complex during the Early Cretaceous subsidence of the Jeanne d'Arc basin (Brown et al., 1989; McAlpine, 1990). As the rate of sea level rise outpaced dwindling sediment supply to the JDB, the Hibernia delta was transgressed leading to the accumulation of shallow marine strata (McAlpine, 1990).

The Lower Hibernia zone was further subdivided into five informal lithostratigraphic layers or reservoir units (Sinclair et al. 2005; Figure 8B). The basal layer, termed Layer 4 (L4), is a 5-10 meters thick heterolithic interval consisting of both sandstone and siltstone. Layer 4 is succeeded by a 70-90 meters thick succession consisting of well-sorted coarse- to medium-grained sandstone interbedded with massive and planar laminated siltstone, named Layer 3 (L3). The Medial Shale (MS) is a 10-15 meters thick mudstone dominated unit, separating Layer 3 and Layer 2 (Figure 8B). The 40-45 m thick sand-rich Layer 2 consists of sandstone, while the overlying Layer 1 is characterized by a 40-50 m thick succession of fine-grained sandstone interbedded with planar and wavy-laminated siltstone with rare coal beds.

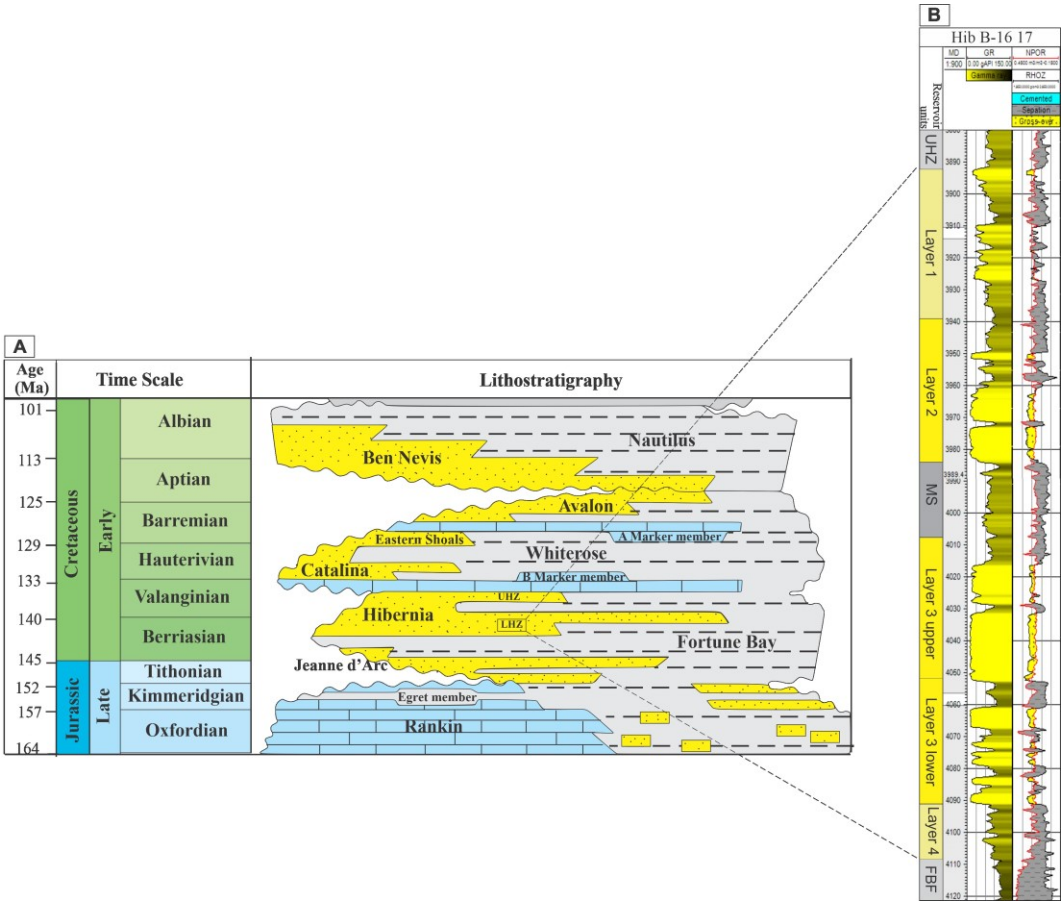

Figure 8. A) Late Jurassic to Upper Cretaceous Lithostratigraphy of the Jeanne d'Arc basin. B) Reservoir units of the Lower Hibernia zone. Upper Hibernia zone (UHZ), Lower Hibernia zone (LHZ). Modified after Johns-Buss et al (2021).

2.3 Methodology

2.3.1 Facies associations analysis

Conventional cores acquired from the Lower Hibernia zone in delineation and development wellbores across the Hibernia field (Hibernia B-16 2, B-16 28, B-16 12, B-16 5, B-16 9, B-16 54W, B-16 55, B-16 17, C-96 and B-27; Figure 7) were logged to analyze sedimentary facies including lithology, bedding, stratification, and biogenic structures. Core logging was also employed to assess the macromorphology of carbonate cements. Corresponding well logs (gamma-

ray, density and neutron porosity) were provided by the Canada Newfoundland and Labrador Offshore Petroleum Board (C-NLOPB).

2.3.2 Carbonate cement and sandstone petrography

Forty-four samples of carbonate-cemented layers were selected and cut into polished thin sections of 35 μm, and seven samples were further selected for Scanning Electron Microscope-Mineral Liberation Analysis (SEM-MLA). Polished thin sections were impregnated with blue epoxy to visualize porosity spaces. Selected thin sections were also stained with Alizarin Red-S and Potassium Ferricyanide solution for calcite/dolomite differentiation (Lindholm and Finkelman, 1972). Thin sections were petrographically examined under a Zeiss Axioscope 5 polarizing microscope to identify mineral phases and diagenetic features. Percentages of framework grains and authigenic cement were estimated based on point counting (< 300 points) following the Gazzi-Dickinson method and MLA analysis. Seven representative samples were selected for quantitative mineral liberation analysis (MLA) using an FEI Quanta 400 scanning electron microscope (SEM) equipped with an energy dispersive X-ray (EDX) microanalytical system (Bruker AXS, XFlash Detector 4010) at Memorial University of Newfoundland. The MLA analysis stands on the energy dispersive fingerprint for each mineral, which is compared against the MLA database of stored EDX spectra, with a matching threshold of 70% in the MLA software (Wilton et al., 2017). The energy dispersive X-ray (EDS) and element mapping techniques were used to recognize the carbonate mineral phases, microtextures, cement abundance and laser spot selection.

2.3.3 Carbon and Oxygen isotopes

Carbonate cement samples of approximately 75 μg were extracted from polished slabs using a hand-held micro drill under a binocular microscope. Prior to sample extraction, areas for C- and O-analyses were carefully selected in polished slab by analyzing those areas in thin sections to prevent sampling contamination in areas where more than one carbonate cement phase coexists. Stable isotopes analyses were carried out at the University of Kansas. The powdered samples were reacted with 100% H_3PO_4 using a Thermo Scientific Kiel IV Carbonate Device interfaced to the inlet of a Thermo Finnigan MAT 253 dual inlet mass spectrometer where the generated CO_2 was measured for its $\delta^{13}C$ and $\delta^{18}O$ compositions (Table 3). The isotope ratios are calibrated relative to the VPDB scale through analysis of primary standards NBS-18 and NBS-19 and additional analysis of secondary standards TSF-1, Sigma Calcite, and 88b Dolomite with uncertainties better than 0.1‰ .

2.3.4 Elemental Geochemistry

For elemental analyses (Table 5), representative cement phases were ablated for minor and trace elements concentrations, including Mn, Fe, Mg, Sr, U, and REE, using a Thermo-Finnigan ELEMENT XR high-resolution magnetic sector inductively coupled plasma mass spectrometer equipped with GEOLAS 193 nm excimer laser system. A beam diameter of 40 μm was employed during the cement ablation and a smaller beam size (20 μm) was used for some small siderite or dolomite crystals. REE concentrations are normalized to the Post-Archean Australian Shale (PAAS; McLennan, 1989). Cerium anomalies were calculated based on the equation of Lawrence et al. (2006): (Ce/Ce* = $(Ce \ / \ 79.6)/(([Pr \ / 8.83]\text{^}2) \ / \ [Nd \ / 33.9])$.

2.4 Results

2.4.1 Facies associations

Facies Association 1

Facies association 1 corresponds with Layer 1 and consists of a coarsening-upward succession composed of massive muddy siltstone that passes upward through wave ripple cross-stratified sandstone interbedded with siltstone and is capped by very thick inversely graded sandstone (Figure 9). The structureless muddy siltstone lies at the bottom of the FA1 and contains abundant shell debris and siderite patches. High bioturbation intensity (BI 4-5; Taylor and Goldring, 1993) is characterized by the abundant traces of *Chondrites* (Figure 10A) and gradually becomes less bioturbated towards the top with a higher abundance of traces*: Chondrites, Planolites, Rosselia Rotatus, Asterosoma* and *Zoophycos* (Figure 10B). Wave ripple cross-stratified very fine-grained sandstone forming 20 to 30 cm thick cosets overlie the bioturbated mudstone and is interbedded with massive siltstone beds (5-10 cm thick) with sporadic thin sandy lenses (1-5 cm thick) and convoluted laminations. Traces of *Thalasionaides, Arenicolites and Helminthopsis* commonly occur in sandy lenses within the siltstone beds (BI: 2-3; Figure 10C). Capping the facies association are 50 to 200 cm thick, inversely graded, fine- to medium-grained structureless sandstone beds with planar irregular basal contacts (Figure 10D). This structureless sandstone caps the wave ripple cross-stratified sandstone towards the top of the succession. This facies association occurs at the base of the Lower Hibernia zone and was measured in the Hibernia B-16 17 and B-16 55 cores. The coarsening-upward succession of FA1 overlies shale and sandy siltstones of the fine-grained prodelta/delta front deposits of the Fortune Bay Formation (McAlpine, 1990).

FA1 Interpretation: Delta Front

The FA1 stratigraphic position above prodelta fines, the gradational nature of the basal contact (McAlpine, 1990), coarsening-upward trend, massive stratification in beds, marine fossils, and trace fossils with low bioturbation indices suggest that FA1 was deposited in a delta-front environment where sediment from river mouths was rapidly deposited into a shallow marine environment. Structureless sandstone beds are interpreted as proximal mouth bars deposited during rapid deposition of water-saturated sediment or hyperpycnal flows from river mouths (Mulder and Alexander, 2001; Mulder et al., 2003; Bhattacharya, 2006). Ripple-cross-laminated sandstone interbedded with planar-laminated siltstone near the base of FA1 represents distal mouth bars, where subcritical unidirectional currents with low near-bed sediment concentrations transport and rework sediment (Olariu and Bhattacharya, 2006). Bioturbated muddy siltstones at the bottom of FA1 are interpreted as delta-front fines deposited beyond the reach and on the fringes of mouth bars. The trace fossil assemblage of FA1 corresponds to *Cruziana* Ichnofacies based upon the occurrence of vertical and inclined traces developed by suspension and deposit feeders, which is also characteristic of high-energy foreshore-to-shoreface environments (MacEachern et al., 2005).

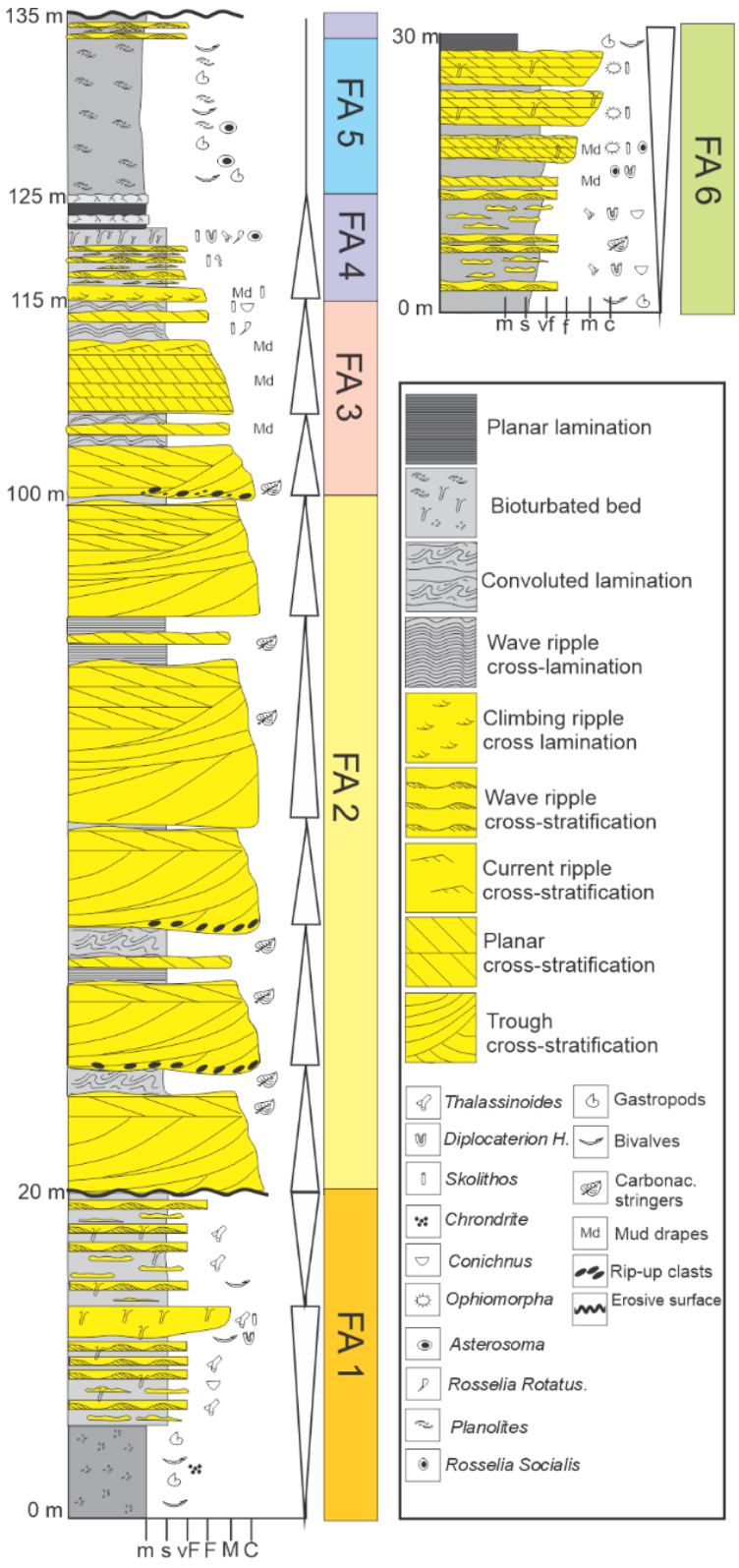

Figure 9. Schematic and generalized stratigraphic section for the Lower Hibernia zone facies associations.

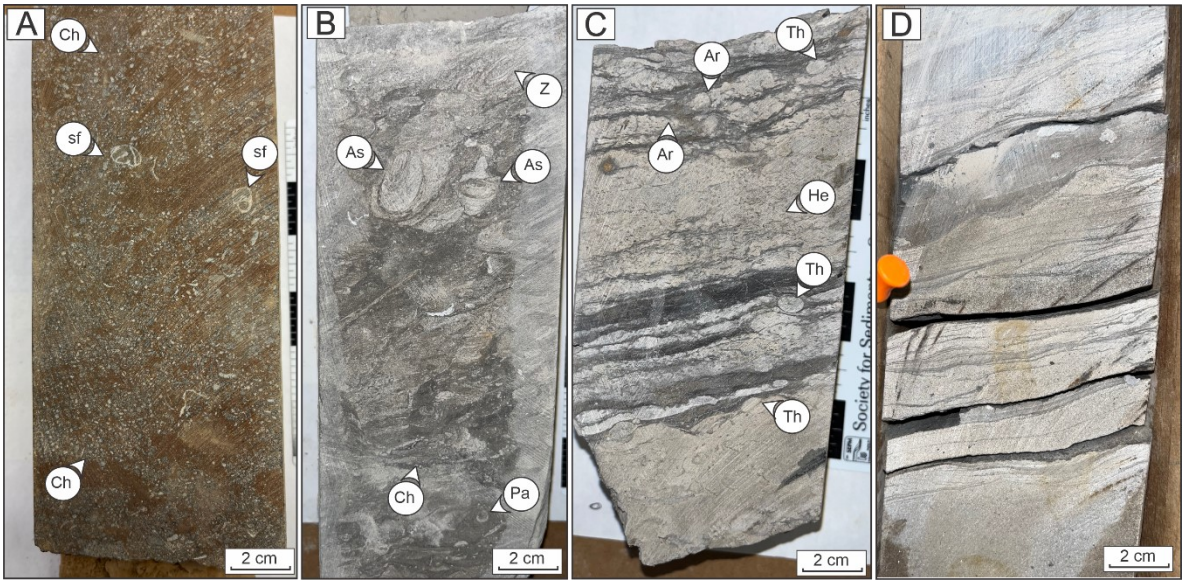

Figure 10. Core photographies of Facies Association 1 (FA1): A-B) Bioturbated muddy siltstone; C-D) Wave ripple cross-stratified very fine-grained sandstone interbedded with massive siltstone. Note the absence of bioturbation abundance and in (D) which correspond to the upper section of the FA1. Arenicolites (Ar), Chondrites (Ch), Asterosoma (As), Planolites (Pa), Thalassinoides (Th), Helminthopsis (He),Zoophycos (Z), shell fragment (sf).

Facies Association 2

The sand-rich Facies Association 2 corresponds with Layer 3 Lower (L3L) and is dominated by stacked, 5-20 meters-thick, erosively based fining-upward cycles of sandstone, each capped by massive and planar laminated sandy siltstone beds (Figure 9). Trough cross-stratified, coarse- to medium-grained sandstone forming 25-50 cm thick sets is the main component of the fining-upward cycles. Basal pebble lags are common at the base of cycles, and bioturbation is generally absent. Planar cross-stratified fine- to medium-grained sandstone with sharp-based 10-20 cm sets gradationally overly through cross-strata, where rare pebble clay clasts and abundant plant detritus occur along the base of sets. Massive and planar laminated sandy siltstone occurs at the top of the fining-upward cycles, forming 0.2 to 8 m thick beds, with localized soft sediment deformation, fluid-scape structures, carbonaceous stringers (20 – 50 mm thick; Figure 11). Bioturbation and fossils are generally absent in this facies association.

FA2 interpretation: Braided Fluvial

The widespread occurrence of medium- to coarse-grained, trough cross-stratified sandstone records sustained high-energy shallow subaqueous unidirectional flow conditions. This, along with a lack of fossils and paucity of bioturbation, is interpreted to record braided river sedimentation (e.g., Miall, 1977, 1996, 2010; Ethridge, 2011). Cyclic, fining-upward successions of trough and planar cross-strata that evolve upward to planar cross-strata represent amalgamated channel-filling braid bar deposits (Miall, 1980; Bridge and Lunt, 2009). Scours and rip-up mud clasts record erosional scouring at the deeper parts of fluvial channels. Channels were continuously shifted laterally as sediment was deposited and eroded, creating frequent scour bases and the characteristic stacking pattern evidenced in the gamma-ray response (Figure 16). Planar laminated and massive siltstone with plant detritus and absence of bioturbation and shell debris records overbank sedimentation (e.g., Miall, 1994). In summary, FA2 exhibits frequent scour bases and multiple channel-filling bar deposits, which reflects the frequent channel shifts, sediment reworking, extensive sediment deposits, and high sediment load of a braided river.

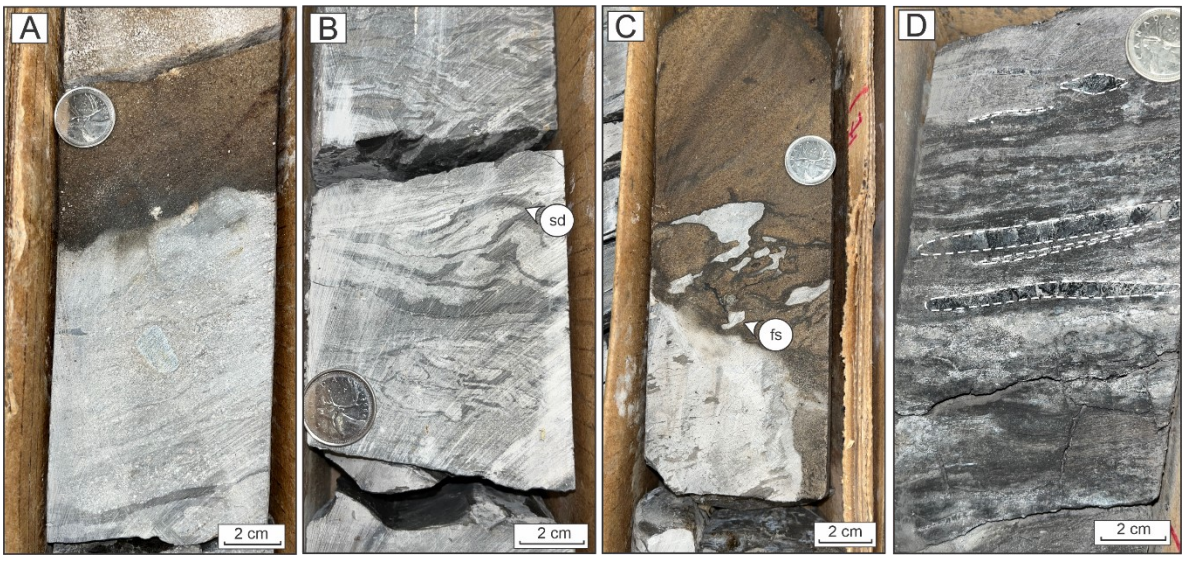

Figure 11. Core photographies of Facies Associations 2 (FA2). Erosive contact at the bottom of FA2, B) Typical synsedimentary deformation observed in planar-laminated Sandy siltstone. C) Fluid scape structures (Flame structures) at the bottom of a in-channel deposit; D) Thick carbonaceous stringers in massive siltstone. Synsedimentary deformation (sd), flame structures (fs).

Facies Association 3

Facies Association 3 corresponds with Layer 3 Upper (L3U) and Layer 2 (L2) and consists of 5-10-meter-thick fining-upward sandstone successions capped by 1-5-meter-thick sandy siltstone interbedded with planar cross-stratified sandstone (Figure 9). The basal part of each fining-upward succession is composed of trough cross-stratified, medium-grained sandstone with 15-35-cm-thick sets and a basal lag of massive coarse-grained sandstone with rip-up mud clasts (Figure 12A). Plant detritus is common along cosets and bioturbation is generally absent. Trough cross-strata usually passes up through abundant 5-15 cm thick sets of planar-cross stratified, medium- to fine-grained sandstone. Thin (1-3 mm thick) clay-rich laminae are usually located at the boundaries between sets (Figure 12B). Rare 1-2 cm thick mud beds occur between cosets (Figure 12C). The uppermost intervals of the fining upward successions consist of 1 to 5 m thick, wave-ripple laminated sandy siltstone with lesser planar and convoluted laminations, and rare massive stratification, with subordinate 20 to 150 cm- thick, very fine- to fine-grained sandstone interbeds with planar cross-stratification and common 1-2 cm-thick cosets of current ripple stratification at the top of the succession (Figure 12D). The wave-ripple laminated siltstone has erosive lower and upper contacts and varies in thickness from 1 to 5 meters. Traces of *Skolithos, Cylindricus and Conichnus* occur in a low abundance (BI: 1-2; Figure 12D). Sporadic plant roots and syneresis cracks occur in siltstone beds.

FA3 interpretation: Marginal marine tidal-fluvial channels

Facies Association 3 consists of a distinctive vertical suite of sedimentary structures characterized by a fining upward transition from rip-up clasts and coarser basal lags to 3D dunes and abundant straight-crested dunes finally being overlain by finer sandstone with current ripple lamination interbedded with wave rippled siltstone. The trough cross-stratified sandstone at the base is interpreted as in-channel deposits of 3D dunes and bars formed under sustained currents (Miall, 1978). These pass upward to tabular cross-stratification formed by straight-crested dunes with thin mud laminae within and between sets recording alternating high and low energy depositional conditions in shallower parts of the channels. The thin mud laminae interstratified with high-energy facies suggests tidal deposition in a brackish water environment, with flocculated mud deposited from suspension fallout and rapid deposition during slack-water periods (Dalrymple, 2010; Longhitano et al., 2012; La Croix and Dashtgard, 2014). The characteristic "bell-shaped" gamma-ray response of FA3 indicates a fining-upward succession associated with point bar sedimentation in a meandering channel, compared to the cylindrical gamma-ray shape of braided fluvial channel fill (Figure 16;Coleman and Prior, 1980; Rider, 1996). Wavy and planar laminated siltstone beds in the upper parts of FA3 successions evidence fluctuations from low to moderate energy wave-dominated conditions and are interpreted as floodplain and abandoned channel deposits (e.g., Davies et al., 2005). The thinner planar and ripple cross-stratified cosets of sandstone interbedded with wavy and planar mudstone are interpreted as crevasse splays (e.g., Farrell, 1987). The absence of horizontal traces, low diversity suite of *Skolithos*, *Cylindrichnus* and *Conichus* corresponds to the *Skolithos Ichnofacies,* which is typical of the trace-making fauna in high-energy tidal-fluvial estuarine channels (MacEachern, 2005).

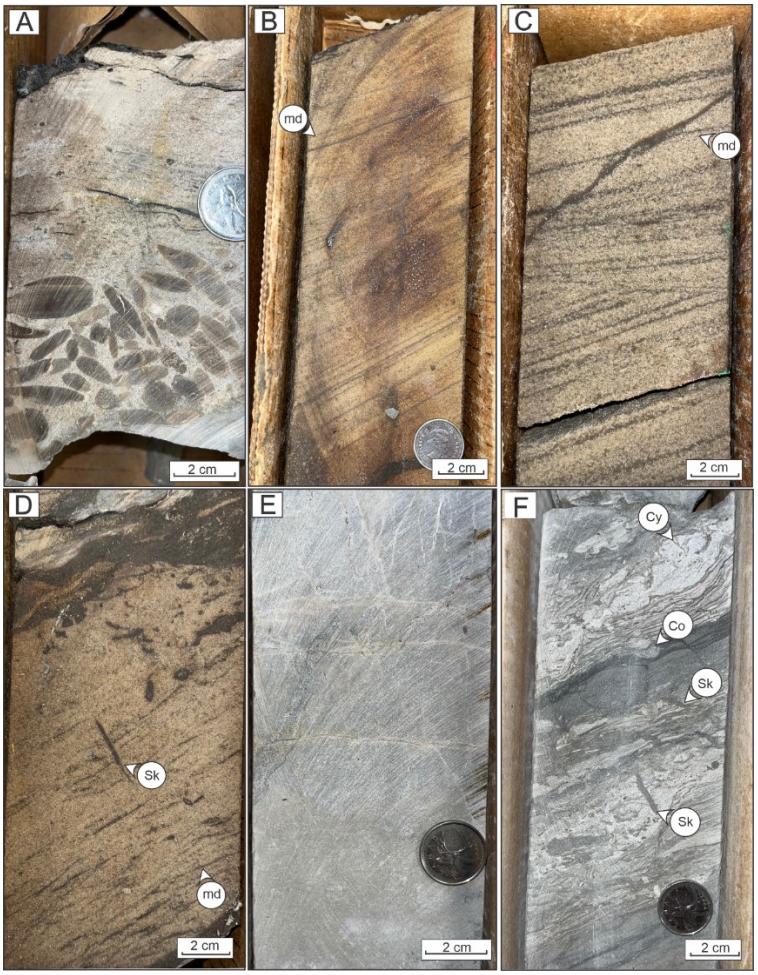

Figure 12. Core photographies of Facies Associations 3 (FA3). A) The basal part of a fining-upward succession with rip-up mud clasts; B-C) Mud drapes in planar-cross stratified sandstone and D) ripple cross stratified sandstone; E) massive siltstone; F) wave ripple laminated siltstone with traces of Skolithos (Sk), Conichnus (Co), Cylindricus (Cy).

Facies Association 4

Facies association 4 corresponds with Layer 3 Upper and Layer 2 and consists of a fining-upward heterolithic succession that grades up from very fine-grained sandstone to rootled mudstone (Figure 9). The basal interval of FA4 is dominated by 5 to 10 cm cosets of very fine-grained sandstone with current ripple cross-lamination and flaser bedding (Figure 13A). The low-intensity bioturbation is characterized by *Skolithos* traces (BI: 1-2). This basal interval is succeeded upward by 1-10 cm thick massive siltstone beds that are interbedded with thin 1-5 cm thick cosets of wave ripple cross-laminated very fine-grained sandstone with rare lenticular stratification, convoluted

lamination and syneresis cracks. *Thalasionaides, Planolites, Diplocaterion* and *Rosselia rotatus traces* are common in this heterolithic succession (BI: 2-3; Figure 13B-F). The massive siltstone gradually overlies the heterolithic strata, showing moderate to high bioturbation intensity (BI 3-4), including *Teichichnus*, *Diplocaterion, Asterosoma, Conichnus, Rosselia Socialis, Rosselia Rotatus, Planolites and Skolithos* traces (Figure 13G-J). The top of FA4 is dominated by 10 to 40 cm-thick massive black non-bioturbated mudstone beds interbedded with 15-30 cm thick structureless muddy siltstone with abundant *Skolithos* traces (BI: 2-3) plant roots, amorphous patches of siderite and erosional upper boundaries (Figure 13K-L).

FA4 interpretation: tidal flats

These bioturbated heterolithic strata are interpreted as tidal flat deposits showing the typical upward transition from sand flats through mixed flats and finally to mud flats (e.g., McIlroy et al., 2005; Dalrymple, 2010; Dalrymple et al., 2012). The current-rippled sandstone at the base of FA4 is interpreted as deposits of sand flats formed in the lower flow regime, in a lower to moderate energy mesotidal setting (Dalrymple et al., 1990; Dalrymple and Choi, 2007). The ichnofaunas are dominated by vertical burrows evidencing the *Skolithos* Ichnofacies. The overlying interbedded siltstone with locally lenticular stratified wave-rippled very fine-grained sandstone is interpreted to record sedimentation in mixed flats, with layers laid down by alternating tidal currents and slack-water conditions, respectively (Heterolithic tidal bedding, Desjardins et al., 2012; Flemming, 2012). The ichnogenera associated with these mixed tidal flats corresponds to Cruziana-Skolithos Ichnofacies based on the presence of vertical burrows (e.g., *Diplocaterion*, *Rosselia rotatus*) and horizontal burrows (e.g., *Planolites*, *Thalassinoides*). The mixed flats are succeeded upward by mud flats deposits, preserved as bioturbated siltstone, massive mudstone interbedded with

structureless muddy siltstone (Figure 13). Plant roots in these mud flat strata suggest the local presence of terrestrial vegetation, indicating low-energy deposition in a supratidal setting (Dalrymple, 2005; Desjardins et al., 2012). In general, trace fossil assemblages in FA4 correspond to mixed *Cruziana-Skolithos* ichnofacies which are common in heterolithic substrates under the influence of shallow water based on the mixed association of vertical and inclined structures (MacEachem et al. 2005).

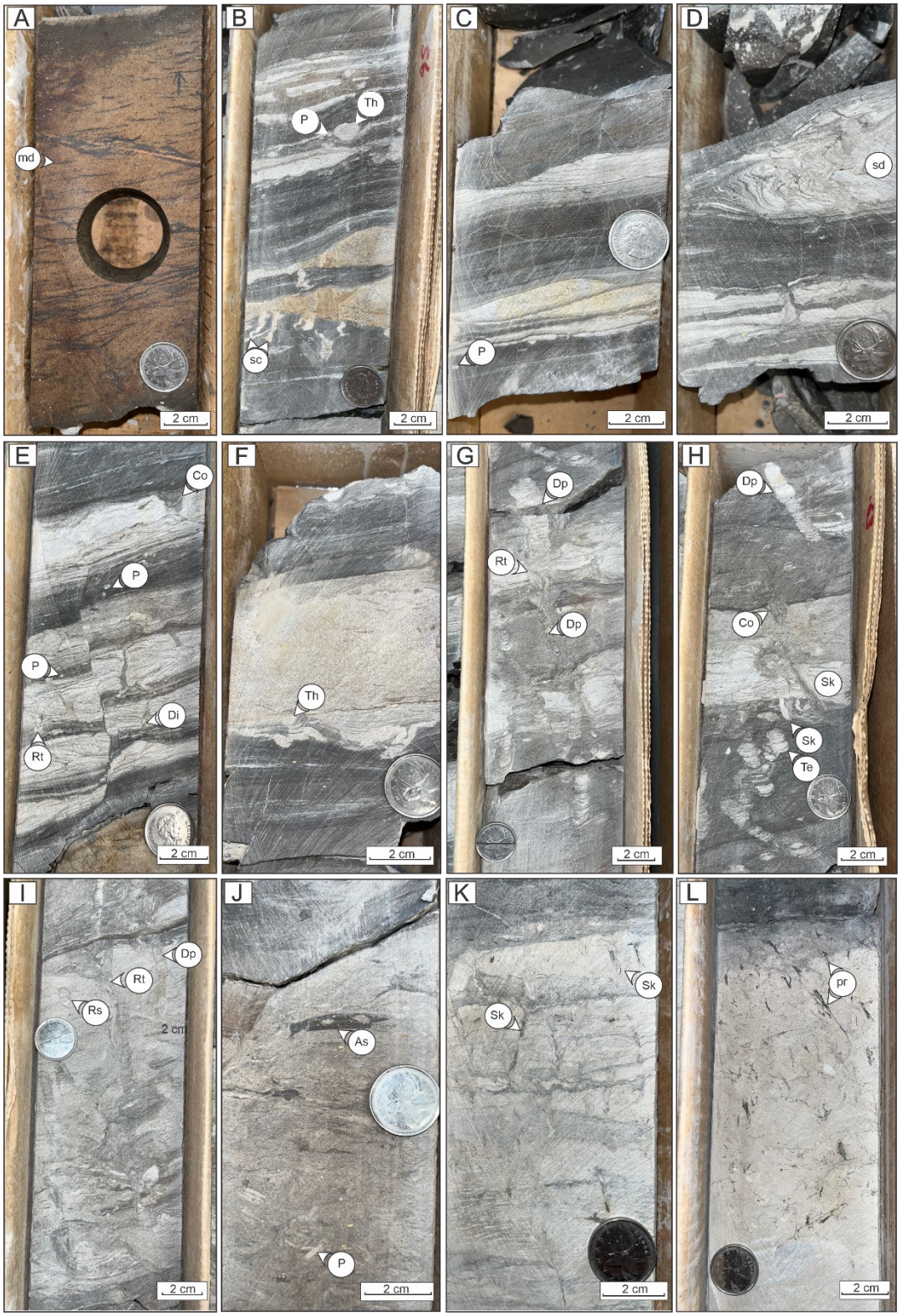

Figure 13. Core photographs of Facies associations 4 (FA4): A) sand flats; B-J) mixed flats; K-L) mud flats. Teichichnus (Te), Diplocaterion (Dp), Asterosoma (As), Conichnus (Co), Rosselia Socialis (Rs), Rosselia Rotatus (Rt), Planolites (P), Thalassionides (Th), Skolithos (Sk), syneresis cracks (sc), synsedimentary deformation (sd).

Facies Association 5

Facies association 5 consists of a 5 to 10 m-thick section of bioturbated grey silty mudstone with shell fragments and siderite patches (Figure 9). Bioturbation is typically of low diversity and high to medium intensity (BI 4-5). The bulk suit of traces consists of deposit feeders such as abundant *Chondrites*, *Planolites* and a few *Asterosoma* and *Thalassinoides* traces. Subordinate vertical traces such as *Ophiomorpha* are uncommon (Figure 14). Silty mudstone widely contains shell debris such as bivalves, gastropods and rare scleractinian corals. These corals are located toward the top of the massive bioturbated mudstone and were observed in southwest and central zones of the Hibernia field.

FA5 interpretation: marine offshore

Facies Association 5 corresponds to the Medial Shale, which was interpreted to record marine inundation in the Hibernia field by Sinclair et al. (2005). The absence of cross-bedded sandstones, and a high bioturbation index (BI 4-5) indicates low sedimentation rates. Additionally, the fine-grained sediments, shell debris, low diversity and uniform distribution of *Cruziana* suites, especially *Chondrites*, are the main indicators that FA5 strata were deposited in an upper offshore environment (Pemberton et al., 2012). The occurrence of *Chondrites* is also associated with transgressive deposits in association with maximum flooding intervals (Knaust, 2017). Furthermore, the Chondrites-producer tolerates low oxygen concentration in stagnant conditions (e.g., estuaries, lagoons, embayments; Savdram and Bottjer, 1991; Martin, 2004). The presence of siderite also indicates post-depositional microbial activity, which is frequent in coastal sediments (Morad 1998; Lin et al., 2020). The abundant shell debris and intervals with scleractinian corals mark the point of maximum of marine inundation.

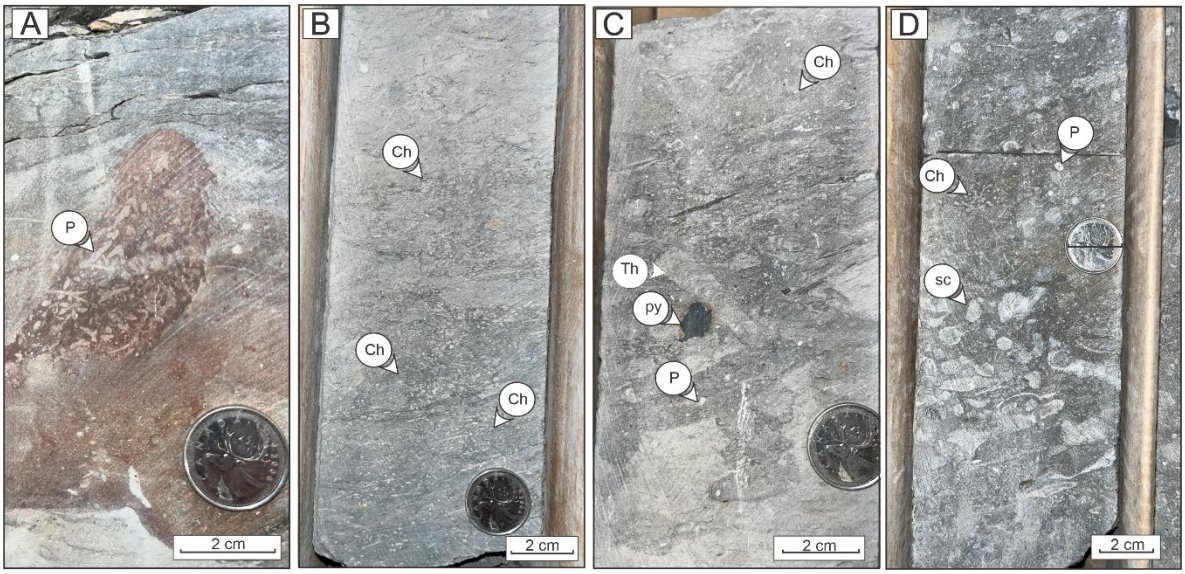

Figure 14. Core photographs of Facies Associations 5 (FA5) illustrating the main trace fossils. Planolites (P), Chondrites (Ch), Thalassinoides (Th). Scleraptinian coral (sc), pyrite (py).

Facies Association 6

Facies Association 6 corresponds with Layer 1 and consists of 3 to 6 m thick coarsening-upward successions beginning with a 1-3 m thick bed of shelly muddy siltstone overlain by 20-40 cm-thick beds of wave ripple and planar cross-laminated very fine-grained sandstone interbedded with 5-10 cm thick beds of structureless siltstone with sandy lenses (Figure 9). Shell-rich layers, 1-3 cm thick, occur mainly in muddy siltstone at the bottom of the successions. Amorphous patches and layers of siderite and carbonaceous stringers are common overall (Figure 15). Bioturbation intensity is low to moderate (BI: 2-3) with sparse traces of *Asterosoma*, *Planolites*, *Bornichnus*, *Diplocaterion*, and *Siphonichnus*. These strata are gradationally overlain by 1-5-cm cosets of planar cross-stratified very fine- to fine-grained sandstone (5 mm thick sets) with 1-2 mm thick mud drapes within sets and a few traces of *Skolithos*, *Rosselia socialis*, and *Ophiomorpha* (BI: 1-2). These cross-bedded sandstones are capped by 1-3 m-thick stacked medium- to coarse planar cross-

stratified sandstone forming 20-30 cm cosets and 5-10-cm thick sets with occasional wavy mud drapes and common *Ophiomorpha* traces (BI: 1-2). Finally, the stacked planar cross strata are sharply overlaid by 20-50 cm thick shell-rich muddy siltstone interbedded with wave ripple, and planar cross laminated siltstone interbeds rare 5-10 cm thick massive coal beds.

FA6 interpretation: Tidal bars

The upward coarsening succession of shell-rich muddy siltstone, wave ripple laminated siltstone, planar cross strata with mud drapes and sporadic coal beds indicates sedimentation in a marginal marine marsh or shallow vegetated lagoon under the influence of tides. The shell-rich muddy siltstone reflects low sedimentation rates with weak tidal currents (e.g. Olariu et al., 2012). The planar cross-stratified sandstone with mud drapes is a distinctive feature of high-energy tidal environments (Dalrymple and Rhodes, 1995; Longhitano et al., 2012, 2014; La Croix and Dashtgard, 2014). The cross-bedded sandstone records the migration of straight-crested dunes under repeated flood and ebb tide cycles corresponding to 3-6-meter-thick tidal bars (e.g., Nio and Yang, 1991; Olariu et al., 2012). The wave ripple laminated siltstone indicates periods of low flow velocity in the through of the tidal bars during tidal current reversals, corresponding to bottom sets (Olariu et al., 2012). The trace fossil assembles vary from mixed *Cruziana-Skolithos* ichnofacies (bottom sets) to *Skolithos* Ichnofacies (straight-crested dunes), suggesting moderate to high energy shallow-marine conditions (MacEachern et al., 2010). Moreover, the high diversity of ichnogenera in the basal interval is an indicator of a low-stress environment with normal levels of salinity and low concentrations of sediment in suspension (MacEachern et al., 2010; Pemberton et al., 1992; Olariu, et al., 2012). The upward progression of the characteristic funnel-shaped gamma ray response also reflects the prograding nature of FA6 (Figure 16). In this context, facies association

6 reflects clastic progradation and progressively shallow and high-energy sedimentation in a tide-dominated marine shoreface influenced by the formation of tidal bars (Dalrymple et al., 1992).

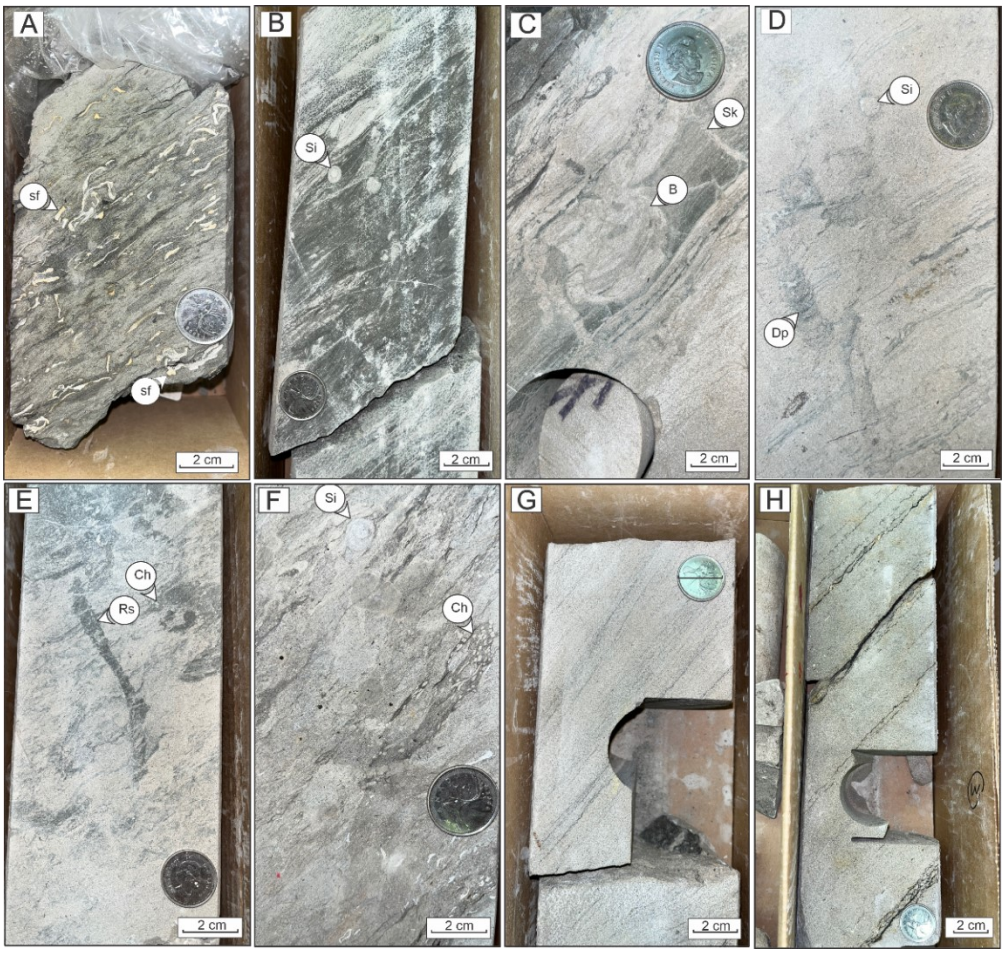

Figure 15. Core photographs of Facies Associations 6 (FA6). A-F) bottom sets showing the characteristic ichnogenera of FA6 and G-H) Planar cross-stratified very fine- to fine-grained sandstone. Asterosoma (As), Planolites (P), Bornichnus (B), Diplocaterion (Dp), and Siphonichnus (Si), Chondrites (Ch), Rosselia Socialis (Rs, shell fragments (sf).

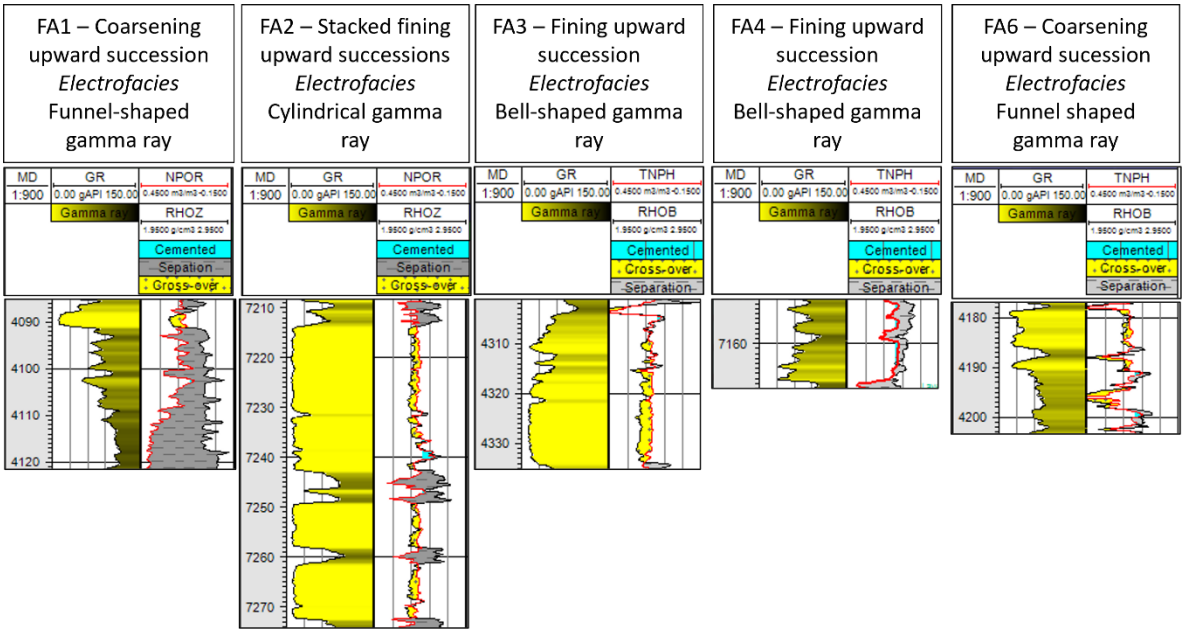

Figure 16. Well log response of facies associations.

2.4.2 Macromorphology and distribution of carbonate cements

Calcite and dolomite cements typically form layers with planar and irregular boundaries exhibiting strata-bound characteristics including orientations parallel to bedding and boundaries that conform to bedding planes (Figure 17). The thickness of the calcite- and dolomite-cemented layers stands around 50 cm to 2 m. Calcite-cemented layers were identified in sandstone of marginal marine tidal-fluvial channel facies (FA3) of Layer 3 Upper (L3U), sandstone and siltstone of open marine embayment shelf (FA5) and subtidal sand bars facies associations (FA6) of the Medial Shale and Layer 1, respectively. Dolomite-cemented sandstone is exclusive to the delta front (FA1) and offshore marine facies associations (FA5) of Layer 4 and the Medial Shale. Ferroan calcite layers are not aligned with bedding and usually crosscut sedimentary structures, and their thickness does not exceed three meters approximately (Figure 17). Ferroan calcite-cemented layers are dispersed throughout the stratigraphy of the Lower Hibernia zone. (i.e., FA2, FA3, FA5, FA6). Siderite

nodules are common in siltstones of FA5 and FA6 and ferroan calcite- and calcite-cemented nodules are not evident in the Lower Hibernia zone.

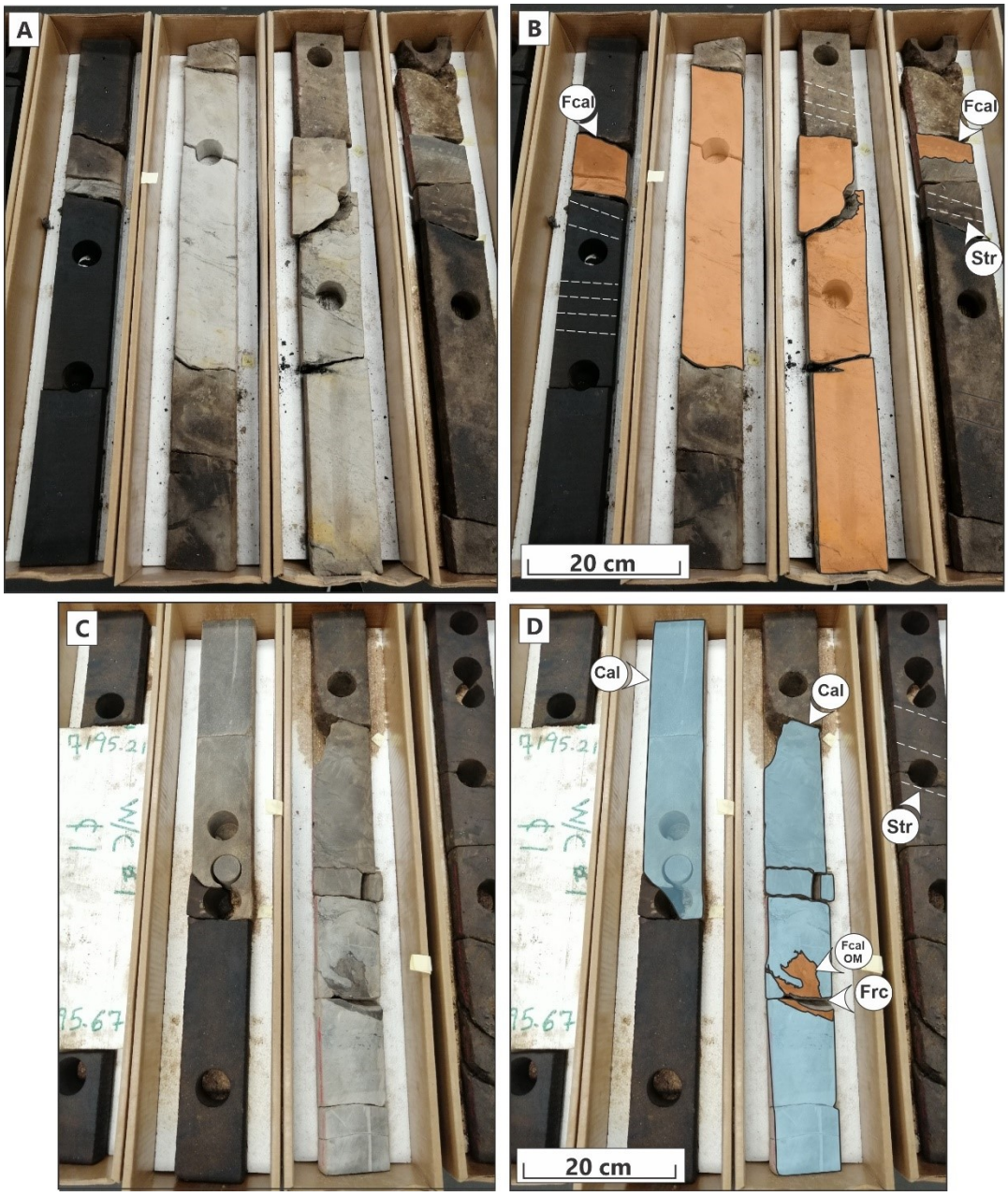

Figure 17. Morphology of cemented intervals, (A-B) calcite and (C-D) ferroan calcite-cemented sandstone. (Fcal) Ferroan calcite; (Cal) calcite; (Frc) fracture; (Stra.) Stratification, (OM) organic matter. Hibernia B 16-55 well, ~7200 m MD.

2.4.3 Sandstone Petrography

Core and petrographic observations show that the Hibernia sandstone beds plot within the field of quartzose sandstone on the QFL diagram (Garzanti; 2018; Table 2; Figure 19). Sand grains are moderately to well-sorted, fine to coarse-grained, and subangular to subrounded, showing mainly tangential and rarely flattened contacts. Quartz grains (80-98%) commonly show corroded boundaries (Figure 18) and are mainly monocrystalline, and a few others are polycrystalline, exhibiting sweeping extinction. Feldspars, mainly plagioclase, are relatively minor (< 9%), and exhibit corrosion, partial dissolution and minor replacement by calcite, sericite, and clays. Accordingly, the current proportions of detrital feldspar are much lower than the initial proportions following sedimentation, suggesting that these sandstone strata were most likely quatzo-feldspathic upon deposition. Rock fragments are mainly metamorphic and igneous in origin (< 10%). Authigenic minerals include pyrite, calcite, ferroan calcite, dolomite, ferroan dolomite, siderite, and quartz overgrowths. Quartz overgrowths are less common in carbonate-cemented sandstones. Accessory minerals include glauconite, chlorite, apatite, rutile, epidote and zircon. Shell fragments include gastropods, brachiopods, bivalves, sponges and unidentified bioclasts, which occurs mainly in sandstone and siltstone of FA1, FA5, and FA6. Additionally, bioclasts show evidence of dissolution and local replacement by authigenic carbonate. Carbonaceous stringers are common in sandstone samples of FA2 and FA3. Oversized pores, larger than adjacent grains and occasionally containing remnant calcite cement are common in sandstones (Figure 18).

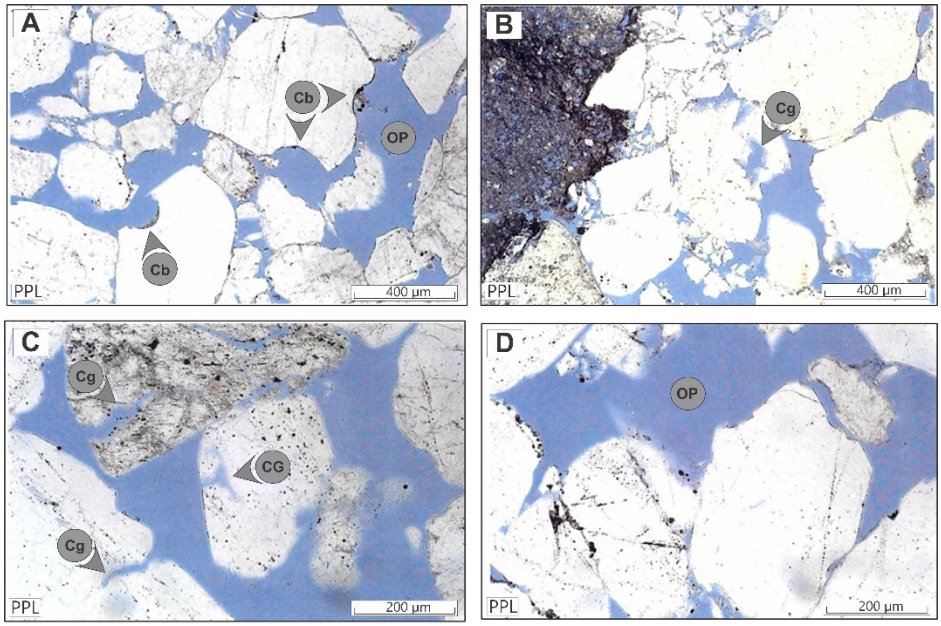

Figure 18. Microphotography of Hibernia sandstone exhibiting well-preserved intergranular porosity, oversized pores and corroded grains. A) Hibernia B-16 2, 4399.62 m; B) Hibernia B-16 2, 4398,39 m; C) Hibernia B-16 2, 4402.3 m; D Hibernia B-16 2, 4376.64 m. (Cb) Corroded grain boundaries; (Cg) Corroded grain, (OP) Oversized pores. Modified after Core Lab (1998).

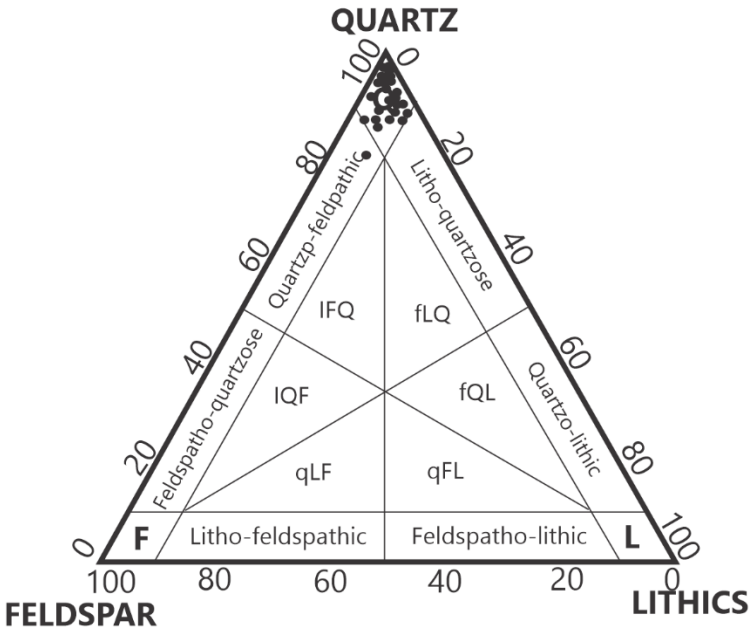

Figure 19. QFR diagram of sandstone petrography showing the composition of the Hibernia sandstone. lFQ = litho-feldspatho-quartzose; lQF = litho-quartzo-feldspathic; qLF = quartzo-litho-feldspathic; qFL = quartzo-feldspatho-lithic; fQL = feldspatho-quartzo- lithic; fLQ = feldspatho-litho-quartzose. After Garzanti (2019)

Table 2. Mineralogic composition (%) of the Lower Hibernia zone samples determined by optical microscopy. Q + F + L = 100%. Layer 1 (L1), Layer 2 (L2), Medial Shale (MS), Layer 3 (L3), Layer 4 (L4).

Sample	Well	FA(RU)	Unit	GS (µm)	Grain size	Grain shape	Qtz	Feld.	Lit.	Car. Cem.	Pyr.	Qo
S1	B-16 2	FA6 (L1)	L1	15	medium silt	angular to subangular	97	1	2	13	2	0
S2	B-16 2	FA6 (L1)	L1	126	v. fine sand	angular to subangular	92	2	6	19	3	1
S3	B-16 28	FA6 (L1)	L1	68	v. fine sand	subangular to subrounded	96	1	3	23	2	1
S4	B-16 28	FA6 (L1)	L1	76	v. fine sand	angular to subangular	95	1	4	15	2	1
S5	B-16 28	FA6 (L1)	L1	528	coarse sand	angular to subangular	86	8	5	32**	5	4
S6	B-16 28	FA5 (MS)	MS	437	medium sand	subnagular to subrounded	87	6	7	27	4	0
S7	B-16 12	FA6 (L1)	L1	72	v. fine sand	subangular to subrounded	94	3	3	18	5	3
S8	B-16 12	FA6 (L1)	L1	89	v. fine sand	angular	94	3	3	28	2	1
S9	B-16 54W	FA5 (MS)	MS	19	v. fine silt	angular	93	1	6	30*	1	0
S10	B-16 54W	FA5 (MS)	MS	15	v.fine silt	subangular	96	2	2	38	1	9
S11	B-16 54W	FA5 (MS)	MS	55	medium silt	angular	94	3	3	29*	2	0
S12	B-16 55	FA1 (L4)	L4	458	medium sand	subangular	97	3	0	35*	3	1
S13	B-16 55	FA2(L3)	L3	1301	coarse sand	subangular to subrounded	89	7	4	24	3	0
S14	B-16 55	FA2(L3)	L3	880	coarse sand	subangular to subrounded	97	1	1	19	1	2
S15	B-16 55	FA3(L3)	L3	590	coarse sand	subangular to subrounded	98	2	0	33	1	1
S16	B-16 55	FA3(L3)	L3	489	medium sand	subrounded	94	5	2	29	5	2
S17	C-96	FA2(L3)	L3	209	fine sand	subangular	95	4	1	17	6	3
S18	B-16 28	FA5 (MS)	MS	69	coarse silt	subnagular	97	2	1	11	1	0
S19	B-16 55	FA1 (L4)	L4	473	medium sand	subrounded	93	4	3	18*	4	2
S20	B-16 55	FA2(L3)	L3	835	coarse sand	subrounded	93	4	3	25	3	2
S21	B-16 55	FA1 (L3)	L3	444	medium sand	subangualr to subrounded	98	2	0	0	3	0
S22	B-16 55	FA2(L3)	L3	790	corase sand	subrounded	94	6	0	26	2	0
S23	B-16 55	FA2(L3)	L3	781	medium sand	subangular-subrounded	93	5	2	22	3	0
S24	B-16 55	FA2(L3)	L3	487	medium sand	subangular	92	7	1	23	2	1
S25	B-16 55	FA2(L3)	L3	432	medium sand	subangular	88	7	4	25	4	2
S26	B-16 55	FA3(L3)	L3	289	medium sand	subaangular-subrounded	86	9	6	27	2	1
S27	B-16 55	FA3(L3)	L3	613	coarse sand	igual a S15	96	4	0	30	1	1
S28	B-16 54W	FA5 (MS)	MS	20	v.fine silt	subangular	93	3	4	28*	2	0
S29	B-16 54W	FA5 (MS)	MS	18	v. fine silt	subangular	97	1	1	30*	1	0
S30	B-16 55	FA2(L3)	L3	183	fine sand	subangular	92	7	1	25	4	0
S31	B-16 28	FA4 (L2)	L2	112	very fine sand	subangular	91	4	5	20	3	0
S32	B-16 28	FA4(L2)	L2	115	very fine sand	subangular	90	3	7	23	5	0
S33	B-16 28	FA5 (MS)	MS	53	medium silt	subangular to subrounded	96	4	0	25	1	0
S34	B-16 28	FA5 (MS)	MS	72	coarse silt	subangular to subrounded	87	4	9	10	5	0
S35	B-16 28	FA5 (MS)	MS	67	coarse silt	subangular to subrounded	90	2	8	13	6	0
S36	B-16 28	FA5 (MS)	MS	61	coarse silt	angular	90	3	7	12	5	0
S37	B-27	FA2(L3)	L3	219	fine sand	subangular	93	3	4	22	2	2
S38	B-27	FA2(L3)	L3	204	fine sand	angular to subangular	97	1	1	24	1	0
S39	B-27	FA4(L3)	L3	233	fine sand	subangular to subrounded	89	4	7	25	3	2
S40	B-27	FA5(MS)	MS	98	very fine sand	subangular	91	2	6	13	5	0
S41	B-27	FA5 (MS)	MS	68	coarse silt	angular	88	2	10	10	7	0
S42	B-27	FA5 (MS)	MS	71	coarse silt	angular	92	0	8	22*	2	0
S43	B-27	FA5 (MS)	MS	79	coarse silt	subangular	94	2	4	20*	3	0
S44	B-27	FA5 (MS)	MS	50	medium silt	subangular	94	2	4	24*	4	0
S45	B-27	FA5 (MS)	MS	91	v.fine silt	angular	99	1	0	25*	3	0
S46	B-27	FA3(L3)	L3	201	fine sand	angular	99	1	0	29**	1	0
S47	B-16 17	FA5 (MS)	MS	94	v. fine silt	angular	97	3	0	23*	2	0
S48	B-16 17	FA5 (MS)	MS	81	coarse silt	angular to subangular	95	0	5	40	2	0
S49	B-16 17	FA5 (MS)	MS	26	medium silt	angular to subangular	91	6	3	27*	4	0
S50	B-16 17	FA5 (MS)	MS	20	medium silt	angular to subangular	96	1	3	21	1	0
S51	B-16 17	FA5 (MS)	MS	18	medium silt	angular to subangular	96	3	1	29*	3	0

* Dolomite cement; **Dolomite + Siderite; FA: Facies Association; RU: Reservoir Unit; GS: Grain size; Qtz: Quartz; Feld: Feldespar; Lit: Lithic fragments; Car. Cem: Carbonate cements; Pyr: Pyrite; Qo; Quartz overgrowth

2.4.4 Carbonate cement petrography

Petrographic examination of the Lower Hibernia zone reveals six distinct phases of carbonate cements: calcite, ferroan calcite, grain-rimming micrite, dolomite, ferroan dolomite and siderite. Ferroan calcite represents the most prevalent pore-filling cement of sandstones with micrite, calcite, dolomite and siderite being comparatively less common. Additionally, no primary two-phase fluids inclusions were observed in any of the investigated carbonate cements.

Calcite

Calcite occurs as a pervasive cement in FA3, FA5 and FA6 in the form of poikilotopic crystals (600–800 μm) and microcrystalline aggregates engulfing and partially replacing detrital grains (Figure 20A-C). Calcite cement usually shows intergrowth textures with corroded quartz grains. Grain-floating textures in which calcite cement fills relatively high apparent intergranular pore space volumes (33% IGV) with rare grain-grain contacts (Figure 24B; Table 2). Calcite is less abundant than its ferroan calcite counterpart in the Lower Hibernia zone, described below.

Ferroan Calcite

Ferroan calcite predominates as the primary pore-occluding carbonate cement in the Lower Hibernia zone, filling intergranular and intragranular porosity and constituting up to 20 % of the rock volume (Figure 20E-F). Ferroan calcite occurs at different intervals and facies associations of the Lower Hibernia zone (e.g., FA2, FA3, FA5, FA6), and there does not appear to be any facies or stratigraphic control on its distribution. Typically, ferroan calcite occurs as pore-filling poikilotopic crystals (700-1200 μm) wrapping detrital grains, which are moderately fractured (Figure 20F-G).

Ferroan calcite-cemented samples exhibit tangential contacts among grains with a closer packing compared with calcite-cemented sandstones (22-28% IGV). Furthermore, 10-15 μm wide ferroan calcite veins locally crosscut detrital quartz grains and dolomite cements (Figure 23B). A bizarre fabric of ferroan calcite forming as fluid-like patches in core along a 2 cm thick fracture occurs at 7194 m of depth Hibernia B-16 55 (Figure 22A-B). This fabric exhibits subhedral to euhedral crystals of ferroan calcite engulfing opaque organic material that shows dark brownish colour in plane-polarized light (Figure 23C-D).

Grain-rimming micrite

Grain-rimming micrite is a non-pervasive cement that occurs mainly in sandstones of delta front facies associations (FA1). It occurs as microcrystalline aggregates forming thin crusts around carbonate shell fragments and detrital grains, along with clays and predating dolomite cementation (Figure 21 A-B).

Dolomite

Pervasive dolomite cement occurs as tightly packed blocky brownish crystals of uniform size (60–70 μm) in sandstone of FA1 (delta front facies, Layer 4) and siltstone of FA5 (marine shelf facies, Medial Shale) filling intergranular space and comprising up to 23% of the samples (Figure 21A-C; Figure 24 A). Dolomite is less abundant than calcite and ferroan calcite cements. Euhedral to subhedral dolomite crystals also occur rarely in siltstones of tidal flat facies (FA4) in Layer 2. Dolomite-cemented sandstones exhibit under-compacted grain fabrics (35% IGV), with grain

contacts observed in thin sections. Generally, dolomite cements form crystalline mosaics and some cavities in bioclasts are also filled with ferroan dolomite.

Ferroan Dolomite

Ferroan Dolomite is a minor and non-pervasive cement that exhibits two main fabrics: (1) microcrystalline aggregates (< 20 μm) of brown ferroan dolomite filling intergranular space constituting up to 13% of the observed sample in FA1 delta front facies of Layer 4 (Figure 21C); and (2) rare subhedral colourless ferroan dolomite crystals (100–200 μm) known as saddle dolomite exhibit the typical sweeping extinction (Figure 21F). The saddle ferroan dolomite occurs as coarse dolomite crystals in moldic or vuggy pores, mainly in shelf marine siltstone facies of FA5.

Siderite

Siderite is widespread in the Lower Hibernia zone, filling intergranular spaces in sandstone and siltstone of FA2, FA3, FA5 and FA6. However, it rarely forms as a pervasive cement. Microcrystalline siderite crystals are brown and occur as rhombohedrons (10–20 μm; Figure 23A) in marine siltstones of FA5 (Medial Shale). It also occurs in the nuclei of pyrite forming rims around detrital grains in and predating ferroan calcite cementation in sandstone of FA2 (Figure 23F). Additionally, medium-grained spherulitic crystals (250–800 μm) occlude intergranular space in sandstone of FA3 and FA4, constituting up to 15 % of the rock volume (Figure 22C-D). These spherical iron carbonate concretions consist of a microcrystalline core with more coarsely

crystalline cortices exhibiting a maltese cross-extinction pattern, typical feature of sphaerosiderites (e.g., Ludvigson et al., 1998).

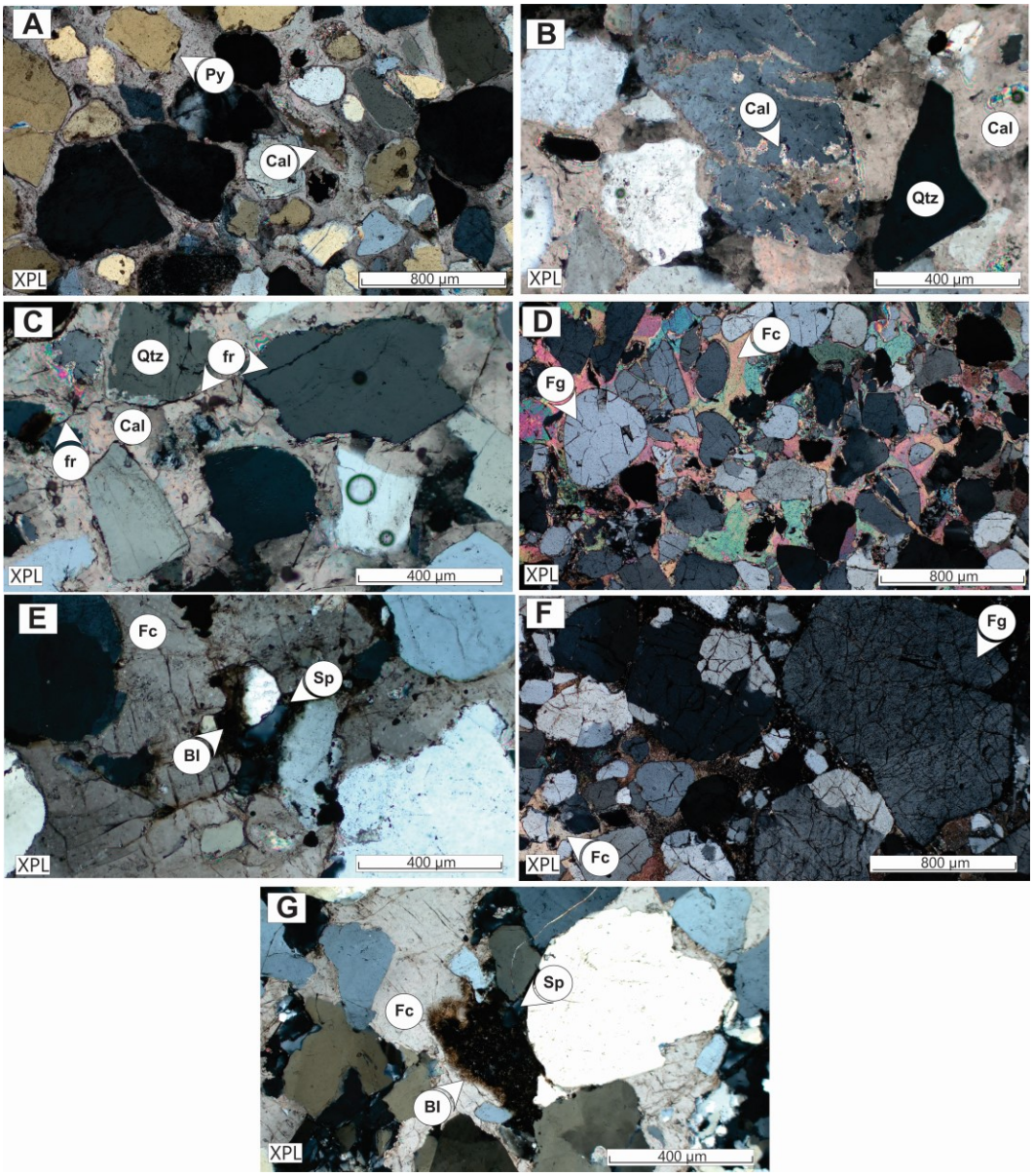

Figure 20 Photomicrographs of petrographic features of sandstones and siltstones of the lower Hibernia zone showing detrital grains with effective porosity occluded by A-C) Calcite (Cal); D-G) ferroan calcite(Fc). Note in (F) the extensive occurrence of fractures within detrital grains (Fg) and, ferroan calcite remains unfractured. Sample S15 (A), S26 (B), S27 (C), S14 (D), S22 (E), S23 (F), S25 (G). Bitumen (BI), Calcite (Cal), Ferroan Calcite (Fc); Fractured grain (Fg); Fracture (fr); Pore space (Sp); Pyrite (Py); Quartz (Qtz).

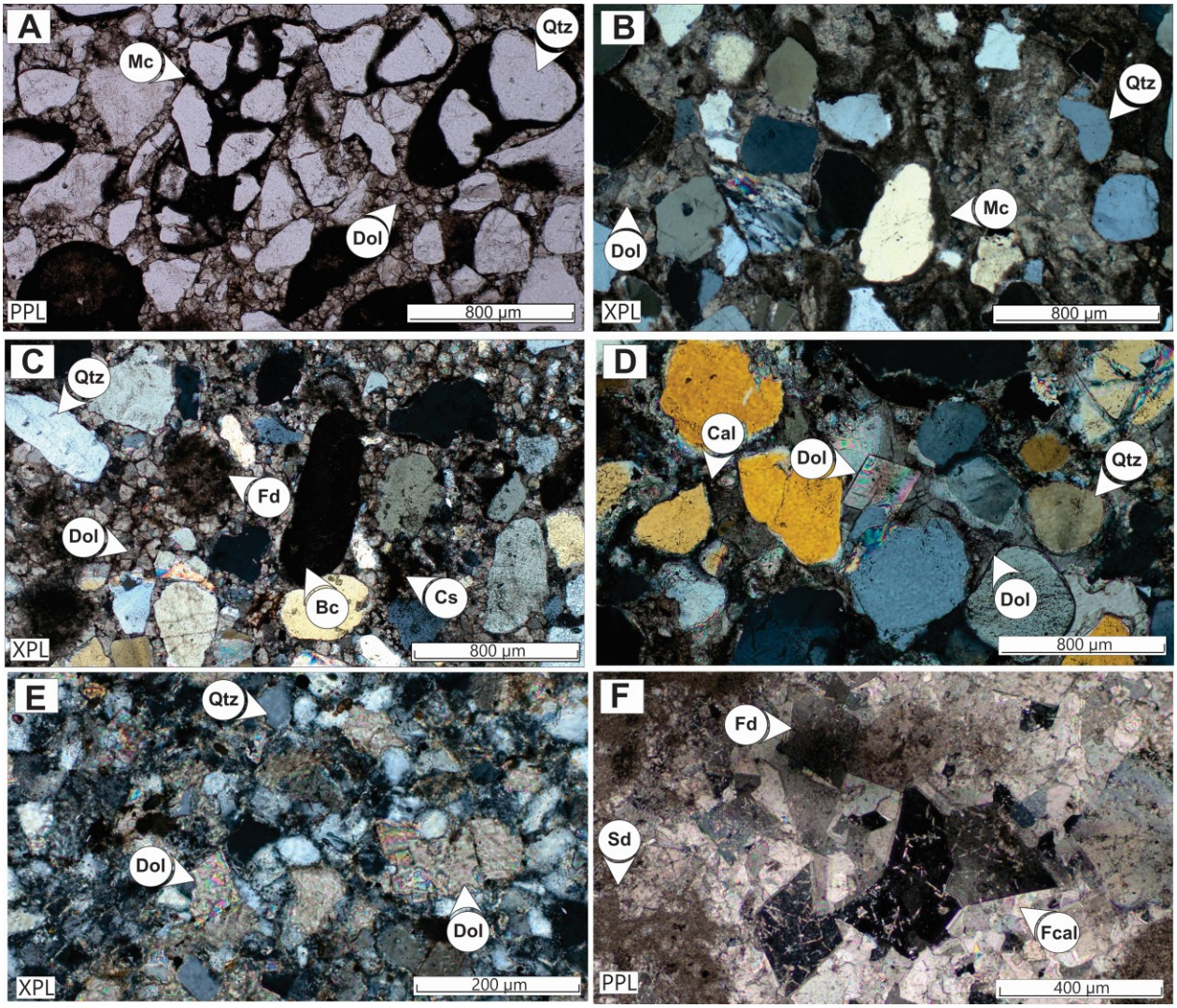

Figure 21. Photomicrographs of petrographic features of sandstones and siltstones of the lower Hibernia zone showing detrital grains with effective porosity occluded by A) grain-rimming cements (Mc); B-C) blocky dolomite (Dol) and microcrystalline ferroan dolomite (Fd); D-E) subhedral dolomite postdating calcite cementation; F) Saddle ferroan dolomite (Fd). Sample S12 (A), S19 (B), S12 (C), S6 (D), S43 (E), S10 (F). Quartz (Qtz), Bioclasts (Bc).

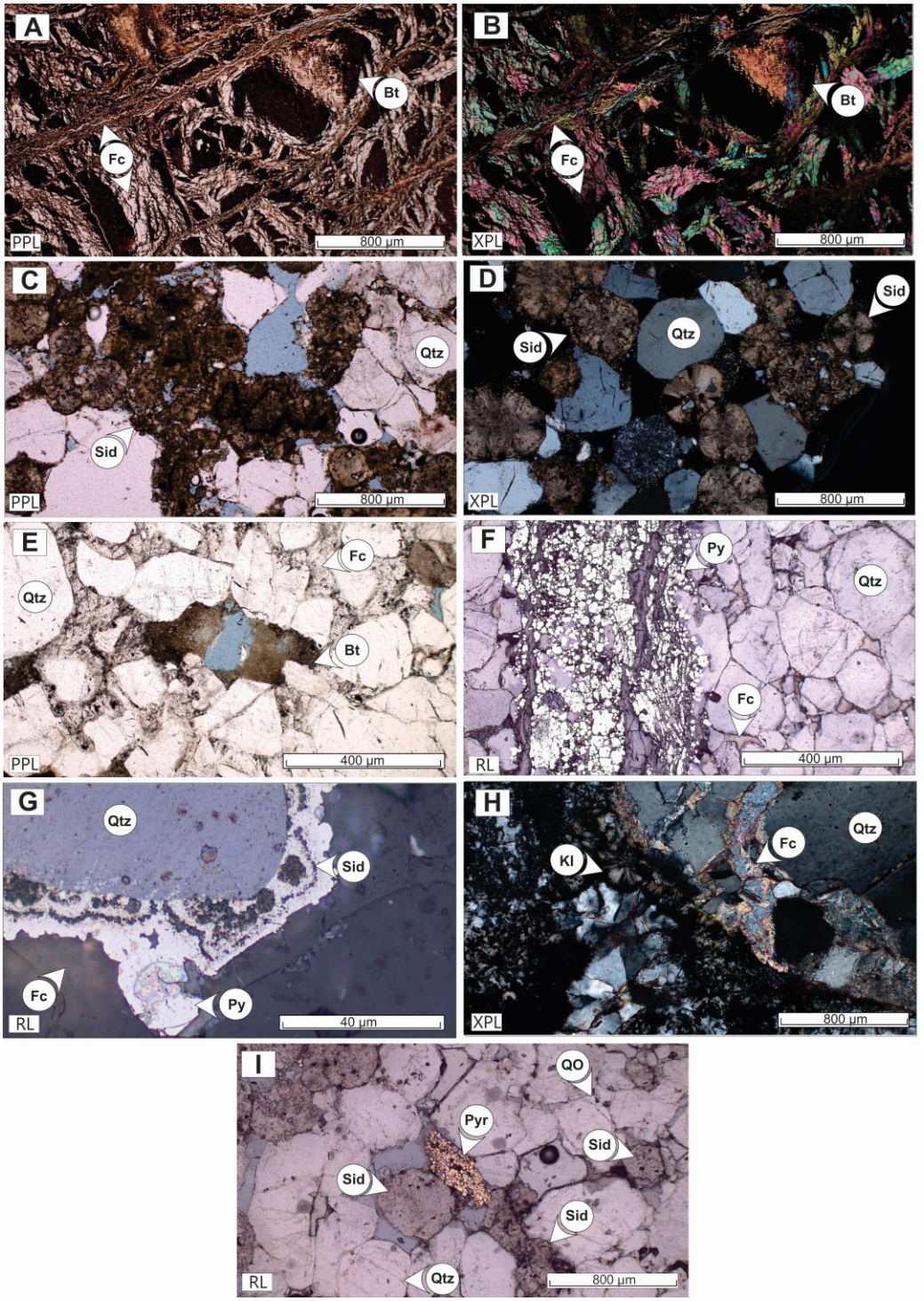

Figure 22. Photomicrographs of petrographic features of sandstones and siltstones of the Lower Hibernia zone. A-B) subhedral to euhedral crystals of ferroan calcite (Fc) engulfing opaque organic masses (Bt); C-D) Sphaerosiderite (Sid) occluding primary intergranular porosity; E) Ferroan calcite and solid bitumen filling intergranular porosity; F) Pyrite (Py) occluding intergranular spaces in fine-grained layers with abundant carbonaceous stringers; G) Grain-coating of siderite and pyrite predating ferroan calcite cementation; H) Vermicular kaolinite (Kl) and ferroan calcite; I) pyrite and sphaerosiderite occluding primary porosity. Sample S16 (A-B), S5 (C-D), S25(E), S17 (F-G), S14 (H), S5 (I).

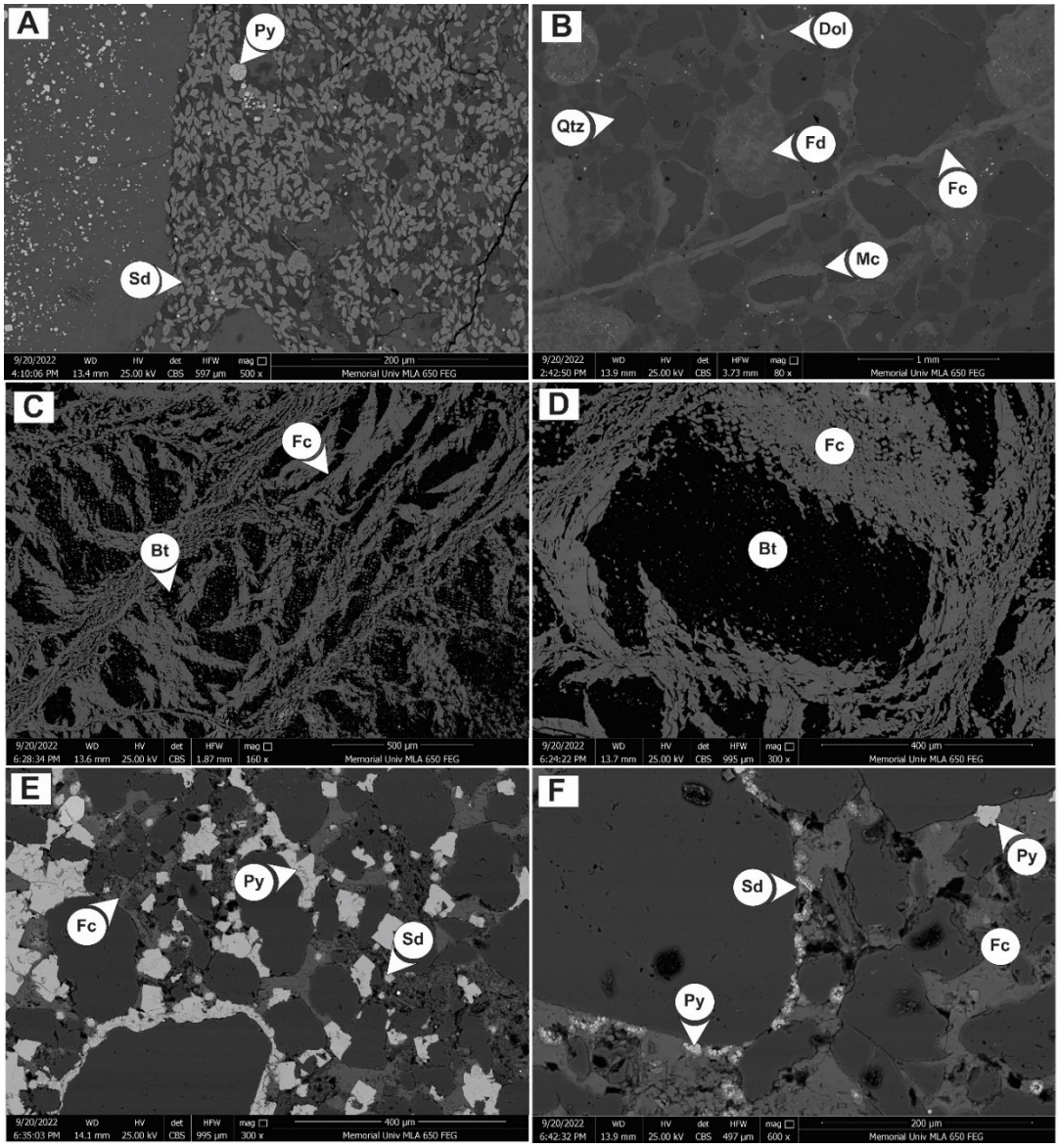

Figure 23. BSEM images of polished thin sections showing A) microcrystalline siderite (Sd) along with botryoidal pyrite (Py); B) grain-rimming micrite (Mic), dolomite (Dol) and ferroan dolomite (Fd) filling intergranular porosity; C-D) Ferroan calcite encapsulating solid bitumen; E-F) Siderite and pyrite forming grain-coating cements and predating ferroan calcite cementation. Sample S10 (A), S12 (B), S16 (C-D), S17 (E-F).

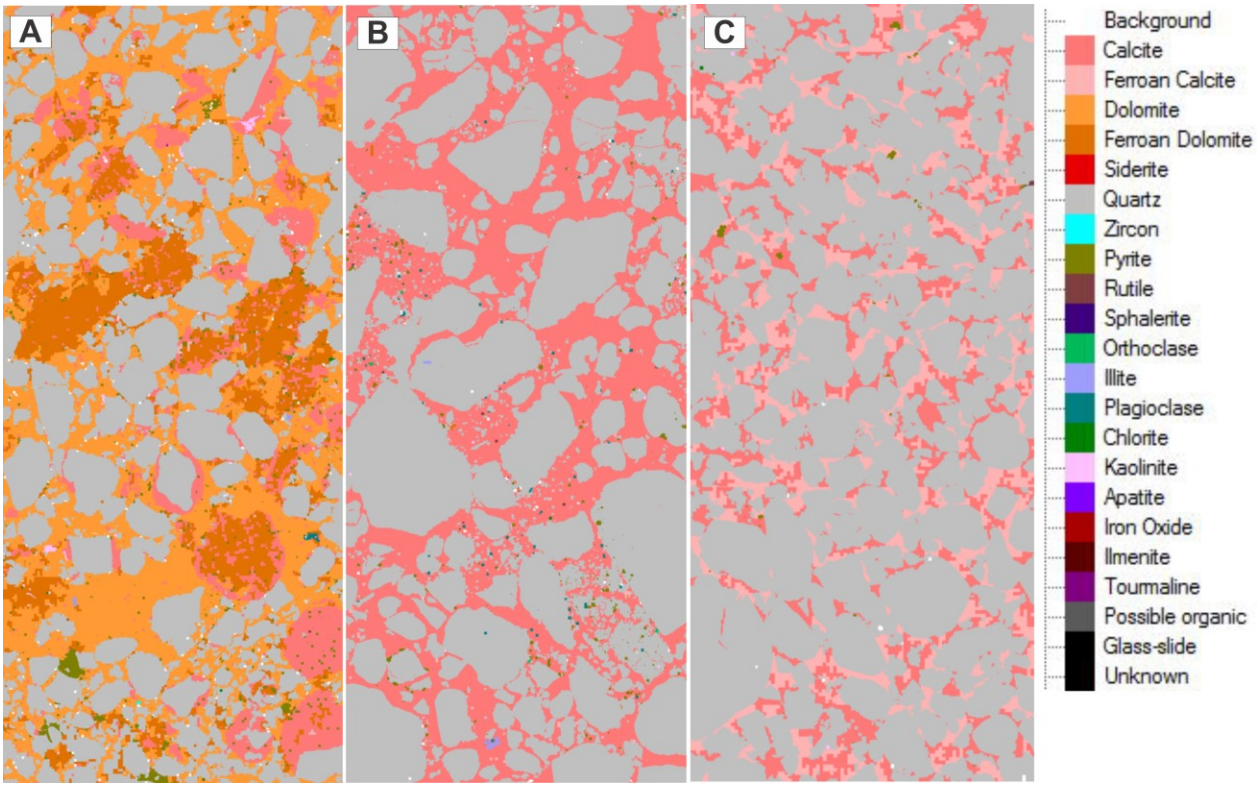

Figure 24. SEM-MLA maps of thin sections for A) dolomite-cemented sandstone, B) calcite-cemented sandstone, and C) ferroan calcite-cemented sandstone. Note the difference among the intergranular volumes of each sample. The dolomite and calcite-cemented sandstones preserve the higher intergranular volume compared to the ferroan calcite cemented sample. Sample S12 (A), S14 (B), S17 (C).

2.4.5 Stable isotope geochemistry

The isotopic and elemental compositions of the investigated cements are tabulated in Table 3 and 4. Despite the wide range in the $\delta^{18}O$ values (-10.2 to -1.2 ‰ VPDB) of the investigated cements from the Lower Hibernia zone, their $\delta^{13}C$ values (-23.9 to 0.6 ‰ VPDB) overlap significantly except for some calcite samples that are distinctively depleted (-23.9 to -14.5 ‰ VPDB; Figure 25). Furthermore, $\delta^{18}O$ and $\delta^{13}C$ values of carbonate cements form clusters dependent on the cement type (Figure 25A). Dolomite cements have the highest values of $\delta^{18}O$ and $\delta^{13}C$ among the other carbonate cements in the Lower Hibernia zone ($\delta^{18}O_{dolomite}$= -4.1 to -1.6 ‰ VPDB; $\delta^{13}C_{dolomite}$= -11.8 to 0.6 ‰ VPDB; Table 3). Calcite cements show more depleted $\delta^{18}O$ and $\delta^{13}C$ signatures than dolomite ($\delta^{18}O_{calcite}$= -7.6 to -4.2; -5.8 ± 1.2 ‰ VPDB and $\delta^{13}C_{calcite}$= -23.9 to -2.5,

-10.0 ± 7.3 ‰ VPDB, n= 14). Ferroan calcite exhibit also narrower ^{18}O and ^{13}C trends, being distinctively more depleted in ^{18}O than any other carbonate cement ($\delta^{18}O_{ferroancalcite}$= -10.2 to -9.1, -9.5 ± 0.3 ‰ VPDB, n = 16; $\delta^{13}C_{ferroancalcite}$= -13.1 to -4.9, -8.2 ± 2.3 ‰ VPDB n = 16). The number of ferroan dolomite and grain-rimming micrite samples analyzed for their $\delta^{13}C$ and $\delta^{18}O$ compositions is limited due to the challenges in micro-drilling without contamination from surrounding carbonate phases.

The carbon and oxygen isotopic values of the ferroan calcite plot in a separate and identifiable cluster as illustrated in $\delta^{13}C$ vs. $\delta^{18}O$ space (Figure 25). Siderite and sphaerosiderite cements exhibit a significant contrast in their $\delta^{13}C$ signature ($\delta^{13}C_{siderite}$= -5.2 to -1.6, -3.3 ± 1.5 ‰ VPDB, n= 4; $\delta^{13}C_{sphaerosiderite}$= -13.4 to -11.3, -8.2 ± 1.4 ‰ VPDB, n= 2), while their $\delta^{18}O$ show slight disparity ($\delta^{18}O_{siderite}$: -8.2 to -3.1, -5.6 ± 2.7 ‰ VPDB, n= 4; $\delta^{18}O_{sphaerosiderite}$= -1.3 to -1.2, -1.2 ± 1.4 ‰ VPDB, n= 2). In addition, the isotopic signatures of carbonate cements also plot in identifiable clusters when considering facies associations and reservoir units (Figure 25B). For instance, the $\delta^{13}C$ composition of calcite cements range from the most depleted $\delta^{13}C$ values in marginal marine tidal fluvial channels (FA3) in Layer 3 ($\delta^{13}C$ = -23.9 to -14.5; -18.9 ± 3.8 ‰ VPDB, n= 5), with values increasing upward into the marine offshore (FA5) Medial Shale ($\delta^{13}C$ = -6.7 to -5.8, -6.2 ± 0.3 ‰ VPDB, n= 5), and increasing slightly on average upward into tidal facies (FA6) of Layer 1 (-4.1 to -2.5; -3.5 ± 0.9 ‰ VPDB, n= 3). Ferroan calcite in the same unit have intermediate $\delta^{13}C$ values (-6.4 to -5.3, -6.0 ± 0.6 ‰ VPDB, n= 3) and the lowest $\delta^{18}O$ values (-10.2 to -9.1, -9.5 ± 0.6 ‰ VPDB, n= 3), with values of both notably overlapping with that of ferroan calcite cements in FA4 and FA5. Finally, upon excluding calcite and sphaerosiderite of FA3 and FA4, a discernible trend is recognized transitioning from dolomite-siderite, through calcite-siderite to ferroan calcite.

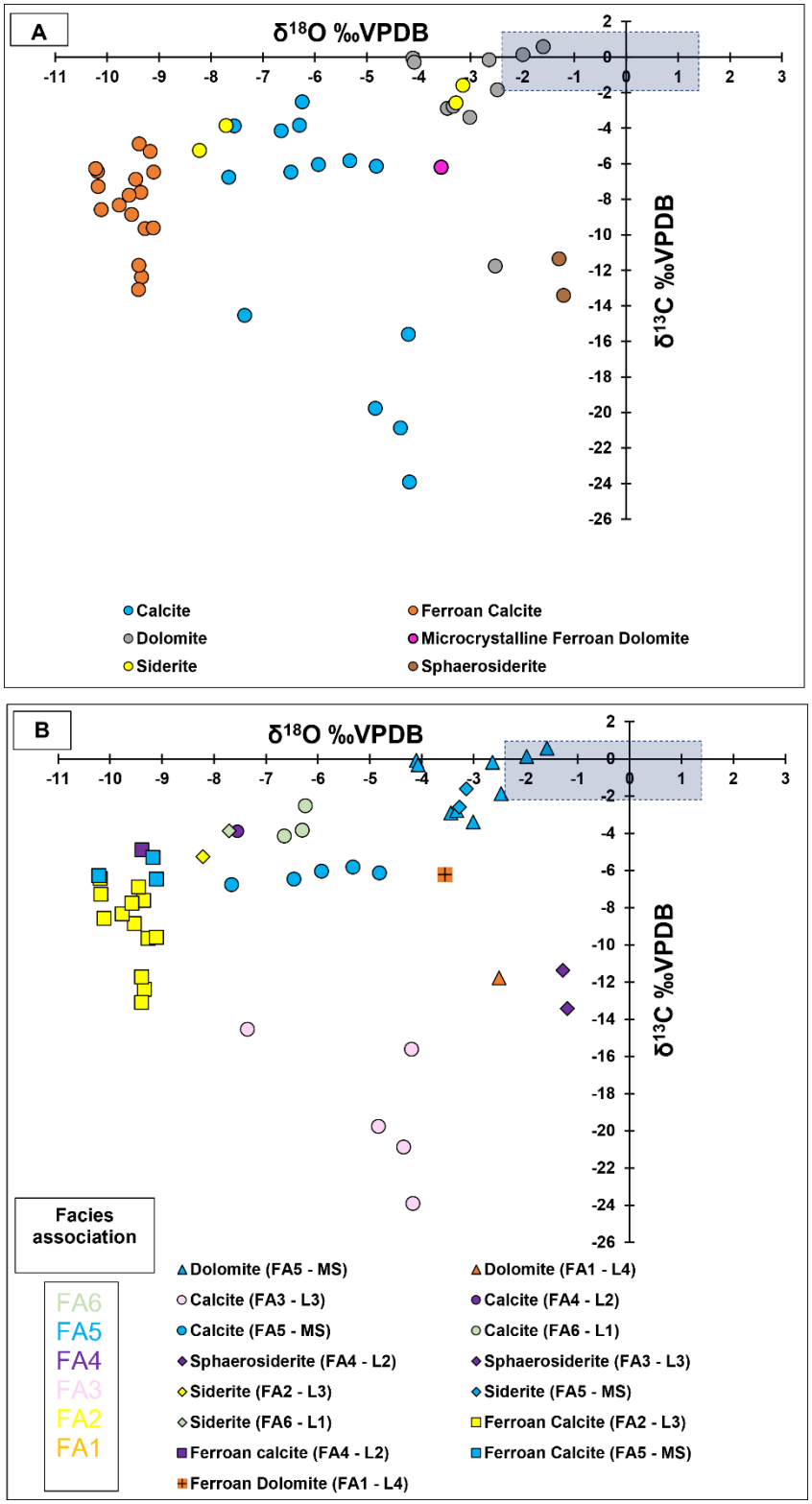

Figure 25. Scatter diagrams of $\delta^{18}O$ vs $\delta^{13}C$ of the analyzed carbonate cements and classified based on A) cement type B) cement type and facies associations. The grey square mark the isotopic composition of the best preserved early cretaceous marine carbonates from Veizer et al.(1999).

Table 3. $\delta^{18}O$ vs $\delta^{13}C$ values for carbonate cements

Well	FA/RU*	Sample	Depth (m)	Carbonate cement	$\delta^{13}C$ VPDB	$\delta^{18}O$ VPDB	δ18O parent fluid T= 25°C	δ18O parent fluid T= 30°C	δ18O parent fluid T= 35°C
B-16 2	FA6 (L1)	M2	4199.10	Calcite	-2.53	-6.24	-4.13	-3.72	-2.71
B-16 12	FA6 (L1)	M7	5921.93	Calcite	-4.17	-6.64	-4.55	-4.13	-3.13
B-16 12	FA6 (L1)	M8	5921.88	Calcite	-3.85	-6.29	-4.19	-3.77	-2.77
B-16 28	FA4 (L2)	M31	7103.34	Calcite	-3.90	-7.55	-5.48	-5.07	-4.06
B-16 55	FA3 (L3)	M15	7194.44	Calcite	-15.62	-4.19	-2.02	-1.60	-0.60
B-16 55	FA3 (L3)	M16	7193.98	Calcite	-19.79	-4.83	-2.68	-2.26	-1.26
B-16 55	FA3 (L3)	M16.2	7193.70	Calcite	-14.56	-7.35	-5.28	-4.86	-3.86
B-16 55	FA3 (L3)	M26	7201.57	Calcite	-23.93	-4.17	-2.00	-1.58	-0.58
B-16 55	FA3 (L3)	M27	7194.14	Calcite	-20.90	-4.34	-2.18	-1.76	-0.76
B-16 28	FA5 (MS)	M18C	7157.65	Calcite	-5.84	-5.32	-3.19	-2.77	-1.77
B-16 28	FA5 (MS)	M18C2	7157.65	Calcite	-6.06	-5.92	-3.81	-3.39	-2.39
B-16 28	FA5 (MS)	M34	7157.82	Calcite	-6.78	-7.65	-5.59	-5.18	-4.17
B-16 28	FA5 (MS)	M35	7157.62	Calcite	-6.49	-6.45	-4.35	-3.94	-2.94
B-16 28	FA5 (MS)	M36	7157.42	Calcite	-6.16	-4.81	-2.66	-2.24	-1.24
B-16 54W	FA5 (MS)	M9	7002.94	Dolomite	-0.18	-2.64	-4.77	-4.29	-3.14
B-16 54W	FA5 (MS)	M11	7004.15	Dolomite	0.13	-1.99	-4.10	-3.62	-2.47
B-16 54W	FA5 (MS)	M28	7004.30	Dolomite	0.58	-1.59	-3.70	-3.22	-2.06
B-27	FA5 (MS)	M42	3861.80	Dolomite	-1.86	-2.47	-4.60	-4.13	-2.97
B-27	FA5 (MS)	M43	3861.75	Dolomite	-3.40	-3.01	-5.15	-4.68	-3.52
B-27	FA5 (MS)	M44	3868.15	Dolomite	-2.91	-3.44	-5.60	-5.12	-3.97
B-27	FA5 (MS)	M45	3868.15	Dolomite	-2.78	-3.33	-5.48	-5.01	-3.85
B-16 17	FA5 (MS)	M49	3985.17	Dolomite	-0.07	-4.10	-6.28	-5.81	-4.65
B-16 17	FA5 (MS)	M51	3990.30	Dolomite	-0.31	-4.08	-6.25	-5.78	-4.62
B-16 55	FA1 (L4)	M12	7273.24	Dolomite	-11.77	-2.51	-4.65	-4.17	-3.01
B-16 54W	FA5 (MS)	M28	7004.34	Dolomite	0.58	-1.59	-3.70	-3.22	-2.06
B-16 54W	FA5 (MS)	M10S	7002.80	Siderite	-2.59	-3.27	-4.43	-3.96	-2.83
B-16 54W	FA5 (MS)	M10.2	7002.70	Siderite	-1.61	-3.14	-4.29	-3.82	-2.69
B-16 28	FA6(L1)	M5	7112.83	Siderite	-11.38	-1.29	-2.38	-1.91	-0.78
B-27	FA3(L3)	M46	3909.89	Siderite	-13.43	-1.20	-2.29	-1.82	-0.69
B-16 12	FA6 (L1)	M8	5927.88	Siderite	-3.87	-7.71	-9.00	-8.53	-7.40
C-96	FA2(L3)	M17	3925.70	Siderite	-5.26	-8.21	-9.52	-9.05	-7.92
B-16 55	FA1 (L4)	M12F	7273.24	Ferroan Dolomite	-6.22	-3.56	-5.72	-5.24	-4.09

δ18O Sw = -0.4 to 0.65 ‰ SMOW and δ18O Mw= -4.4 to -3.3 ‰ SMOW

FA = Facies Associations. RU = Reservoir Unit. PF= Parental Fluid

Table 4. $\delta^{18}O$ vs δ13C values for ferroan calcite cements

Well	FA/RU*	Sample	Depth (m)	Carbonate cement	$\delta^{13}C$ VPDB	$\delta^{18}O$ VPDB	δ18O parent fluid T= 45°C	δ18O parent fluid T= 55°C
B-16 28	FA4(L2)	M32	7108.08	Ferroan Calcite	-4.91	-9.38	-4.08	-2.38
B-16 55	FA2 (L3)	M13	7252.75	Ferroan Calcite	-8.88	-9.53	-4.24	-2.54
B-16 55	FA2 (L3)	M14	7238.70	Ferroan Calcite	-7.63	-9.35	-4.05	-2.35
B-16 55	FA2 (L3)	M20	7267.00	Ferroan Calcite	-8.36	-9.76	-4.48	-2.78
B-16 55	FA2 (L3)	M22	7238.25	Ferroan Calcite	-7.78	-9.57	-4.28	-2.58
B-16 55	FA2 (L3)	M23	7237.50	Ferroan Calcite	-7.30	-10.17	-4.90	-3.20
B-16 55	FA2 (L3)	M24	7234.31	Ferroan Calcite	-8.59	-10.11	-4.84	-3.14
B-16 55	FA2 (L3)	M25	7233.82	Ferroan Calcite	-6.45	-10.18	-4.91	-3.21
B-16 55	FA2 (L3)	M30	7273.90	Ferroan Calcite	-6.90	-9.45	-4.15	-2.45
B-27	FA2 (L3)	M38	3905.40	Ferroan Calcite	-12.41	-9.33	-4.04	-2.34
B-27	FA4 (L3)	M39	3869.00	Ferroan Calcite	-13.11	-9.39	-4.09	-2.40
B-16 55	FA2 (L3)	M16T	7193.98	Ferroan Calcite	-9.66	-9.26	-3.97	-2.27
B-16 55	FA2 (L3)	M16T2	7193.70	Ferroan Calcite	-9.62	-9.10	-3.80	-2.10
B-27	FA3 (L3)	M39T	3891.15	Ferroan Calcite	-11.74	-9.39	-4.09	-2.39
B-27	FA5 (MS)	M40	3870.20	Ferroan Calcite	-6.29	-10.21	-4.94	-3.24
B-27	FA5 (MS)	M41	3861.70	Ferroan Calcite	-6.48	-9.10	-3.80	-2.10
B-16 28	FA5 (MS)	M3	7149.50	Ferroan Calcite	-5.32	-9.16	-4.77	-2.16

δ18O Sw = -0.4 to 0.65 ‰ SMOW and δ18O Mw= -4.4 to -3.3 ‰ SMOW

FA = Facies Associations. RU = Reservoir Unit. PF= Parental Fluid

2.4.6 Elemental geochemistry

Table 5 summarizes the concentrations of iron, magnesium, manganese, in carbonate cements, including rare earth elements (REE). The siderite cements contain, as expected, the highest Fe concentrations (387333 ± 36821 ppm) followed by ferroan dolomite (69007± 17527 ppm) and ferroan calcite (13385 ± 3832 ppm). In addition, calcite cements exhibit the lowest iron concentrations among the investigated carbonate cements (662 ± 1552 ppm). Conversely Mg concentrations are higher in calcite (17462 ± 1330 ppm) than in ferroan calcite (2742 ± 840 ppm). Siderite is the most enriched in Mn (5198 ± 2794 ppm). Calcite, ferroan calcite, dolomite and ferroan dolomite show similar Mn concentrations (Table 5; Figure 26), which increase with increasing Fe and with decreasing Sr concentrations. The mean total REE (∑REE) values for ferroan calcite and ferroan dolomite (47 ± 4 ppm and 144 ± 14 ppm, respectively; Table 5) are higher than their low-Fe counterparts (1 ± 0.1 and 73 ± 8 respectively; Table 5). The shale-normalized rare earth elements (REE_{SN}) patterns (relative to PAAS) of the carbonate cements (Figure 27), exhibit no negative Ce anomalies but an enrichment in middle REEs, and slight heavy and light REE depletion.

Table 5. Trace element statistics of the investigated carbonate cements.

		Mg	Fe	Mn	Sr	Y	U	La	Ce	Pr	Nd
Non-ferroan calcite n=28	**Mean**	**17462**	**662**	**2689**	**587**	**2.97**	**0.05**	**0.84**	**2.25**	**0.32**	**1.54**
	Min	12860	10	2120	519	0.43	0.00	0.12	0.25	0.03	0.13
	Max	19420	7040	3713	687	11.40	0.05	3.32	9.60	1.31	7.19
	Stan. Dev.	1330	1552	543	49	2.62	0.05	0.91	2.50	0.34	1.76
Ferroan Calcite n=41	**Mean**	**2742**	**13385**	**2131**	**712**	**18.01**	**0.35**	**4.99**	**12.88**	**1.90**	**10.30**
	Min	751	4310	1601	333	1.62	0.00	0.82	1.45	0.16	0.88
	Max	4880	22600	2708	1703	80.10	2.90	20.00	64.10	11.88	72.60
	Stan. Dev.	840	3832	219	280	15.96	0.69	3.89	12.36	2.22	13.37
Dolomite n=11	**Mean**	**94790**	**6932**	**1779**	**333**	**15.80**	**0.90**	**13.03**	**27.96**	**3.31**	**14.01**
	Min	93700	2970	1602	323	8.11	0.34	8.22	15.20	1.86	7.42
	Max	96500	15800	1920	339	21.75	1.33	16.17	36.60	4.32	18.04
	Stan. Dev.	924	3363	96	5	3.79	0.26	2.23	5.92	0.71	3.03
Microcrystalline ferroan dolomite n= 11	**Mean**	**71418**	**49145**	**2277**	**464.23**	**12.49**	**0.74**	**19.49**	**43.20**	**4.98**	**19.65**
	Min	38000	38500	1343	321.20	9.31	0.46	15.47	33.50	4.08	16.72
	Max	83700	71200	2620	590.00	20.30	1.66	27.28	58.60	6.79	27.44
	Stan. Dev.	11754	8360	366	103.17	3.65	0.34	3.04	6.23	0.72	3.16
Saddle Ferroan Dolomite n=17	**Mean**	**85906**	**81859**	**1797**	**351.56**	**41.56**	**2.63**	**12.68**	**48.03**	**8.16**	**43.08**
	Min	79600	72200	1699	253.00	34.00	1.63	11.27	41.40	6.99	35.90
	Max	95900	91800	1964	511.00	50.60	3.93	14.42	53.60	9.31	50.20
	Stan. Dev.	4403	5291	73.75	65.01	4.24	0.68	0.88	3.58	0.62	3.57
Siderite n=21	**Mean**	**23754**	**387333**	**5198**	**170**	**32.61**	**3.09**	**8.25**	**22.90**	**2.88**	**13.57**
	Min	17400	289000	3460	97	7.90	0.99	2.41	5.43	0.83	4.14
	Max	46700	433000	14200	338	126.00	4.89	28.20	102.00	10.30	46.90
	Stan. Dev.	8814	36822	2794	63	38.97	0.98	8.12	26.35	2.92	13.56

		Gd	Tb	Dy	Ho	Er	Tm	Yb	Lu	REE	Ce/Ce*
Non-ferroan calcite n=28	**Mean**	**0.81**	**0.11**	**0.53**	**0.10**	**0.25**	**0.03**	**0.19**	**0.03**	**7.72**	**1.14**
	Min	0.06	0.02	0.07	0.01	0.05	0.01	0.03	0.01		0.83
	Max	3.94	0.38	1.99	0.35	0.79	0.11	0.73	0.08		1.57
	Stan. Dev.	0.89	0.10	0.50	0.09	0.22	0.03	0.17	0.02	0.64	0.18
Ferroan Calcite n=41	**Mean**	**5.52**	**0.63**	**3.02**	**0.51**	**1.15**	**0.14**	**0.73**	**0.10**	**46.79**	**1.00**
	Min	0.37	0.03	0.15	0.04	0.08	0.00	0.05	0.01		0.62
	Max	40.50	4.07	17.50	2.63	4.77	0.48	2.70	0.38		1.61
	Stan. Dev.	7.58	0.78	3.37	0.51	1.06	0.13	0.66	0.09	3.94	0.25
Dolomite n=11	**Mean**	**3.67**	**0.52**	**2.94**	**0.54**	**1.45**	**0.20**	**1.12**	**0.17**	**73.08**	**1.03**
	Min	1.75	0.22	1.40	0.24	0.61	0.09	0.49	0.08		0.94
	Max	5.25	0.73	4.31	0.83	2.18	0.30	1.57	0.26		1.15
	Stan. Dev.	0.90	0.14	0.81	0.16	0.44	0.06	0.33	0.05	7.92	0.06
Microcrystalline ferroan dolomite n= 11	**Mean**	**3.90**	**0.53**	**2.82**	**0.51**	**1.28**	**0.17**	**0.95**	**0.14**	**102.84**	**0.99**
	Min	2.92	0.43	2.12	0.39	0.93	0.11	0.66	0.10		0.94
	Max	5.74	0.82	4.00	0.77	2.07	0.34	2.08	0.32		1.03
	Stan. Dev.	0.92	0.12	0.57	0.13	0.35	0.06	0.40	0.07		0.03
Saddle Ferroan Dolomite n=17	**Mean**	**17.04**	**2.25**	**11.20**	**1.76**	**3.97**	**0.46**	**2.58**	**0.37**	**171.09**	**0.90**
	Min	13.90	1.89	9.12	1.43	3.25	0.37	2.09	0.27		0.84
	Max	21.38	2.85	13.58	2.15	4.63	0.56	3.13	0.45		0.97
	Stan. Dev.	1.82	0.23	1.25	0.19	0.40	0.05	0.28	0.05		0.03
Siderite n=21	**Mean**	**7.03**	**1.00**	**6.29**	**1.20**	**3.20**	**0.47**	**3.04**	**0.44**	**77.19**	**1.00**
	Min	2.05	0.28	1.46	0.24	0.70	0.10	0.58	0.07		0.76
	Max	27.00	3.11	22.30	4.40	10.40	1.75	13.50	1.39		1.30
	Stan. Dev.	7.39	1.04	7.30	1.42	3.76	0.59	3.94	0.53	6.22	0.14

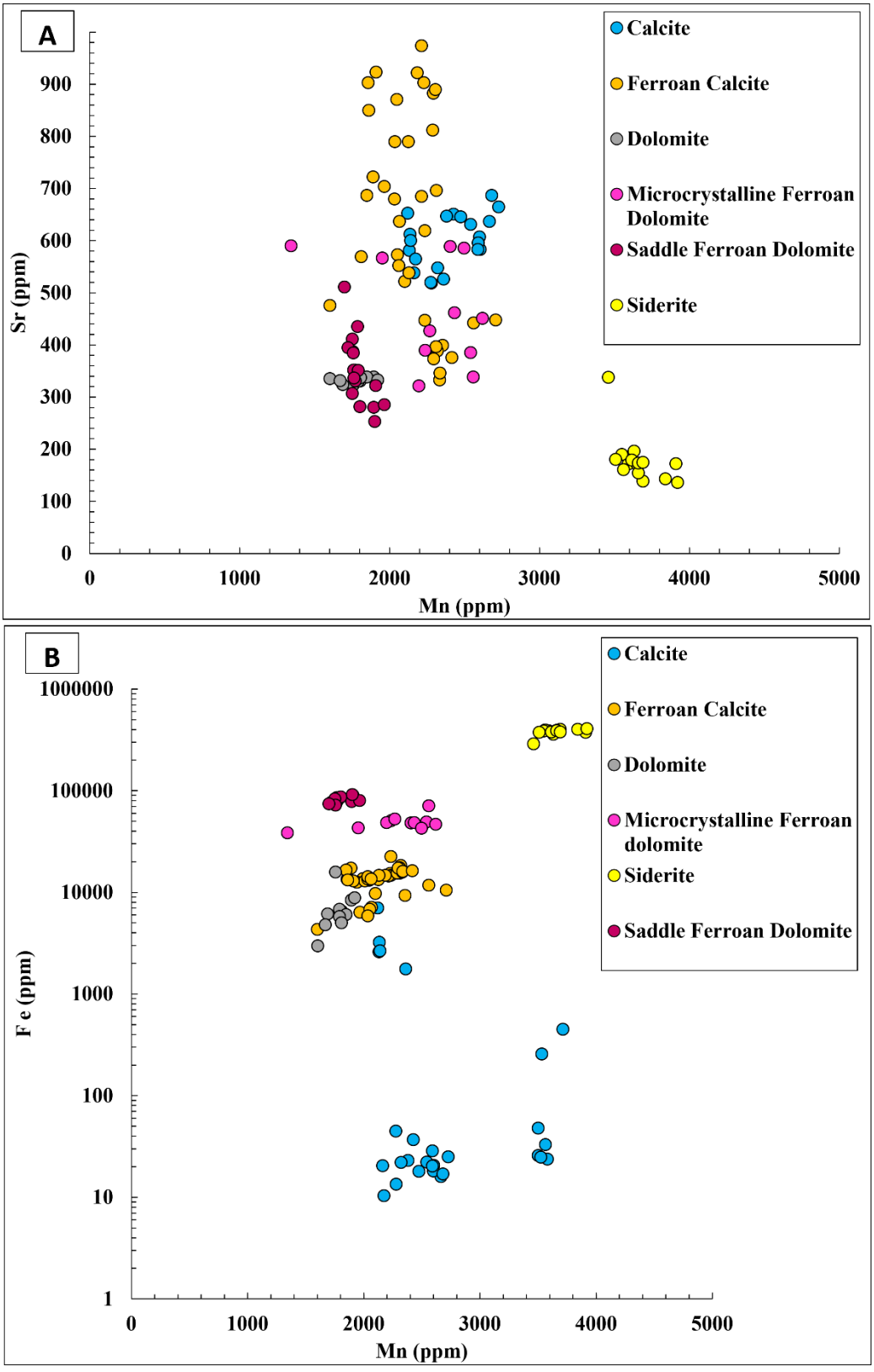

Figure 26. Scatter diagrams of Sr vs Mn and Fe vs Mn for carbonate cements.

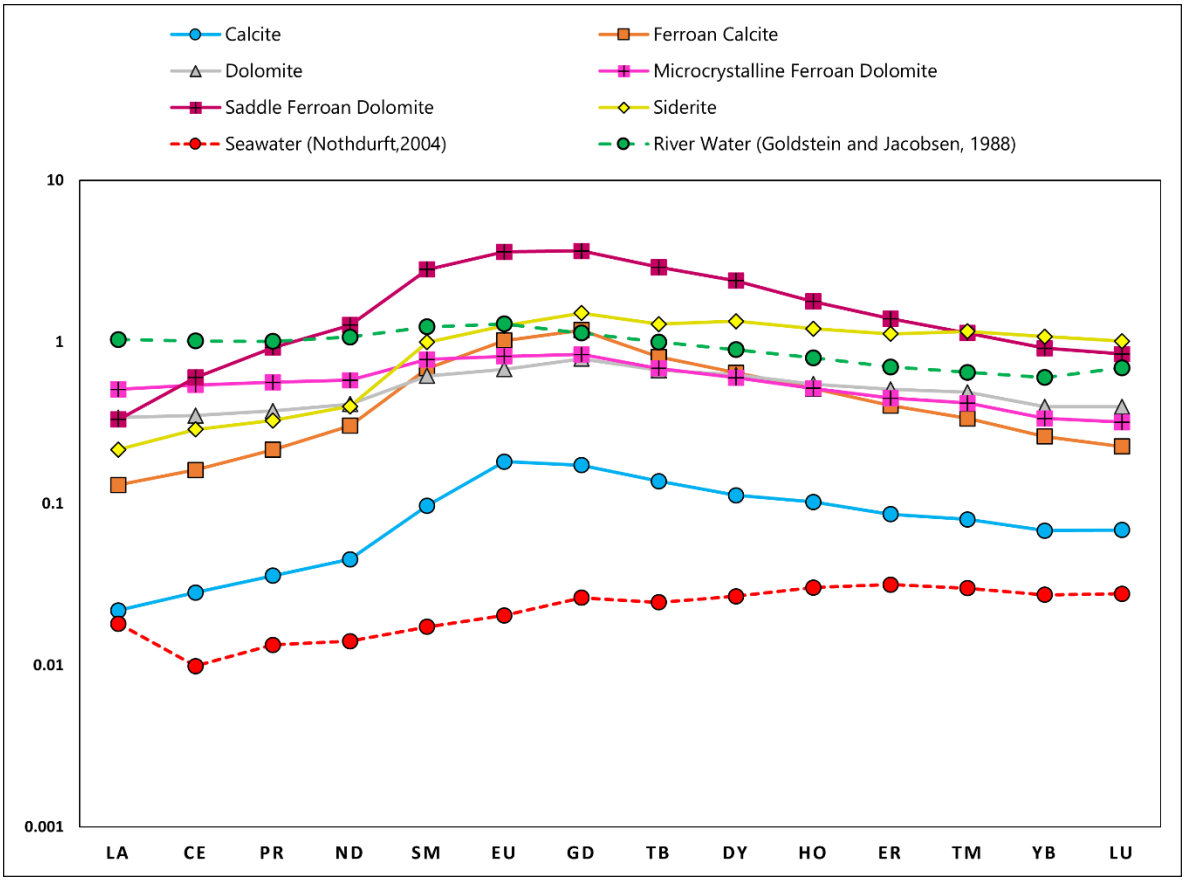

Figure 27. Shale-normalized (PAAS) REE patterns of carbonate cements (REE_{SN}) in the Lower Hibernia zone, Lennard Shelf cements that reflects the REE seawater pattern (Nothdurft et al., 2004) and the REE pattern of suspended load from modern river water that reflects the fluvial input pattern (Goldstein and Jacobsen, 1988).

2.5 Discussion

2.5.1 Stratal evolution of the Lower Hibernia zone

The vertical facies succession of the Lower Hibernia zone records the transition from a deltaic to an estuarine environment punctuated by two regressive sequence boundaries, as illustrated in Figure 28 and Figure 29. Starting at its base, Facies Association 1 within Layer 4 overlies siliciclastic strata of the Fortune Bay Formation that record six stacked sequences of shale grading upward to siltstone indicating prodeltaic and delta front sedimentation (McAlpine, 1990; Hurley et al., 1992). In this framework, the delta front deposits in FA1 record deltaic progradation

characterizing the highstand systems tract (HST) of an underlying distal deltaic sequence. The erosive surface separating FA1 from the overlying terrestrial braided fluvial strata of FA2 suggests erosion of delta front strata coinciding with regression prior to the onset of fluvial sedimentation. This regressive unconformity is interpreted as a sequence boundary representing an abrupt drop in relative sea level that might be linked to the uplift and and erosion of the rift flanks (Tankard and Welsink, 1987; Tankard and Balkwill, 1989). This is evidenced in the Hibernia stratigraphic record as a forced regression, resulting in fluvial incision during an abrupt base-level fall. The coeval exposure and erosion of the rift flanks and Avalon Uplift resulted in renewed clastic sediment generation (Sinclair, 1988; Tankard et al., 1989; Hiscott et al., 1990) and the braided fluvial sedimentation of FA2 above this regressive surface. Fluvial aggradation of FA2 comprising the lowest two-thirds parts of the Layer 3 (Layer 3 Lower; Figure 28) may record purely terrestrial fluvial sedimentation and/or proximal delta plain sedimentation feeding a coeval delta front strata farther into the basin. In any case, it overlies a major regressive unconformity interpreted as sequence boundary and represents the lowest accommodation setting at the base of the succeeding sequence, thus representing the lowstand systems tract (LST).

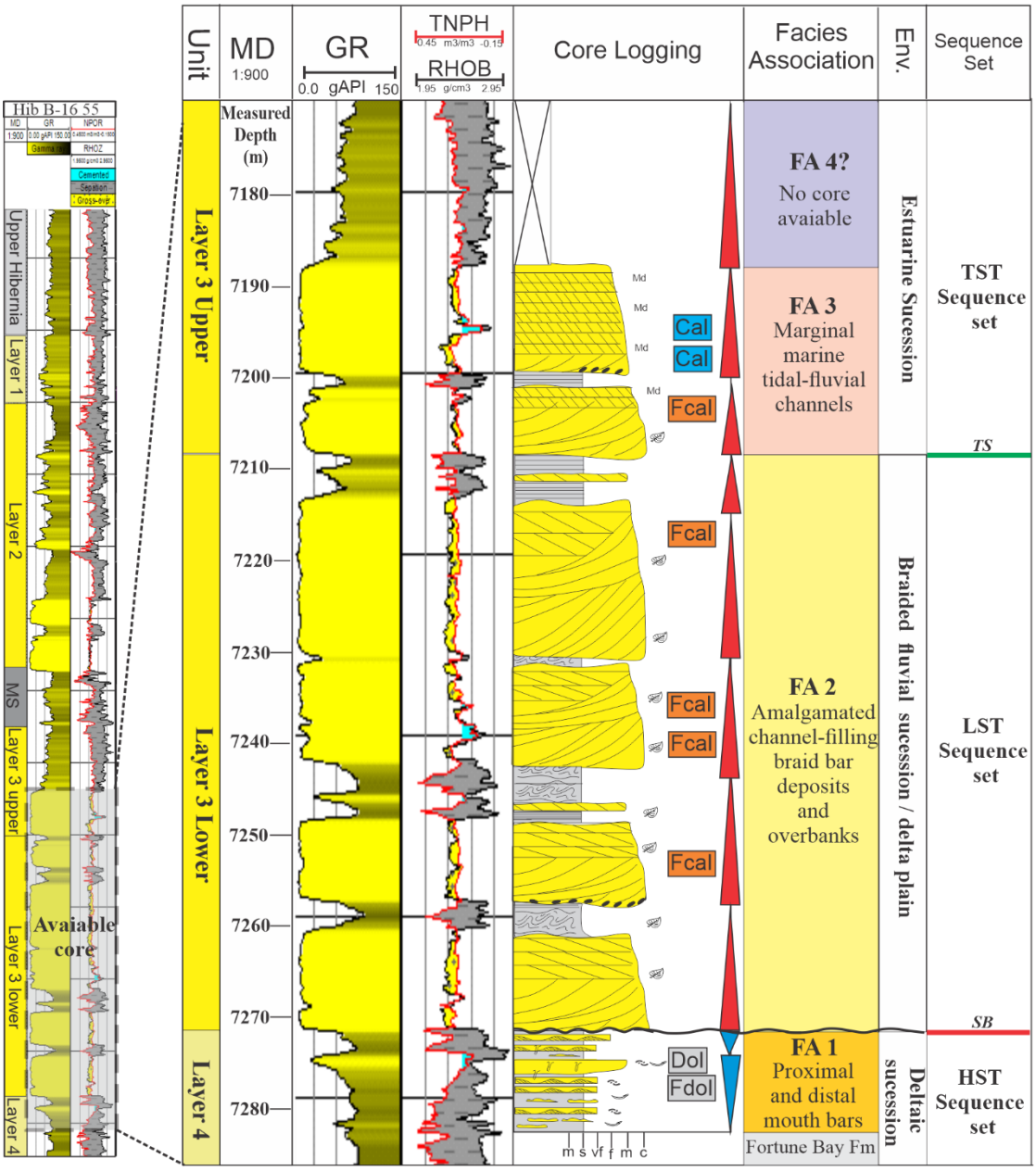

Figure 28. Vertical distribution of facies association in the Layer 4 and Layer 3 of the Lower Hibernia zone. Since B-16 55 is located in a proximal area the the amalgamated braided in-channels bars become thicker and the tidal-fluvial bars tinner.

The stacked successions of FA2 transitionally shift to fining upward successions of marginal marine channels (FA3) and tidal flat deposits (FA4) which comprise Layer 3 Upper (L3U; Figure 28). These strata were deposited during the transgression of the braided fluvial system and represent

the fluvial tidal transition of a tide-dominated estuarine system. In addition, the diversity of the ichnogenera in the braided fluvial and tidal fluvial facies is relatively low because of the reduced salinity conditions and trace-fossil assemble consisting of a mixing of vertical, dwelling burrows of the *Skolithos* ichnofacies and horizontal burrows of the *Cruziana* ichnofacies. The marine offshore deposits of FA5 gradationally overlie tidal flats strata, indicating a marine inundation and coinciding decrease in the supply of siliciclastic sediment to the JDB has been recorded widely in the Hibernia field (Sinclair et al., 2005). At this time, increased subsidence rates resulted in a progressive sea-level rise that led to the retrogradation of the delta/braided fluvial system and the development of a mud-dominated shelf. In addition, *Cruziana* trace fossils become more abundant in FA4, FA5 and FA6, which represent the intertidal and subtidal zones of the estuary. In sequence stratigraphic terminology Layer 3 Upper and the lower part of the Medial Shale (FA3, FA4 and FA5) record the transgressive systems tract. The maximum flooding surface is marked by the build-up of corals, which indicate the most clastic sediment-starved conditions. Overlying this are minor estuarine strata (FA4) that appear to record the onset of progradation, and thus are interpreted as the highstand systems tract.

The next sequence boundary occurs at the base of Layer 2 and is marked by an abrupt erosional unconformity overlain by marginal marine tidal fluvial channel strata (FA3). This marks a second forced regression, coinciding with a lowstand fluvial incision followed by increased clastic input. These strata record the onset of the transgressive systems tract following fluvial incision, and were succeeded by tidal flats (McAlpine, 1990; Figure 29). The final episode of sedimentation in the Lower Hibernia zone is defined by a sea-level rise possibly due to increased subsidence rates, recorded by the repetitive coarsening-upward successions of subtidal sand bars in FA6 (Layer 1).

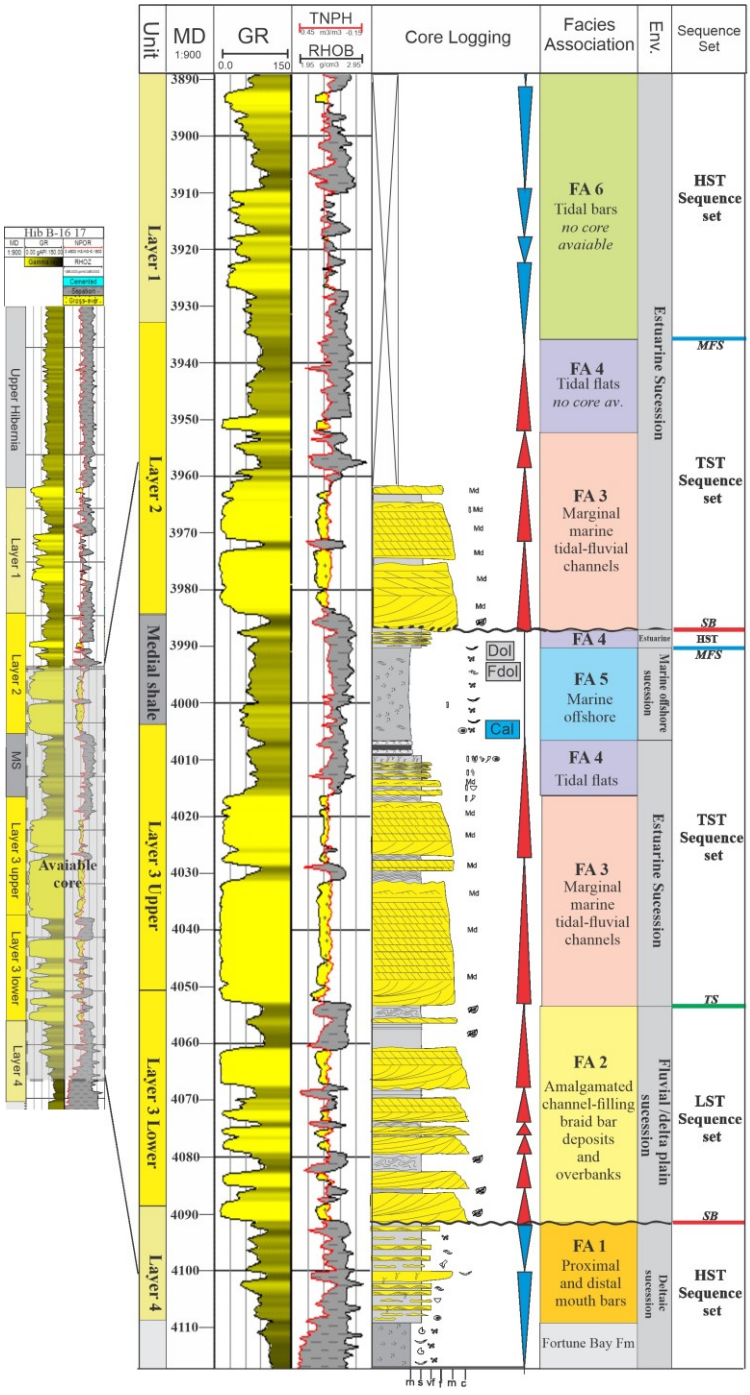

Figure 29. Vertical distribution of facies association in the Layer 4 and Layer 3, Medial Shale and Layer 2 of the Lower Hibernia zone. Hibernia B-16 17 is located in distal area, developing more tidal bars in Layer 1 and marginal marine channels in L3U and L2.

2.5.2 Paragenetic sequence and relative timing of carbonate precipitation

Figure 30 summarizes the paragenetic sequences of the Lower Hibernia zone based on textural relationships and intergranular volume estimates. Strata of the Lower Hibernia zone exhibit both non-pervasive and pervasive carbonate cements, indicating diverse stages of cementation during diagenesis. Grain-rimming micrite occurs in shallow-marine sandstones of FA1, forming irregularly distributed thin coatings around shells and detrital grains (Figure 21A). Cements with similar micromorphology have been linked to shallow carbonate precipitation occurring in intertidal or low supratidal or vadose zoned triggered by carbon dioxide evaporation and algal photosynthesis (Hanor, 1978; Chafetz et al., 1985; Holail and Rashed, 1992; Morad, 1998).

Microcrystalline siderite cements partially fill intergranular space in sandstone with high intergranular volumes, indicating pre-burial siderite cementation that predated calcite and ferroan calcite cements. The millimetre-scale sphaerosiderite in fluvial-tidal strata of FA3 and FA4, shows a distinctive microcrystalline core with a coarser crystalline crust (Figure 22C-D). They coexist with coarse- and fine-grained pyrite filling intergranular space (Figure 22I). Sphaerosiderites are well known as diagenetic products of reducing water-saturated soil systems in modern and ancient wetland environments (e.g., swamps) driven by bacterial reduction of manganese (Mn) and iron (Fe) along with bicarbonate production resulting from the degradation of organic matter (Moore et al., 1992; Choi et al., 2003; Ludvigson et al., 2013; Weibel et al., 2016). In addition, the occurrence of sphaerosiderite along with pyrite, as evidenced in FA3 and FA4 strata, is associated with the infiltration of brackish waters (Sengupta et al., 2021).

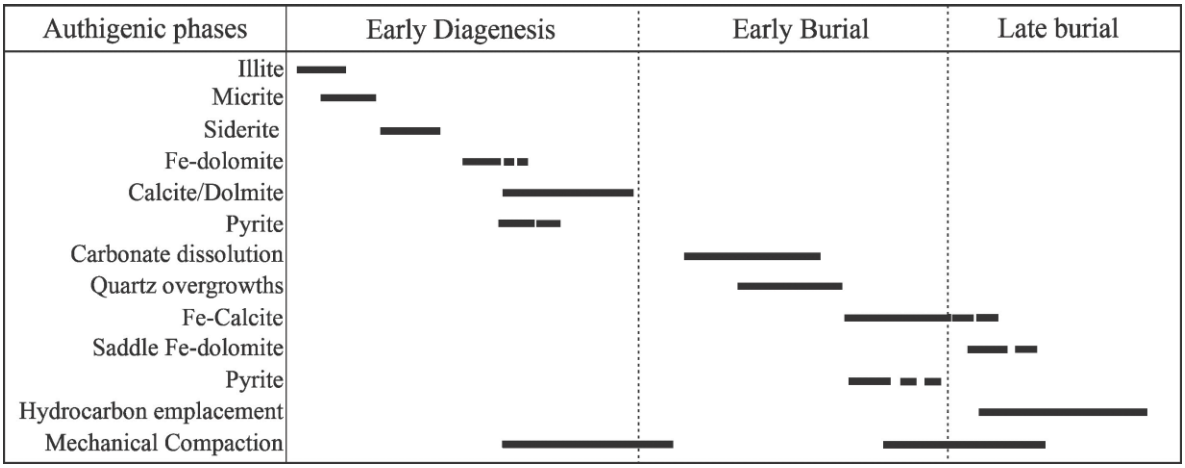

Figure 30. Paragenetic sequence of the Lower Hibernia zone.

The main pervasive cement phases of the Lower Hibernia zone include calcite, dolomite and ferroan calcite. Their petrographic textures, fabrics and intergranular volumes offer insight into the relative timing of carbonate cementation (e.g., Loucks et al., 1977; Milliken et al., 1998; Morad, 1998; Fröhlich et al., 2009). In sandstones of FA1, subhedral to anhedral dolomite crystals typically exhibit a planar-s fabric (Figure 21), which indicates slow crystal growth at low temperatures from fluids that were supersaturated with respect to dolomite (Sibley and Gregg, 1987; Rahimi et al., 2016). Additionally, blocky dolomite crystals form intergranular mosaics, a common feature attributed to shallow phreatic cementation (Scholle and Ulmer-Scholle, 2003; Flügel, 2010). The intergranular volume (IGV) of dolomite-cemented sandstones is similar (~38%) to the likely initial IGV at deposition (42%; Beard and Weyl, 1973), evidencing pre-compaction cementation (Figure 24). Dolomite cements widely coexist with minor pyrite (Figure 23B), indicating that parent fluids contained sulphate ions which were reduced to sulphide (e.g., pyrite) during dolomite cementation. Rare microcrystalline ferroan dolomite cement also occurs within dolomite cemented sandstone, mainly replacing bioclasts, partially fill intergranular space, and forming rare thin coats around detrital grains. The coexistence of ferroan dolomite, pyrite and dolomite suggests that pore waters evolved from iron-reducing to sulphate-reducing conditions, incorporating Fe^{2+} into ferroan

dolomite first and then pyrite. Consequently, the subsequent dolomite became depleted in iron due to the reduction of sulphate and incorporation of iron into coeval sulphide minerals (Baker and Kastner, 1981; Gautier and Claypool, 1984; Morad, 1998).

Poikilotopic calcite cements fill intergranular pore space and partially replace detrital grains (e.g., quartz, feldspars, carbonates; Figure 20A-B). Calcite-cemented sandstone usually shows a grain-floating texture with high intergranular volume (~ 33-35%) and common point grain contacts (Figure 24B). These petrographic features along with the absence of two-phase fluid inclusions suggest that calcite cements likely precipitated during early diagenesis before any significant compaction, similar to dolomite and ferroan dolomite cements.

Ferroan calcite cements occur at different intervals of the Lower Hibernia zone, filling both intergranular and intragranular pore spaces in sandstone and siltstone. Sandstone cemented with ferroan calcite have a reduced intergranular volume (23 – 28 % IGV) compared to those cemented with calcite or dolomite. Ferroan calcite crystals enveloping fractured grains and filling fractures indicate that ferroan calcite cementation occurred in a more compacted sandstone likely during burial. Furthermore, solid bitumen coexists with ferroan calcite and pyrite (Figure 22A-B; Figure 23C-D), forming fluid-like patches along fractures in drill cores (Figure 17C). This association might indicate that ferroan calcite precipitated simultaneously with oil emplacement. The deeper shales of the Egret Member and Fortune Bay Formation entered the oil window around 125 - 100 Ma (Magoon et al., 2005), promoting the migration of oil/bitumen through open fractures and faults during the early stages of burial in the Hibernia Formation (e.g., Sanei, 2020). Euhedral rhombs of saddle ferroan dolomite occur in siltstone of FA5, filling bioclasts with a planar-e texture (Sibley and Greg, 1987; Figure 21F) and postdating ferroan calcite cementation. Saddle dolomite often occurs in host rocks associated with hydrocarbons and is recognized as a late diagenetic cement

that may precipitate from high-saline brines under elevated temperatures (i.e., > 80 °C; Warren, 2000: Flügel, 2010; Rahimi et al., 2016;).

2.5.3 Oxygen isotopic composition: parental fluids

The $\delta^{18}O$ composition of carbonate cements serves as a proxy for the ^{18}O composition of their parental fluids since meteoric waters typically exhibit depleted $\delta^{18}O$ compared to marine water, and the oxygen isotope fractionation is temperature dependent (Hays and Grossman, 1991; Hoefs, 2006). In general terms, the investigated carbonate cements exhibit a lower $\delta^{18}O$ composition than the best-preserved Lower cretaceous carbonates (Figure 25; Veizer et al., 1999). Additionally, the $\delta^{18}O$ signatures progressively become more negative throughout the paragenetic sequence, from dolomite to calcite ultimately to ferroan calcite, reflecting an increase in precipitation temperatures. There is a notable variation in $\delta^{18}O$ among siderite cements, including relatively depleted $\delta^{18}O$ values ($\delta^{18}O_{siderite}$= -8.2 to -7.7 ‰ VPDB) observed in fluvial and tidal facies (FA2 and FA6), contrasting with higher values in marine offshore facies (FA5; $\delta^{18}O_{siderite}$= -3.1 to -3.2 ‰ VPDB), suggesting that substantial depletion of ^{18}O in siderite might be linked to the preferential microbial metabolism of ^{16}O in organic matter and the consequent production of ^{16}O-enriched bicarbonate (i.e., microbial oxygen fractionation; Duan et al., 1996; Morad et al., 1998). On the other hand, sphaerosiderite cements from fluvial-tidal facies (FA3, FA4) are relatively enriched in $\delta^{18}O$ compared to microcrystalline siderite cements. The $\delta^{18}O$ composition along with the typical spherical morphology and maltese cross-extinction pattern indicates that sphaerosiderite likely precipitated from brackish waters at near-surface conditions (e.g., Choi et al., 2003; Moore, 1992).

Dolomite and calcite cements show depleted oxygen isotopic compositions ($\delta^{18}O_{calcite}$ = -7.7 to -4.2 ‰ VPDB; $\delta^{18}O_{dolomite}$ = -4.1 to -1.6 ‰ VPDB) compared to the best preserved Lower

Cretaceous carbonates. However, dolomite exhibits a higher $\delta^{18}O$ trend than calcite. The narrow ranges of $\delta^{18}O$ values for both calcite and dolomite indicate that each cement precipitated from unique bulk fluid reservoirs. The $\delta^{18}O$ signature of diagenetic carbonates are influenced by the $\delta^{18}O$ of parental fluids and temperature of precipitation (Longstaff 1987; Morad et al 1990). Additionally, the common depletion in $\delta^{18}O$ of diagenetic carbonates are usually influenced by meteoric waters and elevated temperatures (Land, 1980; Machemer and Hutcheon, 1988; Scotchman, 1991; Longinelli et al., 2002). Hence, the original $\delta^{18}O$ values of these parental fluids can be estimated based on the $\delta^{18}O$ signature of carbonate cements and a set of assumptions about the values of $\delta^{18}O$ for Cretaceous marine and meteoric water, and the formative temperatures of cements (e.g., Saigal and Bjorlykke, 1987; Xiong et al., 2016; Luan et al., 2023). In addition, burial periods for the Lower Hibernia zone are suggested based on the burial curves illustrated in Figure 32, in order to link them with cementation events: early diagenesis (~135-130 Ma), early burial (130-120 Ma), late burial (120-70 Ma) and post-burial subsidence (70 Ma to present).

The $\delta^{18}O$ values ($\delta^{18}O$ ~ -2 ‰ VPBD; Veizer et al., 1999) of the best-preserved Early Cretaceous marine tropical carbonates formed under normal atmospheric conditions (25 - 30 °C) suggest seawaters with estimated $\delta^{18}O_{SW}$ composition of approximately -0.4 to 0.65 ‰ SOW (Friedman and O'neil, 1977). Furthermore, the present-day difference between meteoric water and seawater stands around -4‰ SMOW (Clark and Fritz, 1997). Assuming that this difference was consistent during the Lower Cretaceous period, the $\delta^{18}O$ value of the meteoric water would be – 4.4 to -3.3 ‰ SMOW (e.g., Yuan et al., 2017; Olanipekun and Azmy, 2022; Luan et al., 2023). An approximate depth of carbonate cementation was estimated employing the porosity-depth function $\emptyset = I * e^{\left(\frac{In(2)}{z_{\frac{1}{2}}} * Z\right)}$ (Ramm, 1992) and intergranular volumes. Assuming $z_{1/2}$ = 1 km and initial

porosity I = 42%, dolomite, calcite and ferroan calcite cementation might have occurred at approximately 144 m, 263 m (early diagenesis) and 580-930 m of depth (early burial), respectively. Consequently, the precipitation temperature of dolomite and calcite stands around 30-34 °C, and ferroan calcite at approximately 45-55 °C, assuming a geothermal gradient of 33 °C/km (Kolawole and Evenick, 2023; Figure 32). This aligns with the lack of two-phase fluid inclusions in carbonate cements, suggesting temperatures of precipitation below 50-60 °C (Goldstein, 2001). Based on the oxygen fractionation equation for calcite (10^3 In α =2.78*10^6 T^{-2} - 2.89; Friedman and O'Neil, 1977), dolomite (10^3 In α = 3.2*10^6 T^{-2} – 3.3; Land, 1983) and siderite (10^3 In α = 3.13*10^6 T^{-2} – 3.50; Carothers et al., 1988), the $\delta^{18}O$ of the parent fluids were calculated for temperatures between 25 - 35 °C (Tables 3-4; Figure 31). The estimated $\delta^{18}O$ of the parent fluids at 25 – 35 °C for calcite and dolomite are constrained between those of Early Cretaceous marine and meteoric water values evidencing mixing between marine and meteoric waters during calcite and dolomite cementation (Figure 31). Additionally, the carbon and oxygen composition of diagenetic calcites precipitated from mixed marine-meteoric waters exhibit a positive covariance as evidenced in calcite cements of the Lower Hibernia zone (Figure 25; Allan and Matthews, 1982; Moore 2001).

Ferroan calcite cements form an overlapping cluster of relatively depleted $\delta^{18}O$ composition ($\delta^{18}O_{ferroan\text{-}calcite}$= -10.2 to -9.1 ‰ VPDB), suggesting precipitation from a similar bulk fluid, but one distinct from other carbonate cements. These values overlap from both braided fluvial (FA2) and low-energy marine (FA5) facies associations, indicating that ferroan calcite precipitation occurred independently of early sedimentary environments, consistent with textural fabrics that suggest links to fracturing, faulting, and burial precipitation (Figure 25A). Furthermore, the $\delta^{18}O$ composition of ferroan calcite cements exhibits the most depleted values among calcite and dolomite suggesting higher temperatures and depths of precipitation during ferroan calcite

formation (e.g., Hays and Grossman, 1991; Chowdhury and Noble, 1996; Xiong et al., 2016). A plausible alternative interpretation for the depleted-^{18}O signature is the potential dissolution and subsequence reprecipitation likely in response to thermal and geochemical alterations during burial (Lynch and Land, 1996). Therefore, ferroan calcite might have precipitated at deeper settings during early burial, compared to the calcite and dolomite, which is consistent with the observed lower intergranular volumes of ferroan calcite cemented sandstone. Ferroan calcite cementation might be controlled by faults which acted as fluid pathways, based on its widely occurrence in the Lower Hibernia zone, overlapping isotopic signatures among ferroan calcite samples, and reduced intergranular volumes observed from ferroan calcite cemented intervals from a variety of facies associations (FA2, FA4, and FA5). Finally, ferroan calcite-cemented sandstones were not correlated to faults employing seismic data due to their relatively thinness (< 2 m), their dispersed occurrence in the stratigraphy and the limited resolution of the available seismic surveys at Hibernia (~ 35 m).

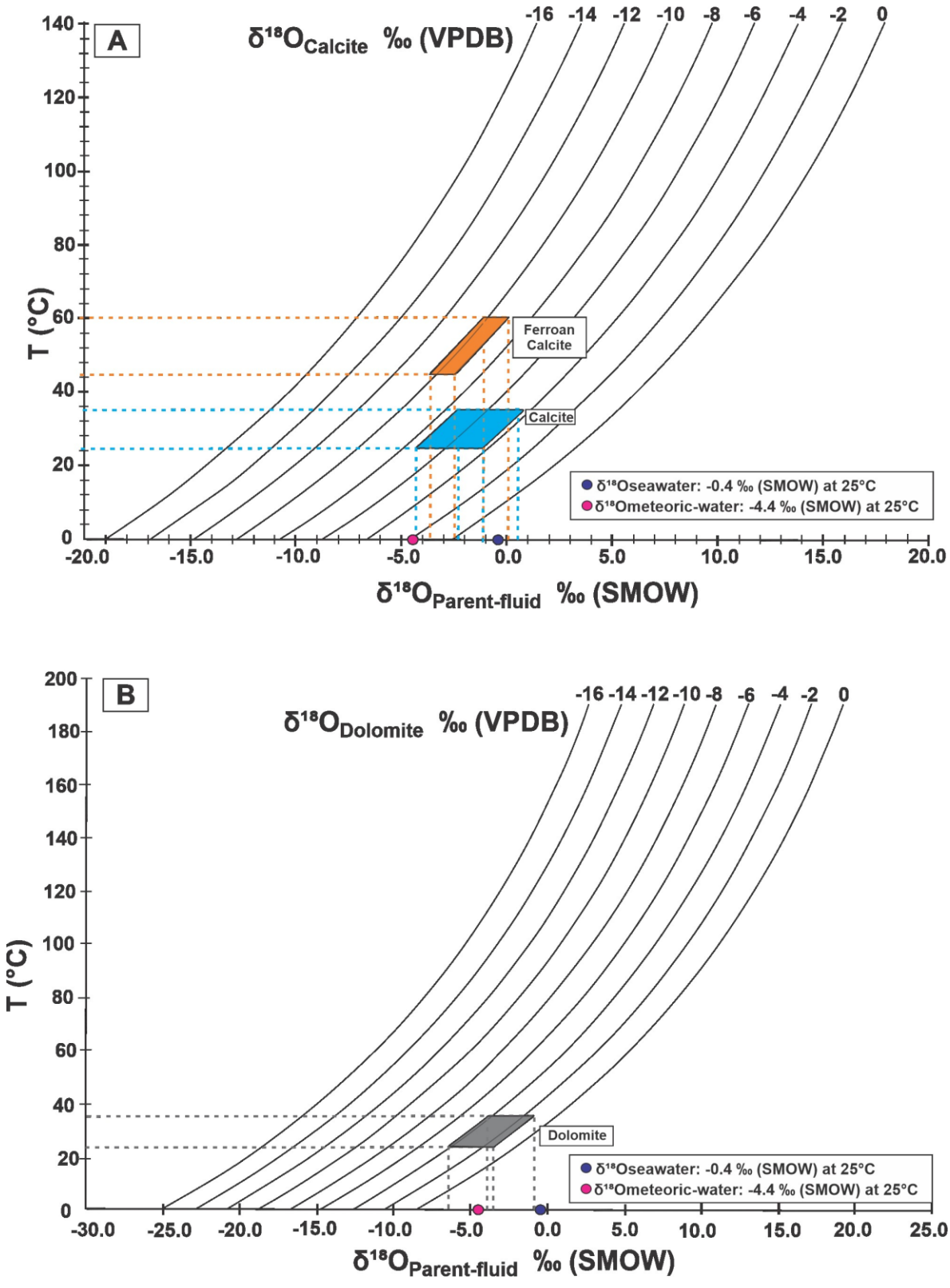

Figure 31. Temperature vs $\delta^{18}O$ diagenetic fluid for various A) $\delta^{18}O$ calcite and B) $\delta^{18}O$ dolomite values using the equation of $10^3 \ln \alpha = 2.78*10^6 T^{-2} - 2.89$ (Friedman and O'Neil, 1979) and $10^3 \ln \alpha = 3.2*10^6 T^{-2} - 3.3$ (Land, 1983), respectively.

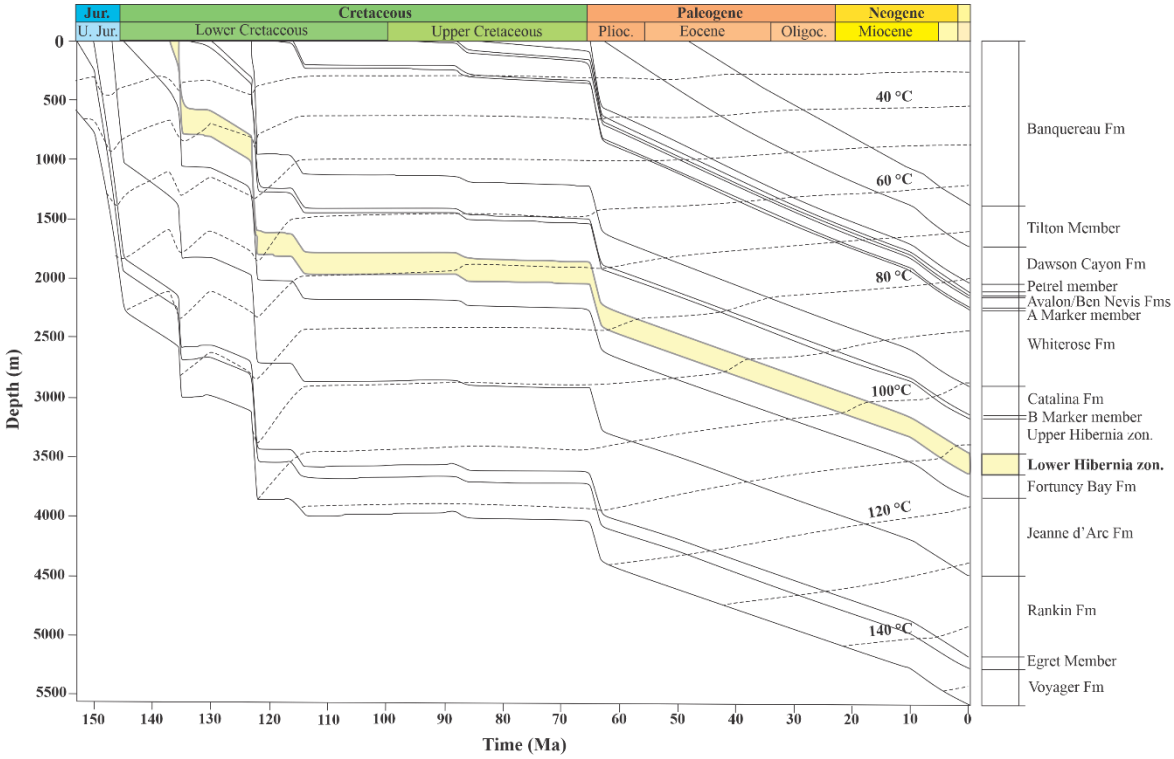

Figure 32. Burial history curves for the Hibernia B-08 well. Modified after DesRoches (1992)

2.5.4 Carbon isotopic composition: carbon source

Generally, carbonate cements with enriched $\delta^{13}C$ signatures typically reflect methanogenic processes occurring during diagenesis (e.g., $\delta^{13}C_{carbonates}$= 10 to 22 ‰ VPDB; Hayes and Boles, 1993; Choi et al., 2003; Purvis et al., 2020; Lanz et al., 2021). The depleted ^{13}C signature of carbonate cements in the Lower Hibernia zone precludes the possibility that the carbon source was mainly methanogenic due to the lower $\delta^{13}C$ values (-23.9 to 1.2 ‰ VPDB). The $\delta^{13}C$ values of dolomite cements in the offshore marine facies (FA5) are slightly lower ($\delta^{13}C_{dolomites}$= -3.4 to 0.6 ‰ VPDB) than those documented for the best-preserved Lower Cretaceous marine carbonates (Figure 25; Veizer et al., 1999), likely reflecting a carbon source linked the to oxidation of organic matter of and/or bioclast dissolution (Irwin et al., 1977). Furthermore, the dolomite and ferroan

dolomite cement of delta front facies (FA1) shows a more depleted ^{13}C signature ($\delta^{13}C_{dolomite}$= -11.8 ‰ VPDB; $\delta^{13}C_{ferroan\text{-}dolomite}$= -6.2 ‰ VPDB) compared to dolomite in offshore marine facies (FA5), indicating carbon contributions from bacterial sulphate reduction (Irwin et al., 1977; Morad 1998).

Calcite cements exhibit a broader and more depleted ^{13}C-trend compared to dolomite ($\delta^{13}C_{calcite}$= -23.9 to -2.5 ‰ VPDB), reflecting carbon contributions from different sources including bioclast dissolution, microbial sulphate reduction, and decomposition of organic matter. Calcite cements of the fluvial tidal facies (FA3) have the most depleted ^{13}C signature among carbonate cements ($\delta^{13}C_{calcite}$= -23.9 to -14.6 ‰ VPDB; Figure 25B) along with the coexistence with pyrite and low iron concentration, is interpreted to reflect carbon contributions from microbial sulphate reduction during early diagenesis (e.g., Irwin et al., 1977; Coleman and Raiswell, 1981; Kantorowicz et al., 1987; Morad, 1998). Conversely, calcite cements in marine offshore and tidal bar facies (FA5 and FA6) exhibit a more enriched $\delta^{13}C$ trend, most likely due to carbon contributions from dissolution of bioclasts and/or oxidation of organic matter (Figure 25; e.g., Bjørkum and Walderhaug, 1990; Chowdhury and Noble, 1996; Mcbride et al., 2003; Xiong et al., 2016; Mao et al., 2019). This is consistent with the calcite-cemented beds found near bioclast-rich layers in FA5 and FA6.

Siderite occurs as microcrystalline rims around detrital grains and rarely in the nuclei of pyrite (Figure 23F). The $\delta^{13}C$ composition is similar to that of calcite and dolomite cements ($\delta^{13}C_{siderite}$= -5.2 to -1.6 ‰ VPDB). The $\delta^{13}C$ signature and the microcrystalline siderite rims indicates that the carbon sources are most likely related to the oxidation of organic matter in the iron reduction zone (Morad, 1998). Conversely, the depleted $\delta^{13}C$ composition of sphaerosiderite cements coupled with its coexistence with pyrite, is typical of carbon from oxidation of organic matter as iron and sulphate were reduced at shallow depths (Irwin et al., 1977; Coleman et al., 1997).

In burial settings, carbon dioxide production is mainly driven by the decarboxylation of organic matter as bacterial activity diminishes due to the increased temperature (Irwin, 1977; Morad, 1998). The $\delta^{13}C$ signature of the investigated ferroan calcite ($\delta^{13}C_{ferroan\text{-}calcite}$= -13.1 to -4.9 ‰ VPDB; Figure 25A) coupled with the depleted $\delta^{18}O$ composition ($\delta^{18}O_{ferroan\text{-}calcite}$= -10.2 to -9.1 ‰ VPDB) and low intergranular volumes of ferroan calcite-cemented sandstones, implies that the main carbon source might have been associated with dissolved inorganic carbon derived from deeper shales under the influence of thermal decarboxylation processes during the Cretaceous drift stage of the Jeanne d'Arc Basin (e.g., Egret member, Fortune Bay Formation; Magoon et al., 2005).

2.5.5 Trace element geochemistry of carbonate cements

The investigated dolomite cements exhibit a comparable Sr content (333 ± 5 ppm) to dolomite formed from diagenetic fluids (mean ~300 ppm; Budd, 1997). This similarity is notable, particularly considering that calcite and dolomite in ancient limestones typically possess substantially lower Sr concentrations (20 – 70 ppm; Banner, 1995). The Y/Ho ratio (mean 29.6 ± 2.4; n= 11) is lower than the ratio reported for the modern seawater (Y/Ho_{sw} = 44-74; Bau and Dulski, 1996), which indicates an influence of non-marine parent fluids. In this context, dolomite cements likely precipitated from mixed pore fluids rather than pristine marine water. Furthermore, the relatively high Fe contents (6932 ± 3363 ppm) and Mn contents (1779 ± 96 ppm) indicate that the dolomitizing pore fluids were mainly reducing during dolomite precipitation (Fe > 1000 ppm and Mn > 50 ppm; Budd, 1997).

Calcite is the most iron-depleted cement among the carbonate cements described in the Lower Hibernia zone (661 ± 1551 ppm; Table 5). The higher Mn concentrations (2689 ± 543 ppm) compared to the Fe content suggest that calcite precipitated in a less reducing environment rather

than an oxidizing setting (; e.g., Frank et al., 1982; Xiong et al., 2016). The low Mg concentrations in calcite cements (mean 17462 ± 1330 ppm) are typically attributed to meteoric cementation (mean < 40000 ppm; Flugel, 2010) since meteoric waters have lower Mg/Ca ratio compared to marine water. Magnesium is leached during diagenesis, and High-Mg calcite is converted into Low-Mg calcite (Flügel, 2010; Hashim and Kaczmarek, 2021). The lack of negative Cerium anomalies (Ce/Ce^*_{SN}), in calcite cements are often attributed to shallow groundwater processes respectively (Nothdurft et al., 2004; Webb et al., 2009; Xiong et al., 2016; Rieger et al., 2022). Negative $(Ce/Ce^*)_{SN}$ anomalies typically occur in shallow water environments due to the oxidation of soluble Ce^{3+} to insoluble Ce^{4+} through bacterial degradation (Elderfield and Greaves, 1982; German and Elderfield, 1990). On the other hand, a positive and/or a lack of Ce anomalies in carbonates ($Ce/Ce^*_{SN} \geq 1$) indicates the predominance of diagenetic pore waters rather than pristine marine water during carbonate cements precipitation (German and Elderfield, 1990). Furthermore, the Y/Ho ratio of calcite cements (mean 32 ± 6.9; n=17) is lower than the ratio observed in present-day sea water (Y/Ho_{SW} = 44-74; Bau and Dulski, 1994) also suggesting potential influence from non-marine parent fluids (e.g., Nothdurft et al. 2004). Consequently, calcite cements are interpreted to have been precipitated in a suboxic phreatic environment from mixed marine-meteoric pore fluids also consistent with the discussed oxygen and carbon composition.

Mn and Fe contents of diagenetic carbonates reflect the redox conditions during carbonate precipitation because Mn- and Fe-oxides/oxyhydroxides remain stable under oxidizing conditions, preventing the availability of Mn^{2+} and Fe^{2+} ions during carbonate formation (e.g., Xiong et al., 2016; Frank et al., 1982; Barnaby and Rimstidt, 1989a). Iron in the oxidized state (Fe^{3+}) cannot replace calcium in calcite due to differences in charge and size between Fe^{3+} and Ca^{2+}. Instead, reduced iron (Fe^{2+}) can be readily incorporated into the carbonate structure (James and Alden,

1982). Consequently, carbonates formed under oxidizing conditions, such as those directly precipitated from seawater at near-surface conditions, exhibit low Mn and Fe contents (Fouke, 1994; Budd, 1997; Morad, 1998). In contrast, microcrystalline ferroan dolomite cements deviate from this pattern due to their elevated Fe and Mn concentrations (49145 ± 8360 ppm; 2277 ± 366 ppm), indicating reducing conditions during cementation. Additionally, the REE_{SN} pattern of ferroan dolomite closely resembles the REE_{SN} pattern of dolomite cements, suggesting that ferroan dolomite partially inherited the REE components of dolomite cements (Figure 27). This might indicate the evolution of the REE compositions of the dolomitizing fluid with progressive burial and change of redox conditions.

Ferroan calcite, saddle ferroan dolomite and siderite exhibit high Fe and Mn contents, with a lack of negative cerium anomalies evidencing reducing conditions during carbonate precipitation (e.g., Frank et al., 1982; Barnaby and Rimstidt, 1989). Their REE_{SN} patterns exhibit a similar profile to the REE_{SN} pattern of river water, showing an enrichment in the ∑REE content, especially in MREE. Additionally, the REE_{SN} pattern of ferroan calcite and saddle ferroan dolomite exhibit almost similar profiles. Combining the petrographic observations, stable isotopes, and similar REE_{SN} profiles, ferroan calcite and saddle ferroan dolomite might have formed from a similar late diagenetic fluid in a burial setting (e.g., Xiong et al., 2016).

2.5.6 Controls on early carbonate cementation: depositional settings, relative sea level variations, and sequence stratigraphy

The diagenetic sequence proposed in this study reflects the changes in environments of sedimentation and corresponding relative sea-level fluctuations and near-surface pore water

evolution. Linking sedimentary sequence architecture to early cement formation models may help to predict how carbonate cements are distributed in the reservoir stratigraphy (e.g., Gibbons et al., 1993; Bakke, 1996; Zamanzadeh et al., 2009). The Lower Hibernia zone records the evolution of a deltaic to estuarine succession under a fluctuating relative sea level. The progradation recorded by the delta front facies of layer 4 (FA1) represents the highstand system set of a deltaic succession (Sequence 1), initially recorded by the Fortune Bay Formation. The erosive boundary at the base of the braided fluvial deposits (FA2) of Layer 3 is interpreted as a Sequence Boundary (SB), which marks the lowest point of accommodation space and a new stratigraphy sequence (Sequence 2). The erosive nature of this contact represents a forced regression indicating relatively rapid loss of accommodation and sea level regression (Figure 29; Posamentier and Allen, 1999; Catuneanu, 2006; Catuneanu et al., 2011). Thin layers of dolomite-cemented sandstones of layer 4 (< 1 meter thick, FA1) exhibit pore-filling blocky dolomite mosaics and planar-s fabrics along with the high intergranular volumes (~35%), indicating slow rates of dolomite growth at low temperatures, most likely during early diagenesis (e.g., Sibley and Greg, 1987; Rahimi et al., 2016). A decrease in sulphate concentrations due to the microbial reduction into sulphide (e.g., pyrite) coupled by an increase in pore water alkalinity enhances dolomite precipitation (Baker and Kastner, 1981). This is consistent with the depleted $\delta^{13}C$ signature of dolomite cements of FA1 and their coexistence with pyrite. In addition, the overall absence of evaporite minerals in the Lower Hibernia zone, evidences normal marine conditions during sedimentation rather than sabkha conditions (Badiozamani et al., 1978; Land 1983). Dolomite precipitation at shallow depths, when evaporites are absent, may be attributed to pore water mixing of different compositions (Badiozamani, 1973; Ward and Halley, 1985; Hardie, 1987; Taberner and Santisteban, 1987; Bjørlykke, 1994). The $\delta^{18}O$ composition, Sr content, REE signature and fluvio-marine nature of the Lower Hibernia zone suggest an influence of marine and meteoric waters in the dolomitizing pore fluid. Although the

mixing between seawater and meteoric water does not explain a regional scale dolomitization, it may explain a relatively limited amount of dolomite cements in sandstones deposited coastal environments with cyclical changes of salinity (Varol and Magaritz, 1992; Moore, 2001; Taylor and Gawthorpe, 2003, Mache, 2004; Choquette and Hiatt, 2008). Additionally, a higher $\delta^{18}O$ signature is expected for dolomites precipitating directly hypersaline/mesohaline waters, and regions affected by seepage-reflux dolomitization typically show high dolomitized rock volumes (e.g., Melin and Scholle, 2002; Győri, et al., 2019; Adam et al., 2019). This contrasts with the low abundance of dolomite cements observed in the Lower Hibernia zone. Sea-level falls facilitated the retention of seawater and/or marine-meteoric waters within sediments, and coupled with fluid expulsion by compaction of the underlying succession of shallow-marine shales (Fortune Bay Formation; Figure 28 and Figure 29), delivered fluids rich in Mg^{2+}, Ca^{2+} and CO_3^{2-} promoting dolomite supersaturation and subsequent dolomite cementation (e.g., Kaldi and Gidman, 1982; Varol and Magaritz, 1992; Mather 2020; Olanipekum and Azmy, 2022).

Braided fluvial (FA2) strata above the sequence boundary represent deposits of the Lowstand System Tract (LST), record aggradation and progradation following the lowest level of accommodation in the sequence. The overlying tidal-fluvial facies (FA3) began to accumulate after the onset of a relative sea-level rise (Figure 29). The Transgressive System Tract (TST) includes these facies and overlying tidal strata (FA4) and the Medial shale (FA5-FA4). During this transgression, the estuary mouth migrated up valley, with a coinciding reduction of the delivery of coarse clastic sediment during Medial Shale deposition. As sea levels rose during transgression, major inland incursions of seawater combined with alkaline conditions led to mixed marine-meteoric pore waters becoming supersaturated with calcite (Badiozamani et al., 1973). This facilitated calcite formation and explains the presence of calcite-cemented stratabound layers in

tidal-fluvial facies, which exhibit poikilotopic fabrics and high intergranular volumes. Subsequent progradation and normal regression of tidal flats overlying FA5 represent the Highstand System Tract (HST) and the end of the Sequence 2. Consequently, early diagenetic fluids progressively evolved from calcite-saturated mixed waters to pore waters supersaturated with respect to dolomite, allowing dolomite precipitation towards the top of Facies Association 5, below the maximum flooding surface (e.g., Moore 1992; Gibbons et al., 1992).

The base of sequence 3 is characterized by an erosive surface recording fluvial erosion due to relatively rapid loss of accommodation and sea level regression. The overlying Transgressive System Tract comprises tidal fluvial and tidal facies (FA3-FA4), with the maximum flooding surface between the TST and the HST along the transition of Layers 2 and 1. The tidal bar formation occurred at the prograding estuary mouth as sediment supply overwhelmed the accommodation space. Facies associations 6 overlying the Transgressive System Tract (Layer 2: FA3-FA4) comprises the Highstand System Tract of the Sequence 3, recording the end of the Lower Hibernia zone deposition. The abundance of early calcite-cemented layers in FA6 strata is attributed to supersaturation with respect to calcite in the pore fluids due to the contributions of marine and meteoric water during FA6 deposition. The frequent alternation of straight-crested dunes and bioclast-rich muddy siltstones indicates a dynamic environment with local sea-level variations with low and high sedimentation rates (Olariu et al., 2012), allowing constant seawater contributions into the sediments and interaction with meteoric pore water during slack-water periods.

Carbonate cementation in the Lower Hibernia zone illustrates how sea level fluctuations contribute to the formation of carbonate-cemented layers in shallow-marine siliciclastic systems (e.g., Moore 1992). Specifically, dolomite cements tend to form during forced regressions (e.g., FA1 and FA5), while calcite-cemented stratabound layers develop during transgressions impacting Transgressive

System Tract strata (e.g., FA3 – FA4). Although early carbonate-cemented sandstones are rare in Layer 3 Lower (L3L) and Layer 2 (L2), evidence of carbonate dissolution is widespread at various intervals of the Lower Hibernia zone (Figure 33). The preservation of high intergranular porosity and evidence of cement dissolution suggest early carbonate cementation in L3L and L2, likely calcite, and subsequent carbonate dissolution developing secondary porosity.

2.5.7 Mesogenetic carbonate dissolution and implications for porosity evolution

The fluid-rock interactions in the Lower Hibernia zone played an essential role in the evolution of reservoir porosity as they involved multiple carbonate cementation and dissolution events. Early episodes of carbonate cementation likely preserved considerable porosity and permeability prior to significant mechanical compaction. Oversized and elongated pore throats, preservation of high intergranular porosity and remnants of intergranular calcite constitute the primary evidence of an early carbonate dissolution observed in the Lower Hibernia zone (Figure 33; e.g., Schmidt and McDonald, 1979; Surdam et al., 1984; Andresen et al., 1994; Morad, 1998). Previous studies on the Hibernia Formation and Cretaceous reservoirs in the Jeanne d'Arc basin have also reported the dissolution of early carbonate cements (Brown et al., 1989; Hesse and Abid, 1998; Olanipekum and Azmy, 2022; Luan et al., 2023). Recent discussions elucidate two possible mechanisms for extensive carbonate dissolution in sandstones: (1) the massive influx of cold meteoric freshwater during early diagenesis and (2) the influx of deep basinal fluids provided via faults and fractures (Yuan et al. 2019). Additionally, the organic CO_2 generated by the thermal maturation of kerogen also promotes carbonate dissolution on a small scale (e.g., Weedman et al., 1996; Lu et al., 2011). During the early burial stage of the Hibernia Formation (130-120 Ma) and before ferroan calcite cementation, freshwater and basinal fluids may have percolated potentially through pre-existing

fluid pathways such as the NE-SW-trending fault system. In addition, this period slightly aligns with the onset of kerogen degradation and carbon dioxide production in deeper burial shales , such as the Egret member, which also experienced over-pressuring due to high sedimentation rates in the JDB at approximately 140-130 Ma (Williamson et al., 1993). Consequently, carbonate dissolution presumably occurred as acidic pore waters reduced the alkalinity of the carbonate-water system during early burial at depths shallower than 1 km (e.g., Huang et al., 2009). This process resulted in the formation of secondary pores, which were crucial for ferroan calcite cementation and hydrocarbon emplacement. Additionally, acidic pore waters, characterized by elevated carbonate dissolution rates, are likely capable of precipitating silica at low rates (Bjorlykke, 1994). This diagenetic process might explain the notable absence of quartz overgrowths in intervals cemented by calcite and dolomite (Figure 20), as well as in intervals cemented by silica exhibiting carbonate dissolution textures (Figure 31). The exceptional levels porosity (up to 22%; Brown et al., 1989) observed in the Hibernia Formation are linked to the preservation of intergranular volume through the formation of early carbonate cements, followed by subsequent dissolution during burial.

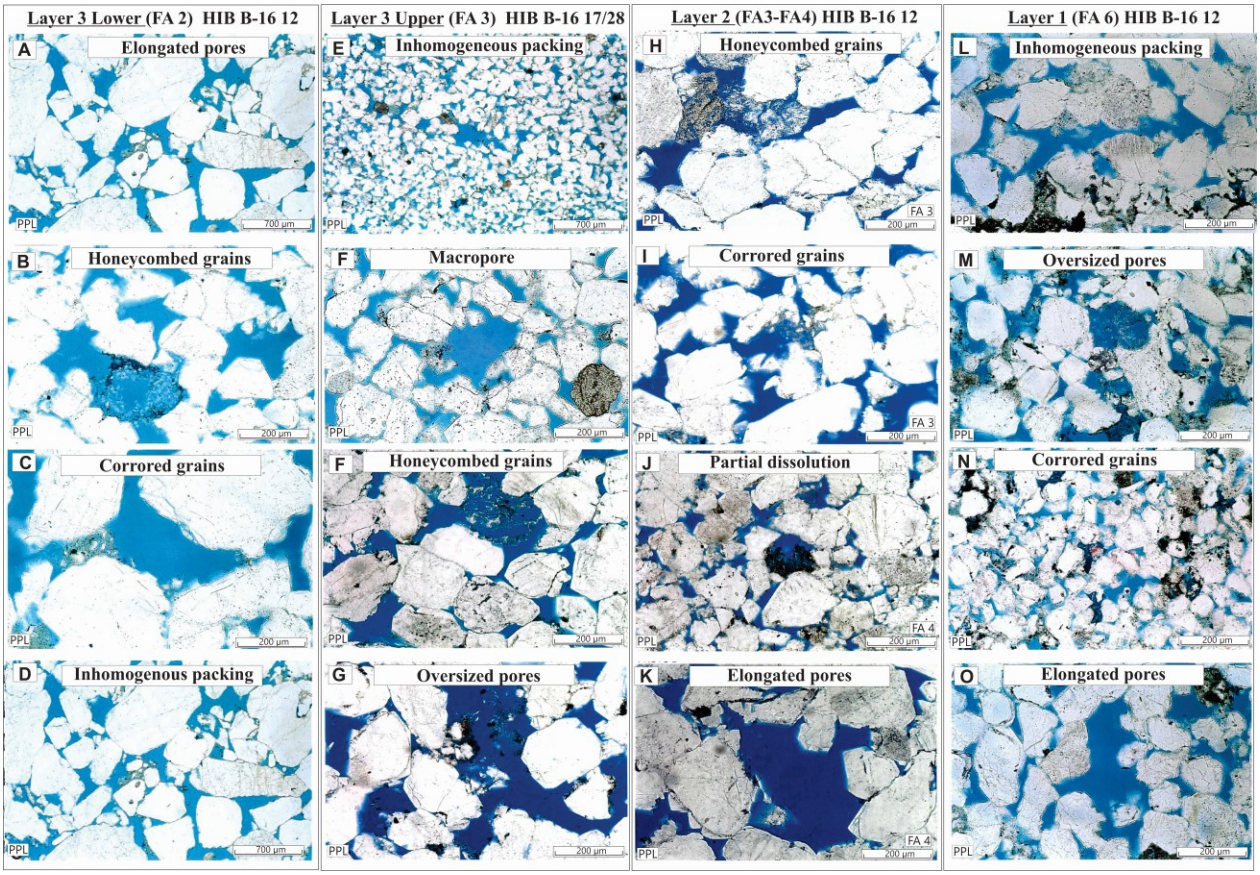

Figure 33. Evidence of cement dissolution in the Lowe Hibernia zone. A-D) Layer 3 Lower; E-G) Layer 3 Upper; H-K) Layer 2 and L-O) Layer 1. Microphotographs are available in reservoir quality and petrography reports of the Hibernia B-16 12, B-16 17, and B-16 28 wellbores. Modified after Core Lab (1998, 2002); Wang et al. (2005).

2.8 Conclusions

The Lower Hibernia zone records the transition from a deltaic to an estuarine environment punctuated by two regressive sequence boundaries and characterized by six facies associations: delta front (FA1), braided fluvial (FA2), marginal marine tidal-fluvial channels (FA3), tidal flats (FA4), marine offshore (FA5) and tidal bars (FA6). Deltaic progradation was recorded by the delta front strata in Layer 4, overlayed by the stacked braided fluvial strata (FA2) of Layer 3 Lower (L3L). The erosive surface separating FA1 from FA2 is interpreted as a sequence boundary and suggests an erosion of the delta front coinciding with a forced regression before the onset of fluvial sedimentation. Fining-upward successions of marginal marine channels (FA3) and tidal flats (FA4) in Layer 3 Upper (L3U) overlie the braided fluvial strata and represent the fluvial tidal transition of the estuarine system. The onset of tidal-fluvial sedimentation (FA3-FA4) followed by the offshore marine deposition of FA5 in the Medial shale (MS) was given by increased rates of subsidence that resulted in a progressive transgression and retrogradation of the fluvial-deltaic system. An abrupt sea-level fall was recorded by a second regressive sequence boundary that separates the Medial Shale from Layer 2 (L2), followed by the fluvial-tidal deposition of fining-upward successions of marginal marine channels (FA3) and tidal flats (FA4). The final episode of sedimentation is defined by a sea-level rise recorded by the coarsening-upward successions of subtidal sand bars (FA6) in Layer 1 (L1).

Most of the reservoir units in the Lower Hibernia zone consist of well-sorted, fine to coarse-grained quartzose sandstone with variable volumes of carbonate cements. Petrographic analyses revealed three main pervasive carbonate cements: early calcite, early dolomite, and late ferroan calcite which usually form stratabound layers. Ferroan calcite stands as the most common pore-filling cement, followed by calcite and dolomite. Grain-rimming micrite, ferroan dolomite, and

siderite partially fill intergranular space, representing minor carbonate cements and exhibiting lower abundance relative to calcite and dolomite.

Calcite-cemented sandstone exhibit poikilotopic texture and retain relatively high intergranular volumes (33 % IGV), indicating pre-burial cementation. The high Mn and Fe contents (2689 ± 543 ppm 662 ± 1552 ppm, respectively) indicate precipitation in a less reducing environment rather than oxidizing setting. The $\delta^{18}O$ composition ($\delta^{18}O_{calcite}$ = -7.7 to -4.2 ‰ VPDB) suggests a parent fluid of mixed marine and meteoric waters with carbon derived from organic matter oxidation and bacterial sulfate reduction, as indicated by its $\delta^{13}C$ composition ($\delta^{13}C_{calcite}$ = -23.9 to -2.5 ‰ VPDB).

Dolomite cements show a relatively high intergranular volume (35% IGV), indicating pre-burial dolomite cementation, and exhibiting a planar-s fabric, characteristic of slow crystal growth at low temperatures. The Sr content and Y/Ho ratio of dolomite coupled with the slightly high Fe and Mn contents indicate an influence of reduced non-marine parent fluids during dolomite cementation. This is also supported by its $\delta^{18}O$ composition ($\delta^{18}O_{dolomite}$ = -4.1 to -1.6 ‰ VPDB), which reflects a parent fluid of mixed marine and meteoric waters.

The widespread occurrence of ferroan calcite across multiple facies associations (FA2, FA3, FA5, FA6) within the Lower Hibernia zone suggests a lack of stratigraphical control on ferroan calcite distribution. The reduced intergranular volume of ferroan calcite-cemented sandstones (22 – 28 % IGV) compared to those cemented by calcite and dolomite suggests that ferroan calcite precipitated during progressive burial, postdating early carbonate dissolution, and likely at higher temperatures and as inferred from its depleted oxygen composition ($\delta^{18}O_{ferroan\text{-}calcite}$ = -10.2 to -9.1 ‰ VPDB). The coeval occurrence of ferroan calcite with bitumen aggregates might suggest that precipitation occurred in relatively timing the oil window. Additionally, the elevated Fe and Mn

concentrations and lack of negative Ce anomalies of the ferroan calcite and saddle ferroan dolomite highlight their formation under reducing conditions. The similarity in REE_{SN} profiles of ferroan calcite and saddle ferroan dolomite coupled with the petrographic observations, indicates a common origin from late diagenetic fluids in a burial setting.

The stratigraphy and sea-level fluctuations influenced the pore water evolution and early diagenetic pervasive carbonate cementation in the Lower Hibernia zone. Dolomite cement fills intergranular spaces in the delta front and offshore marine facies associations (FA1 and FA5) underlying the two sequence boundaries of the Lower Hibernia zone. Regression episodes facilitated the retention of seawater within sediments, along with the dewatering of underlying shale units, representing the primary Mg^{2+} sources that promoted dolomite saturation in the pore fluids. Calcite cements were observed in marginal marine tidal-fluvial channels, marine offshore, and subtidal flats facies (FA3, FA5, and FA6). Calcite cementation occurred during transgressions by the inland incursion of seawater that promoted the saturation with respect to calcite in the marine-meteoric mixed parent fluids.

Carbonate dissolution is suggested to have occurred in the first stages of burial, predating the ferroan calcite formation, when acidic pore waters percolated through the preexisting NE-SW-trending fault system into the Lower Hibernia zone dissolving early carbonate cements based as evidenced by relatively common dissolution textures. This carbonate dissolution most likely led to secondary porosity development, enhancing the porosity and permeability of the reservoir units.

2.9 References

Adams, A., Larryn, W., Lukas, A. (2019). Dolomitization by hypersaline reflux into dense groundwaters as revealed by vertical trends in strontium and oxygen isotopes: Upper Muschelkalk, Switzerland. Sedimentology, 66, 362-390.

Albrechtsons, E., and Sinclair, L. K. (1997). Representative Core Samples from the Hibernia and Avalon Reservoirs, Hibernia Field, Offshore Newfoundland, Canada.

Allan, J. R., Matthews, R. K. (1982). Isotopic signatures associated with early meteoric diagenesis: Sedimentology, 29, 797-817.

Andresen, B., Throndsen, T., Barth, T., and Bolstad, J. (1994). Thermal generation of carbon dioxide and organic acids from different source rocks. Organic Geochemistry, 21(12), 1229–1242.

Arthur, K. R., Cole, D. R., Henderson, G. G. L., and Kushnir, D. W. (1982). Geology of the Hibernia Discovery.

Badiozamani, K. (1973). The Dorag Dolomitization Model-Application to The Middle Ordovician of Wisconsin. Journal Of Sedimentary Petrology, 43(4), 965–984.

Bakke, N. E. (1996). Prediction of calcite cement distribution in shallow marine sandstones reservoirs using seismic data. PhD thesis. Department of Petroleum Engineering and Applied Geophysics – Norwegian University of Science and Technology.

Baker, P. A., and Kastner, M. (1981). Constraints on the formation of sedimentary dolomite. Science, 213.

Banner, J. (1995). Application of the trace element and isotope geochemistry of strontium to studies of carbonate diagenesis. Sedimentology, 42(5), 805–824.

Barnaby, R. J., and Rimstidt, J. D. (1989a). Redox conditions of calcite cementation interpreted from Mn and Fe contents of authigenic calcites. GSA Bulletin, 101(6), 795–804.

Barnaby, R. J., and Rimstidt, J. Donald. (1989b). Redox conditions of calcite cementation interpreted from Mn and Fe contents of authigenic calcites. GSA Bulletin, 101(6), 795–804.

Bau, M., and Dulski, P. (1996). Distribution of yttrium and rare-earth elements in the Penge and Kuruman iron-formations, Transvaal Supergroup, South Africa. Precambrian Research, 79(1), 37–55.

Baur, F., Wielens, H., and Littke, R. (2009). Basin and Petroleum Systems Modeling at the Jeanne d'Arc and Carson Basin offshore Newfoundland, Canada.

Beard, D. C., and Weyl, P. K. (1973). Influence of Texture on Porosity and Permeability of Unconsolidated Sand. AAPG Bulletin, 57(2), 349–369.

Bhattacharya. (2006). Deltas. In R. G. Walker and H. Posamentier (Eds.), Facies Models (84th ed.). SEPM Special Publication.

Bjørkum, P. A., and Walderhaug, O. (1990). Geometrical arrangement of calcite cementation within shallow marine sandstones. Earth-Science Reviews, 29(1), 145–161.

Bjørlykke, K. (1994). Fluid-flow processes and diagenesis in sedimentary basins. Geological Society, London, Special Publications, 78(1), 127–140.

Bolhar, R., and Vankarnendonk, M. (2007). A non-marine depositional setting for the northern Fortescue Group, Pilbara Craton, inferred from trace element geochemistry of stromatolitic carbonates. Precambrian Research, 155(3–4), 229–250.

Bridge, J., and Lunt, I. (2009). Depositional Models of Braided Rivers (pp. 11–50).

Brown, D. M., Mcalpine, K. D., and Yole, R. W. (1989). Sedimentology and Sandstone Diagenesis of Hibernia Formation in Hibernia Oil Field, Grand Banks of Newfoundland^ modeling constrains the interpreted time and depth of hydrocarbon generation and accumulation in the sand-stone reservoirs.

Budd, D. A. (1997). Cenozoic dolomites of carbonate islands: their attributes and origin. Earth-Science Reviews, 42(1), 1–47.

Carothers, W. W., Adami, L. H., and Rosenbauer, R. J. (1988). Experimental oxygen isotope fractionation between siderite-water and phosphoric acid liberated CO2-siderite (Vol. 52).

Catuneanu, O., Galloway, W. E., Kendall, C., Miall, A. D., Posamentier, H. W., Strasser A. (2011). Sequence stratigraphy: methodology and nomenclature. Newsletters on Stratigraphy, 44 (3), 173-245.

Catuneanu, O. (2006). Principles of Sequence Stratigraphy (1st ed.). Elservier.

Chafetz, H. S., Wilkinson, B. H., and Love, K. M. (1985). Morphology and Composition of Non-Marine Carbonate Cements in Near-Surface Settings. In N. Schneiderman and P. M. Harris (Eds.), SEPM Special Publication: Carbonate Cements. SEPM.

Choi, K. S., Khim, B. K., and Woo, K. S. (2003). Spherulitic siderites in the Holocene coastal deposits of Korea (eastern Yellow Sea): elemental and isotopic composition and depositional environment. Marine Geology, 202(1), 17–31.

Choquette, P., Hiatt, E. (2008). Shallow-burial dolomite cement: a major component of many ancient sucrosic dolomites. Sedimentology, 55, 423-460.

Chowdhury, A. H., and Noble, J. P. A. (1996). Origin, distribution, and significance of carbonate cements in the Albert Formation reservoir sandstones, New Brunswick, Canada. Marine and Petroleum Geology, 13(7), 837–846.

Clark, I. D., and Fritz, P. (1997). Environmental Isotopes in Hydrogeology (1st ed.). CRC Press.

CNLOPB. (1997). Properties of Oil-Bearing Reservoirs.

CNLOPB. (2021). Hibernia field: Hibernia Well locations, Hibernia reservoir - L3b sandstone.

CNLOPB. (2022). Petroleum Resources and Reserves Newfoundland Area. Canada Newfoundland and Labrador Offshore Petroleum Board - Report.

Coleman, J. M., and Prior, D. B. (1980). Deltaic Sand Body Variability, a 1980 Short Course. In Deltaic Sand Bodies. American Association of Petroleum Geologist.

Coleman, M. L., and Raiswell, R. (1981). Carbon, oxygen and sulphur isotope variations in concretions from the Upper Lias of N.E. England. Geochimica et Cosmochimica Acta, 45, 329–340.

Coleman, M. L., Raiswell, R., Brown, A., Curtis, C. D., Aplin, A. C., Ortoleva, P. J., Gruszczynski, M., Lyons, T. W., Lovley, D. R., Eglinton, G., Raiswell, R., Coleman, M. L., Curtis, C. D., and Turner, G. (1997). Microbial mineralization of organic matter: mechanisms of self-organization and

inferred rates of precipitation of diagenetic minerals. Philosophical Transactions of the Royal Society of London. Series A: Physical and Engineering Sciences, 344(1670), 69–87.

Core Lab. (1998). A Petrographic Study of the Hibernia Formation at HMDC Hibernia B 16-2.

Core Lab. (2002). A Petrographic and Reservoir Quality Study of the Hibernia Formation at HMDC Hibernia B 16-28.

Dalrymple, R., Mackay, D., Ichasso, A., and Choi, K. (2012). Processes, Morphodynamics and Facies of Tide-Dominated Estuaries. In R. A. Davis and R. W. Dalrymple (Eds.), Principles of Tidal Sedimentology. Springer.

Dalrymple, R. W. (2010). Tidal Depositional Environments. In N. P. James and R. W. Dalrymple (Eds.), Facies Models 4. Geological Association of Canada.

Dalrymple, R. W., and Choi, K. (2007). Morphologic and facies trends through the fluvial–marine transition in tide-dominated depositional systems: A schematic framework for environmental and sequence-stratigraphic interpretation. Earth-Science Reviews, 81(3), 135–174.

Dalrymple, R. W., Knight, R. J., Zaitlin, B. A., and Middleton, G. V. (1990). Dynamics and facies model of a macrotidal sand-bar complex, Cobequid Bay—Salmon River Estuary (Bay of Fundy). Sedimentology, 37(4), 577–612.

Dalrymple, R. W., and Rhodes, R. N. (1995). Chapter 13 Estuarine Dunes and Bars. In G. M. E. Perillo (Ed.), Developments in Sedimentology (Vol. 53, pp. 359–422). Elsevier.

Dalrymple, R. W., Zaitlin, B. A., and Boyd, R. (1992). Estuarine facies models; conceptual basis and stratigraphic implications. Journal of Sedimentary Research, 62(6), 1130–1146.

Davies, C., Poynter, S., Macdonald, D., Flecker, R., Voronova, L., Galverson, V., Kovtunovich, P., Fot'yanova, L., and Blanc, E. (2005). Facies Analysis of the Neogene Delta of the Amur River, Sakhalin, Russian Far East: Controls on Sand Distribution. In L. Giosan and J. P. Bhattacharya (Eds.), River Deltas - Concepts, Models and Examples (pp. 207–229). SEPM Society of Sedimentary Geology.

Desjardins, P. R., Buatois, L. A., and Mángano, M. G. (2012). Tidal Flats and Subtidal Sand Bodies. In D. Knaust and R. G. Bromley (Eds.), Developments in Sedimentology (Vol. 64, pp. 529–561).

DesRoches, K. J. (1992). A subsidence, compaction, pressure, temperature, and maturity history of the Hibernia B-08 Well, Grand Banks of Newfoundland. Dalhousie University.

Driscoll, N. W., Hogg, J. R., Christie-Blick, N., and Karner, G. D. (1995). Extensional tectonics in the Jeanne d'Arc Basin, offshore Newfoundland: implications for the timing of break-up between Grand Banks and Iberia. In R. A. Scrutton, M. S. Stoker, G. B. Shimmield, and A. W. Tudhope (Eds.), The Tectonics, Sedimentation and Paleoceanography of the North Atlantic Region. Geological Society Special Publication.

Duan, W. M., Hedrick, D. B., Pye, K., Coleman, hf. L., and White, D. C. (1996). A preliminary study of the geochemical and microbiological characteristics of modern sedimentary concretions. Limnology and Oceanography, 41(7), 1404–1414.

Elderfield, H., and Greaves, M. J. (1982). The rare earth elements in seawater. Nature, 296(5854), 214–219.

Enachescu, and Fagan. (2005). Call for Bids 2005 NL05-01.

Enachescu, M. E. (1987). Sedimentary Basins and Basin-Forming Mechanisms. In Memoir (Vol. 12). Canadian Society of Petroleum Geologists.

Estupiñan, J., Marfil, R., Delgado, A., and Permanyer, A. (2007). The Impact of carbonate cements on the reservoir quality in the Napo Fm sandstones (Cretaceous Oriente Basin, Ecuador) The impact of carbonate cement on the Napo Cretaceous sandstones. Geologica Acta, 5, 89–107.

Ethridge, F. (2011). Interpretation of Ancient Fluvial Channel Deposits: Review and Recommendations. In From River to Rock Record: The Preservation of Fluvial Sediments and Their Subsequent Interpretation (Vol. 97, pp. 9–35).

Farrell, K. M. (1987). Sedimentology And Facies Architecture of Overbank Deposits of The Mississippi River, False River Region, Louisiana. In Recent Developments in Fluvial Sedimentology (pp. 111–120). SEPM (Society for Sedimentary Geology).

Fidan, E. (1996). Reservoir Characterization of the Hibernia Formation, Jeanne d'Arc Basin, Gran Banks, Newfoundland. Memorial University of Newfoundland.

Flemming, B. W. (2012). Siliciclastic Back-Barrier Tidal Flats. In R. A. Davis Jr. and R. W. Dalrymple (Eds.), Principles of Tidal Sedimentology (pp. 231–267). Springer Netherlands.

Flügel, E. (2010). Microfacies of Carbonate Rocks: Analysis, Interpretations and Application (2nd ed.). Springer Berlin, Heidelberg.

Fouke, B. W. (1994). Deposition, diagenesis and dolomitization of Neogene Seroe Domi Formation coral reef limestones on Curacao, Netherlands Antilles.

Frank, J. R., Carpenter, A. B., and Oglesby, T. W. (1982). Cathodoluminescence and Composition of Calcite Cement in the Taum Sauk Limestone (Upper Cambrian), Southeast Missouri.

Friedman, I., and O'neil, J. R. (1977). Data of Geochemistry- Compilation of Stable Isotope Fractionation Factors of Geochemical Interest.

Fröhlich, S., Redfern, J., Petitpierre, L., Marshall, J., Power, M., and Grech, P. (2009). Diagenetic evolution of incised channel sandstones: Implications for reservoir characterisation of the lower carboniferous marar formation, ghadames basin, western Libya. Journal of Petroleum Geology, 33, 3–18.

García-García, F., Marfil, R., De Gea, G. A., Delgado, A., Kobstädt, A., Santos, A., and Mayoral, E. (2013). Reworked marine sandstone concretions: A record of high-frequency shallow burial to exhumation cycles. Facies, 59(4), 843–861.

Garzanti, E. (2019). Petrographic classification of sand and sandstone. Earth-Science Reviews, 192, 545–563.

Gaupp, R., Moller, P., Luders, V., Di Primio, R., and Littke, R. (2008). Fluids in sedimentary basins: an overview.

Gautier, D. L., and Claypool, G. E. (1984). Interpretation of Methanic Diagenesis in Ancient Sediments by Analogy with Processes in Modern Diagenetic Environments. In D. A. McDonald and R. C. Surdam (Eds.), Clastic Diagenesis (Vol. 37). American Association of Petroleum Geologist.

German, C. R., and Elderfield, H. (1990). Application of the Ce anomaly as a paleoredox indicator: The ground rules. Paleoceanography, 5(5), 823–833.

Gibbons, K., Hellem, T., Kjemperud, A., Nio, S. D., and Vebenstad, K. (1993). Sequence architecture, facies development and carbonate-cemented horizons in the Troll Field reservoir, offshore Norway. In M. Asthon (Ed.), Advances in Reservoir Geology (69th ed., Issue 69). Geological Society Special Publication.

Grant, A. C., McAlpine, K. D., and Wide, J. A. (1986). The Continental Margin of Eastern Canada: Geological Framework and Petroleum Potential. In M. T. Halbouty (Ed.), Future Petroleum Provinces of the World. AAPG Memoir.

Gyori, O., Hass, J., Hips, K., Lukoczki, G., Budai, T., Demeny, A., Szocs, E. (2019). Dolomitizations of shallow-water, mixed siliciclastic-carbonate sequences: The Lower Triassic ramp succession of the Transdanubian Range, Hungary. Sedimentary Geology, 395.

Hanor, J. S. (1978). Precipitation of beachrock cements; mixing of marine and meteoric waters vs. CO 2 -degassing. Journal of Sedimentary Research, 48(2), 489–501.

Hayes, M. J., and Boles, J. R. (1993). Evidence for meteoric recharge in the San Joaquin basin, California provided by isotope and trace element chemistry of calcite. Marine and Petroleum Geology, 10, 135–144.

Hays, P. D., and Grossman, E. L. (1991). Oxygen Isotopes in Meteoric Calcite Cements as Indicators of Continental Paleoclimate. Geology, 19, 441–444.

Hesse, R., and Abid, I. A. (1998). Carbonate cementation-the key to reservoir properties of four sandstones levels (Cretaceous) in the Hibernia Oilfield, Jeanne d'Arc Basin, Newfoundland, Canada. Spec. Publs Int. Ass. Sediment., 26, 636–393.

Hiscott, R. N., Wilson, R. C. L., Gradstein, E. M., Pujalte, V., Garcia-Mondejar, J., Boudreau, R. R., and Wishart, H. A. (1990). Comparative stratigraphy and subsidence history of Mesozoic rift basin of north Atlantic. The American Association of Petroleum Geologists Bulletin, 74, 60–76.

Hodson, K. R., Crider, J. G., and Huntington, K. W. (2016). Temperature and composition of carbonate cements record early structural control on cementation in a nascent deformation band fault zone: Moab Fault, Utah, USA. Tectonophysics, 690, 240–252.

Hoefs, J. (2006). Stable Isotope Geochemistry (6th Edition). Springer.

Holail, H., and Rashed, M. (1992). Stable isotopic composition of carbonate-cemented recent beachrock along the Mediterranean and the Red Sea coasts of Egypt. Marine Geology, 106(1), 141–148.

Huang, K., Huang, S., Tong, H., Huang, Y., LiHong, L. I. U., and Zhong, Q. (2009). Thermodynamic simulation of carbonate-carbon dioxide equilibrium system during diagenetic processes. Acta Petrologicas Sinica, 25(10), 2417–2424.

Hurley, T. J., Kreisa, R. D., Taylor, G. G., and Yates, W. R. L. (1992). The Reservoir Geology and Geophysics of the Hibernia Field, Offshore Newfoundland.

Irwin, H., Curtis, C., and Coleman, M. (1977). Isotopic evidence for source of diagenetic carbonates formed during burial of organic-rich sediments. Nature, 269(5625), 209–213.

Kaldi, J., Gidman, J. (1982). Early diagenetic dolomite cements: Examples from the Permian Lower Magnesian Limestone of England and the Pleistocene Carbonate of the Bahamas. Journal of Sedimentary Geology, 52 (4), 1072-1085.

Kantorowicz, J. D., Bryant, I. D., and Dawans, J. M. (1987). Controls on the geometry and distribution of carbonate cements in Jurassic sandstones: Bridport Sands, southern England and Viking Group, Troll Field, Norway. In J. D. Marshall (Ed.), Diagenesis of Sedimentary Sequences - Geological Society Special Publication (Vol. 36, pp. 103–118).

Knaust, D. (2017). Atlas of Trace Fossils in Well Core: Appearance, Taxonomy, and Interpretation (1st ed.). Spring Cham.

Kolawole, F., and Evenick, J. C. (2023). Global distribution of geothermal gradients in sedimentary basins. Geoscience Frontiers, 14(6), 101685.

Kyser, K., and Hiatt, E. E. (2003). Fluids in sedimentary basins: An introduction. Journal of Geochemical Exploration, 80(2–3), 139–149.

La Croix, A. D., and Dashtgard, S. E. (2014). Of sand and mud: Sedimentological criteria for identifying the turbidity maximum zone in a tidally influenced river. Sedimentology, 61(7), 1961–1981.

Land, L. S. (1980). The Isotopic and Trace Element Geochemistry of Dolomite: The State of the Art. In D. H. Zenger, J. B. Dunham, and L. Raymond (Eds.), Concepts and Models of Dolomitization (28th ed., Vol. 1). SEPM Special Publication.

Land, L. S. (1983). The Application of Stable Isotopes to Studies of the Origin of Dolomite and to Problems of Diagenesis of Clastic Sediments. In M. A. Arthur, T. F. Anderson, I. R. Kaplan, J. Veizer, and L. S. Land (Eds.), Stable Isotopes in Sedimentary Geology (Vol. 10). SEPM Society of Sedimentary Geology .

Lanz, M. del R., Azmy, K., Cesaretti, N. N., and Fortunatti, N. B. (2021). Diagenesis of the Vaca Muerta Formation, Neuquén Basin: Evidence from petrography, microthermometry and geochemistry. Marine and Petroleum Geology, 124.

Lethbridge, G. D. (2012). A Geological Model of the Hibernia Formation in the Vicinity of the Terra Nova and Hebron Field [MSc thesis]. Memorial University of Newfoundland.

Lin, C. Y., Turchyn, A. V, Krylov, A., and Antler, G. (2020). The microbially driven formation of siderite in salt marsh sediments. Geobiology, 18(2), 207–224.

Lynch, F. L. and Land, L. S. (1996). Diagenesis of calcite cements in Frio Formation sandstones and its relationship to formation water chemistry. Journal of Sedimentary Research, 66(3), 439-446.

Lindholm, R. C., and Finkelman, R. B. (1972). Calcite Staining: Semiquantitative Determination of Ferrous Iron. Journal of Sedimentary Research, 2(1), 239–242.

Longhitano, S. G., Chiarella, D., and Muto, F. (2014). Three-dimensional to two-dimensional cross-strata transition in the lower Pleistocene Catanzaro tidal strait transgressive succession (southern Italy). Sedimentology, 61(7), 2136–2171.

Longhitano, S. G., Mellere, D., Steel, R. J., and Ainsworth, R. B. (2012). Tidal depositional systems in the rock record: A review and new insights. Sedimentary Geology, 279, 2–22.

Longinelli, A., Iacumin, P., and Ramigni, M. (2002). δ18O of carbonate, quartz and phosphate from belemnite guards: implications for the isotopic record of old fossils and the isotopic composition of ancient seawater. Earth and Planetary Science Letters, 203(1), 445–459.

Loucks, R. G., Bebout, D. G., and Galloway, W. E. (1977). Relationship of Porosity Formation and Preservation to Sandstone Consolidation History--Gulf Coast Lower Tertiary Frio Formation (1).

Lu, J., Wilkinson, M., Haszeldine, R. S., and Boyce, A. J. (2011). Carbonate cements in Miller field of the UK North Sea: a natural analog for mineral trapping in CO2 geological storage. Environmental Earth Sciences, 62(3), 507–517.

Luan, G., Azmy, K., Meyer, R., Olanipekun, B., and Dong, C. (2023). Origin of carbonate cements in Ben Nevis sandstones of Jeanne d'Arc Basin: Insights from geochemistry. Marine and Petroleum Geology, 148.

Ludvigson, G. A., González, L. A., Fowle, D. A., Roberts, J. A., Driese, S. G., Villarreal, M. A., Smith, J. J., and Suarez, M. B. (2013). Paleoclimatic applications and modern process studies of pedogenic siderite. SEPM Special Publications, 104, 79–87.

Ludvigson, G. A., González, L. A., Metzger, R. A., Witzke, B. J., Brenner, R. L., Murillo, A. P., and White, T. S. (1998). Meteoric sphaerosiderite lines and their use for paleohydrology and paleoclimatology. Geology, 26(11), 1039–1042.

Ma, B., Cao, Y., Wang, Y., and Jia, Y. (2016). Origin of carbonate cements with implications for petroleum reservoir in Eocene sandstones, northern Dongying depression, Bohai Bay Basin, China. Energy Exploration and Exploitation, 34(2), 199–216.

Macdougall, M. D. J., Braun, A., and Fotopoulos, G. (2021). Evidence of lithospheric boudinage in the grand banks of newfoundland from geophysical observations. Geosciences (Switzerland), 11(2), 1–20.

MacEachern, J., Bhattacharya, J., and Howell, C. (2005). Ichnology of Deltas: Organism Responses to the Dynamic Interplay of Rivers, Waves, Storms, and Tides. SEPM Spec. Publ., 83.

MacEachern, J., Pemberton, G., Gingras, M., and Bann, K. (2010). Ichnology and facies models. Facies Models 4, 19–58.

Machemer, S. D., and Hutcheon, I. (1988). Geochemistry of Early Carbonate Cements in the Cardium Formation, Central Alberta.

Machel, G. M. (2004). Concepts and models of dolomitization: a critical reappraisal. Geological Society, London, Special Publications, 235.

Magoon, L. B., Hudson, T. L., and Peters, K. E. (2005). Egret-Hibernia(!), a significant petroleum system, northern Grand Banks area, offshore eastern Canada. American Association of Petroleum Geologists Bulletin, 89(9), 1203–1237.

Mao, S. W., Bao, Z. D., Wang, X. X., Gao, Y. S., Song, J., Wang, Z. C., Liu, W., Zhang, L., Wei, M. Y., and Bao, Y. F. (2019). Origin of carbonate cements and reservoir evolution of tight sandstone in the Upper Triassic Yanchang Formation, Ordos Basin, China. Australian Journal of Earth Sciences, 66(8), 1175–1194.

Martin, K. D. (2004). A re-evaluation of the relationship between trace fossils and dysoxia. Geological Society, London, Special Publications, 228(1), 141–156.

Mather, C. C. (2020). Dolomite formation within groundwater and arid northwest Australia. Thesis presented for the degree of Doctor of Philosophy. University of Western Australia.

Melim, L. A., Scholle, P. A. (2002). Dolomitization of the Capitan Formation forereef facies (Permian, west Texas and New Mexico): seepage reflux revisited. Sedimentology, 49, 1207-1227.

McAlpine, K. D. (1990). Mesozoic stratigraphy, sedimentary evolution, and petroleum potential of the Jeanne d'Arc Basin, Grand Banks of Newfoundland. Geological Survey of Canada.

Mcbride, E. F., Picard, M. D., and Milliken, K. L. (2003). Calcite-cemented Concretions in Cretaceous Sandstone, Wyoming and Utah, U.S.A. Journal of Sedimentary Research, 73(3), 462–483.

Mcilroy, D., Flint, S., Howell, J., and Timms, N. (2005). Sedimentology of the tide-dominated Jurassic Lajas Formation, Neuquen Basin, Argentina. Geological Society, London, Special Publications, 252, 83–107.

Miall, A. (2010). Alluvial Deposits. In N. P. James and R. W. Dalrymple (Eds.), Facies Models 4. Geological Association of Canada.

Miall, A. D. (1977). A review of the braided-river depositional environment. Earth-Science Reviews, 13(1), 1–62.

Miall, A. D. (1980). Cyclicity and the Facies Model Concept in Fluvial Deposits. Bulletin of Canadian Petroleum Geology, 28(1), 59–79.

Miall, A. D. (1994). Reconstructing Fluvial Macroform Architecture from Two-Dimensional Outcrops: Examples from The Castlegate Sandstone, Book Cliffs, Utah.

Miall, A. D. (1996). The Geology of Fluvial Deposits: Sedimentary Facies, Basin Analysis, and Petroleum Geology, 4th corrected printing (1st ed.). Springer Berlin, Heidelberg.

Milliken, K. L., McBride, E. F., Cavazza, W., Cibin, U., Fontana, D., Picard, M. D., and Zuffa, G. G. (1998). Geochemical History of Calcite Precipitation in Tertiary Sandstones, Northern Apennines, Italy. In Carbonate Cementation in Sandstones (pp. 213–239).

Molenaar, N. (1998). Origin of Low-Permeability Calcite-Cemented Lenses in Shallow Marine Sandstones and CaCO3 Cementation Mechanisms: An Example from the Lower Jurassic Luxemburg Sandstone, Luxemburg. In Carbonate Cementation in Sandstones (pp. 193–211). John Wiley and Sons, Ltd.

Moore, S. E., Ferrell, R. E., and Aharon, P. (1992). Diagenetic siderite and other ferroan carbonates in a modern subsiding marsh sequence. Journal of Sedimentary Research, 62(3), 357–366.

Moore, C. H. (2001). Dolomitization associated with meteoric and mixed meteoric-marine waters. In Carbonate reservoirs: Porosity evolution and diagenesis in a sequence stratigraphic framework. Developments in Sedimentology, Elservier.

Morad, S. (1998). Carbonate cementation in sandstones: distribution patterns and geochemical evolution. Spec. Publs Int. Ass. Sediment. , 26, 1–26.

Morad, S., Marfil, R., Ai-Aasm, I. S., and Gomez-Gras, D. (1992). The role of mixing-zone dolomitization in sandstone cementation: evidence from the Triassic Buntsandstein, the Iberian Range, Spain. Sedimentary Geology, 80, 53–65.

Mulder, T., and Alexander, J. (2001). The physical character of subaqueous sedimentary density flows and their deposits. Sedimentology, 48(2), 269–299.

Mulder, T., Syvitski, J., Migeon, S., Faugères, J.-C., and Savoye, B. (2003). Marine hyperpycnal flows: Initiation, behaviorand related deposits. A review. Marine and Petroleum Geology, 20, 861–882.

Nio, S.-D., and Yang, C.-S. (1991). Diagnostic Attributes of Clastic Tidal Deposits: A Review. CSPG Special Publications: Clastic Tidal Sedimentology - Memoir 16, 3–27.

Normore, L. S. (2006). Origin, distribution and paragenetic sequence of carbonate cements in the Ben Nevis Formation, White Rose Field, Jeanne d'Arc Basin, offshore Newfoundland, Canada (MSc. Thesis). Memorial University of Newfoundland.

Nothdurft, L. D., Webb, G. E., and Kamber, B. S. (2004). Rare earth element geochemistry of Late Devonian reefal carbonates, Canning Basin, Western Australia: confirmation of a seawater REE proxy in ancient limestones. Geochimica et Cosmochimica Acta, 68(2), 263–283.

Octavian, C., Galloway, W., Kendall, C., Miall, A., Posamentier, H., Strasser, A., and Tucker, M. (2011). Sequence Stratigraphy: Methodology and Nomenclature. Newsletters on Stratigraphy, 44, 173–245.

Odigi, M. I., and Amajor, L. C. (2010). Geochemistry of carbonate cements in Cretaceous sandstones, southeast Benue Trough, Nigeria: Implications for geochemical evolution of formation waters. Journal of African Earth Sciences, 57(3), 213–226.

Olanipekun, B., and Azmy, K. (2022). Carbonate cementation in the Tithonian Jeanne d'Arc sandstone, Terra Nova Field, Newfoundland: Implications for reservoir quality evolution. Sedimentology, 69(2), 461–500.

Olariu, C., and Bhattacharya, J. P. (2006). Terminal distributary channels and delta front architecture of river-dominated delta systems. Journal of Sedimentary Research, 76(2), 212–233.

Olariu, C., Steel, R. J., Dalrymple, R. W., and Gingras, M. K. (2012). Tidal dunes versus tidal bars: The sedimentological and architectural characteristics of compound dunes in a tidal seaway, the lower Baronia Sandstone (Lower Eocene), Ager Basin, Spain. Sedimentary Geology, 279, 134–155.

Pemberton, G., MacEachern, J., Dashtgard, S., Bann, K., Gingras, M., and Zonneveld, J.-P. (2012). Shorefaces. In Developments in Sedimentology (Vol. 64, pp. 563–603).

Pemberton, G., Wagoner, J., and Wach, G. (1992). Ichnofacies of a wave-dominated shoreline. SEPM Core Workshop (Society of Economic Paleontologists and Mineralogists), 17, 339–382.

Posamentier, H. W., and Allen, G. P. (1999). Siliciclastic Sequence Stratigraphy: Concepts and Aplications (Vol. 7). SEPM Society of Sedimentary Geology.

Purvis, K., Dennis, P., Holt, L., and Marca, A. (2020). The origin of carbonate cements in the Hildasay reservoir, Cambo Field, Faroe-Shetland Basin; clumped isotopic analysis and implications for reservoir performance. Marine and Petroleum Geology, 122.

Rahimi, A., Adabi, M. H., Aghanabati, A., Majidifard, M. R., and Jamali, A. M. (2016). Dolomitization Mechanism Based on Petrography and Geochemistry in the Shotori Formation (Middle Triassic), Central Iran. Open Journal of Geology, 06(09), 1149–1168.

Ramm, M. (1992). Porosity-depth trends in reservoir sandstones: theoretical models related to Jurassic sandstones offshore Norway.

Rider, M. H. (1996). The Geological Interpretation of Well Logs (2nd ed.). Whittles Publishing.

Rieger, P., Magnall, J. M., Gleeson, S. A., Oelze, M., Wilke, F. D. H., and Lilly, R. (2022). Differentiating between hydrothermal and diagenetic carbonate using rare earth element and yttrium (REE+Y) geochemistry: a case study from the Paleoproterozoic George Fisher massive sulfide Zn deposit, Mount Isa, Australia. Mineralium Deposita.

Saigal, G. C., and Bjorlykke, K. (1987). Carbonate cements in clastic reservoir rocks from offshore Norway-relationships between isotopic composition, textural development, and burial depth. In J. D. Marshall (Ed.), Diagenesis of Sedimentary Sequences (Vol. 36, pp. 313–324). Geological Society Special Publications.

Sanei, H. (2020). Genesis of solid bitumen. Scientific Reports, 10(1).

Savdram, C., and Bottjer, D. (1991). Oxygen-related biofacies in marine strata: an overview and update. Geological Society, London, Special Publications, 58(1), 201–219.

Schmidt, V., and Mcdonald, D. A. (1979). Texture and Recognition of Secondary Porosity in Sandstones. In P. A. Scholle and P. R. Schluger (Eds.), Aspects of Diagenesis.

Scholle, P. A., and Ulmer-Scholle, D. S. (2003). A Color Guide to the Petrography of Carbonate Rocks: Grains, textures, porosity, diagenesis. American Association of Petroleum Geologist.

Scotchman, I. C. (1991). The geochemistry of concretions from the Kimmeridge Clay Formation of southern and eastern England. In Sedimentology (Vol. 38).

Sengupta, R., Robinson, S. A., and Tosca, N. J. (2021). Sphaerosiderites as sensitive recorders of non-marine depositional and diagenetic history: Insights from the Lower Cretaceous Wealden Supergroup. The Depositional Record, 7(3), 520–540.

Sibley, D. F., and Gregg, J. M. (1987). Classification of dolomite rock textures. Journal of Sedimentary Research, 57(6), 967–975.

Sinclair, I. K. (1988). Evolution Of Mesozoic-Cenozoic Sedimentary Basins in The Grand Banks Area of Newfoundland and Comparison with Falvey's (1974) Rift Model. Bulletin Of Canadian Petroleum Geology, 36(3).

Sinclair, I. K. (1992). Tectonism: the dominant factor in mid-Cretaceous deposition in the Jeanne d'Arc Basin, Grand Banks. Marine and Petroleum Geology.

Sinclair, I. K., Evans, J. E., Albrechtsons, E. A., and Sydora, L. J. (1999). The Hibernia Oilfield-effects of episodic tectonism on structural character and reservoir compartmentalization. In A. J. Fleet and S. A. R. Boldy (Eds.), Petroleum Geology of the Northwest Europe: Proceedings of the 5th Conference (pp. 517–528). Geological Society.

Sinclair, I. K., Flint, S., Stokes, R., and Bidgood, M. (2005). Hibernia Formation (Cretaceous) Sequences and Breathitt Group (Pennsylvanian) Analogue-Implications for Reservoir Compartmentalization and Modelling, Offshore Newfoundland.

Surdam, R. C., Boese, S. W., and Crossey, L. J. (1984). The Chemistry of Secondary Porosity. In D. A. McDonal and R. C. Surdam (Eds.), Clastic Diagenesis (Vol. 1). American Association of Petroleum Geologist.

Taberner, C., and Santisteban, C. (1987). Mixed-water dolomitization in a transgressive beach-ridge system, Eocene Catalan Basin, NE Spain. Geological Society, London, Special Publications, 36(1), 123–139.

Tankard, A. J., and Balkwill, H. R. (1989). Extensional Tectonics and Stratigraphy of the North Atlantic Margins: Introduction: Chapter 1.

Tankard, A., and Welsink, H. J. (1987). Extensional Tectonics and Stratigraphy of Hibernia Oil Field, Grand Banks, Newfoundland.' The American Association of Petroleum Geologist Bulletin, 71(10).

Taylor, K. G., Gawthorpe, R. L. (2003). Basin-scale dolomite cementation of shoreface sandstones in response to sea-level fall. GSA Bulletin, 115 (10), 1218-1229.

Varol, B., Magaritz, M. (1992). Dolomitization, time boundaries and unconformities: examples from the dolostone of the Taurus Mesozoic sequence, south-central Turkey. Sedimentary Geology, 76, 117-133.

Vasconcelos, C., and McKenzie, J. A. (1997). Microbial mediation of modern dolomite precipitation and diagenesis under anoxic conditions (Lagoa Vermelha, Rio de Janeiro, Brazil). Journal of Sedimentary Research, 67(3), 378–390.

Veizer, J. (1983). Trace elements and isotopes in sedimentary carbonates. Reviews in Mineralogy, 11.

Veizer, J., Ala, D., Azmy, K., Bruckschen, P., Buhl, D., Bruhn, F., Carden, G. A. F., Diener, A., Ebneth, S., Godderis, Y., Jasper, T., Korte, C., Pawellek, F., Podlaha, O. G., and Strauss, H. (1999). 87Sr/86Sr, δ13C and δ18O evolution of Phanerozoic seawater. Chemical Geology, 161, 59–88.

Wang, F. H., Honarpour, M. M., Djabbarah, N. F., Chiasson, C. G., Glotzbach, R. C., Klimentidis, R. E., and Leitzel, G. L. (2005). Double Displacement Laboratory Investigation for Hibernia Q-Block.

Ward, W. C., and Halley, R. B. (1985). Dolomitization in a Mixing Zone of Near-Seawater Composition, Late Pleistocene, Northeastern Yucatan Peninsula. Journal of Sedimentary Research, 55, 407–420.

Warren, J. (2000). Dolomite: occurrence, evolution, and economically important associations. Earth-Science Reviews, 52(1), 1–81.

Webb, G. E., Nothdurft, L. D., Kamber, B. S., Kloprogge, J. T., and Zhao, J.-X. (2009). Rare earth element geochemistry of scleractinian coral skeleton during meteoric diagenesis: a sequence through neomorphism of aragonite to calcite. Sedimentology, 56(5), 1433–1463.

Weedman, S. D., Brantley, S. L., Shiraki, R., and Poulson, S. R. (1996). Diagenesis, Compaction, and Fluid Chemistry Modeling of a Sandstone Near a Pressure Seal: Lower Tuscaloosa Formation, Gulf Coast. AAPG Bulletin, 80(7), 1045–1063.

Welsford, B. (1993). Petrography, Diagenesis, and Carbonate Cement Geochemistry on the Sandstones of the Jurassic Jeanne d' Arc Formation, Jeanne d'Arc Basin, Grand Banks. Thesis Submitted to

the Faculty of Graduate Studies and Research in Partial Fulfilment of the Requirements for the Degree of Master of Science.

Williamson, M. A., Desroches, K., King, S., Williamson, M. A., Desroches, K., and King, S. (1993). Overpressures and hydrocarbon migration in the Hibernia-Nautilus area of the Jeanne d'Arc Basin, offshore Newfoundland. In Bulletin of Canadian Petroleum Geology (Vol. 41, Issue 4).

Withjack, M. O., and Schlische, R. W. (2005a). A Review of tectonic events on the passive margin of Eastern North America.

Withjack, M. O., and Schlische, R. W. (2005b). A Review of Tectonic Events on the Passive Margin of Eastern North America. In P. P. Post, N. C. Rosen, D. L. Olson, S. L. Palmes, K. T. Lyons, and G. B. Newton (Eds.), Petroleum Systems of Divergent Continental Margin Basins.

Worden, R. H., and Smith, L. K. (2004). Geological sequestration of CO2 in the subsurface: lessons from CO2 injection enhanced oil recovery projects in oilfields. Geological Society, London, Special Publications, 233(1), 211–224.

Xiong, D., Azmy, K., and Blamey, N. J. F. (2016). Diagenesis and origin of calcite cement in the Flemish Pass Basin sandstone reservoir (Upper Jurassic): Implications for porosity development. Marine and Petroleum Geology, 70, 93–118.

Yuan, G., Cao, Y., Zhang, Y., and Gluyas, J. (2017). Diagenesis and reservoir quality of sandstones with ancient "deep" incursion of meteoric freshwater - An example in the Nanpu Sag, Bohai Bay Basin, East China. Marine and Petroleum Geology, 82, 444–464.

Zamanzadeh, S. M., Amini, A., and Ghavidel-Syooki, M. (2009). Sequence stratigraphic controls on early diagenetic carbonate cementation of shallow marine clastic sediments (the Devonian Zakeen Formation, southern Zagros, Iran). Geosciences Journal, 13(1), 31–57.

Chapter 3: Summary

Carbonate cements in siliciclastic reservoirs act as potential barriers or baffles for fluid flow, significantly reducing porosity and permeability (Macaulay et al., 2009). Carbonate cements have been reported and analyzed in the Hibernia Formation in past studies (e.g., Brown et al., 1989; Hesse and abid, 1998). Here, calcite, dolomite and siderite reduce porosity and permeability leading to poor reservoir quality and heterogeneity. Nonetheless, the genesis of these cements and potential links with the reservoir stratigraphy and facies associations had yet to be well established. Strata of the Lower Cretaceous Hibernia Formation comprise the main reservoirs of the Hibernia field, Jeanne d'Arc basin, and is subdivided into two members: the Lower Hibernia zone and the Upper Hibernia zone (Brown et al., 1989; Sinclair et al., 2005). This thesis aimed to develop a better understating of the stratigraphic or structural controls on carbonate cements in the Lower Hibernia zone, using a combined approach of facies analysis, sequence stratigraphy, petrography, and geochemistry to define links between the chemical and sedimentary constraints on cement formation.

Core and well logs observations carried out in the Lower Hibernia zone record the transition from a deltaic to an estuarine environment and it is composed of six facies associations: delta front (FA1), braided fluvial (FA2), marginal marine tidal-fluvial channels (FA3), tidal flats (FA4), marine offshore (FA5) and tidal bars (FA6). Starting at its base, facies association 1 within the Layer 4, overlies fine-grained strata of the Fortune Bay Formation that record six stacked sequences of shale grading upward to siltstone indicating prodeltaic and delta from sedimentation (McAlpine, 1990). An erosive surface, interpreted as a sequence boundary, separates the delta front strata from the overlying braided fluvial strata of FA2. This erosive surface suggests a loss of the delta front coinciding with a forced regression before the onset of fluvial sedimentation. Fining-upward

succession of marginal marine channels (FA3) and tidal flats (FA4) in Layer 3 Upper overlie the braided fluvial strata (FA2) and represent the fluvial tidal transition of the estuarine system. Increased rates of subsidence led to the tidal-fluvial sedimentation of FA3 - FA4 succeeded by the offshore marine deposition of FA5 in the Medial Shale, resulting in progressive transgression and retrogradation of the fluvial-deltaic system. A sudden drop of sea level is indicated by a second erosive sequence boundary, separating the Medial Shale from Layer 2, followed by the deposition of fining-upward succession of FA3 and FA4 in a tidal-fluvial setting. The final episode phase of sedimentation is characterized by a rise in sea level, indicated by the coarsening-upward successions of subtidal sand bars (FA6) recorded in Layer 1.

The reservoir strata of the Lower Hibernia zone are characterized by well-sorted, fine- to coarse-grained quartzose sandstone exhibiting variable amounts and types of carbonate cements. Petrographic analysis indicates three main pervasive carbonate cements in the Lower Hibernia zone: early calcite, early dolomite and late ferroan calcite. Ferroan calcite cements predominate in abundance, whereas dolomite cements are the least prevalent. These cements generally form stratabound layers. However, ferroan calcite may not always align perfectly parallel to bedding. Minor pore-filling cements, such as grain-rimming micrite, siderite and ferroan dolomite, exhibit lower abundance compared to ferroan calcite and calcite. Stratabound layers of calcite were observed mainly in marginal marine fluvial-tidal channels (FA3), offshore marine (FA5) and tidal sand bars (FA6). Calcite cements exhibit a poikilotopic texture and retain high intergranular volumes (35% IGV) compared to the potential initial intergranular volume of well-sorted sandstones (42%; Beard and Weyl, 1973), indicating pre-burial cementation. Higher Mn contents compared to Fe indicate that calcite precipitated in a more reduced environment rather than an oxidizing setting. Furthermore, the REE content and patterns closely resembles the REE pattern of

present-day seawater. The $\delta^{18}O$ composition of calcite cements is relatively lower than the best-preserved lower cretaceous marine carbonates ($\delta^{18}O$= -2 ‰ VPBD; Veizer et al., 1999). Its composition suggests that the parent fluids were most likely composed of marine and meteoric waters with carbon derived from organic matter oxidation and bacterial sulfate reduction as indicated by the $\delta^{13}C$ composition ($\delta^{18}O_{calcite}$ = -7.7 to -4.2 ‰ VPDB). Dolomite cements occur in delta front and offshore marine facies associations, showing a high intergranular volume (35% IGV), indicating pre-burial dolomite formation. Additionally, dolomite exhibits a planar-s fabric which is typical of slow crystal growth at low temperatures (Sibley and Gregg, 1987; Rahimi et al., 2016). The Mg source of dolomite cements is attributed to seawater contributions and compactional fluid expulsion from adjacent shales. The $\delta^{18}O$ composition of dolomite cements ($\delta^{18}O_{dolomite}$ = -4.1 to -1.6 ‰ VPDB) also reflects mixing of marine and meteoric waters.

The widespread occurrence of ferroan calcite layers in the Lower Hibernia zone indicates a potential lack of stratigraphic control on its distribution. The reduced intergranular volume of ferroan calcite-cemented sandstones (22 – 28% IGV) compared to calcite- and dolomite-cemented samples, suggests ferroan calcite formation in a more complicated sandstone likely during burial likely at higher temperatures as inferred from the depleted $\delta^{18}O$ composition ($\delta^{18}O_{ferroan\text{-}calcite}$ = -10.2 to -9.1 ‰ VPDB). The coexistence of ferroan calcite with solid bitumen also indicates that ferroan calcite formation occurred coeval with the oil emplacement. In addition, the high concentrations of Fe and Mn, along with the lack of negative Ce anomalies of ferroan calcite and saddle ferroan dolomite suggest formation under reducing conditions. The resemblance in REE_{SN} between ferroan calcite and saddle ferroan dolomite, along with the petrographic observations, suggest a common origin from late diagenetic fluids in a burial environment.

The reservoir stratigraphy and sea-level fluctuations of the Lower Hibernia zone control the early carbonate cementation. Pore-filling dolomite mosaics in sandstones and siltstones of FA1 and FA5 underlying the two sequence boundaries coincide with the forced regressions during the deposition of the Lower Hibernia zone. The dolomitizing pore fluid were composed of meteoric and marine water as evidenced by the $\delta^{18}O$ composition and trace element geochemistry of the investigated dolomite cements. Sea level regressions facilitated the retention of seawater and/or marine-meteoric waters within sediments. This, combined with fluid expulsion due to the compaction of the underlying Fortune Bay Formation and Medial Shale, led to dolomite supersaturation and subsequent dolomite cementation. Calcite formation occurred mainly in tidal-fluvial, tidal facies and offshore marine facies by the massive incursion of seawater during transgressions.

Finally, the occurrence of dissolution textures in sandstones of FA2, FA3 and FA4 provides evidence of carbonate dissolution, as documented in previous studies (Brown et al., 1989; Hesse and Abid, 1998). The influx of meteoric waters and basinal pore fluids promotes the dissolution of carbonate cements (Yuan et al. 2019). During the first stages of burial, acidic pore water might have infiltrated the Hibernia Formation via the preexisting NE-SW-trending fault system, resulting in the dissolution of early carbonate cements. This dissolution likely contributed to the development of secondary porosity, thereby enhancing the porosity and permeability of the reservoir units.

3.1 References

Badiozamani, K. (1973). The Dorag Dolomitization Model-Application to The Middle Ordovician of Wisconsin. Journal Of Sedimentary Petrology, 43(4), 965–984.

Brown, D. M., Mcalpine, K. D., and Yole, R. W. (1989). Sedimentology and Sandstone Diagenesis of Hibernia Formation in Hibernia Oil Field, Grand Banks of Newfoundland^ modeling constrains the interpreted time and depth of hydrocarbon generation and accumulation in the sand-stone reservoirs.

Beard, D. C., and Weyl, P. K. (1973). Influence of Texture on Porosity and Permeability of Unconsolidated Sand. AAPG Bulletin, 57(2), 349–369.

Hesse, R., and Abid, I. A. (1998). Carbonate cementation-the key to reservoir properties of four sandstones levels (Cretaceous) in the Hibernia Oilfield, Jeanne d'Arc Basin, Newfoundland, Canada. Spec. Publs Int. Ass. Sediment., 26, 636–393.

McAlpine, K. D. (1990). Mesozoic stratigraphy, sedimentary evolution, and petroleum potential of the Jeanne d'Arc Basin, Grand Banks of Newfoundland. Geological Survey of Canada.

Macaulay, C., Fallick, A. E., Mclaughlin, O., Haszeldine, R., and Pearson, M. (1998). The Significance of 13C of Carbonate Cements in Reservoir Sandstones: A Regional Perspective from the Jurassic of the Northern North Sea (Vol. 26, pp. 395–408).

Rahimi, A., Adabi, M. H., Aghanabati, A., Majidifard, M. R., and Jamali, A. M. (2016). Dolomitization Mechanism Based on Petrography and Geochemistry in the Shotori Formation (Middle Triassic), Central Iran. Open Journal of Geology, 06(09), 1149–1168.

Sibley, D. F., and Gregg, J. M. (1987). Classification of dolomite rock textures. Journal of Sedimentary Research, 57(6), 967–975.

Sinclair, I. K., Flint, S., Stokes, R., and Bidgood, M. (2005). Hibernia Formation (Cretaceous) Sequences and Breathitt Group (Pennsylvanian) Analogue-Implications for Reservoir Compartmentalization and Modelling, Offshore Newfoundland.

Taberner, C., and Santisteban, C. (1987). Mixed-water dolomitization in a transgressive beach-ridge system, Eocene Catalan Basin, NE Spain. Geological Society, London, Special Publications, 36(1), 123–139.

Yuan, G., Cao, Y., Zhang, Y., and Gluyas, J. (2017). Diagenesis and reservoir quality of sandstones with ancient “deep” incursion of meteoric freshwater - An example in the Nanpu Sag, Bohai Bay Basin, East China. Marine and Petroleum Geology, 82, 444–464.

Appendix 1

Minor elements results of carbonate cements by LA-ICP-MS

Cem./Sam.	Mg (ppm)	Mn (ppm)	Fe (ppm)	Sr (ppm)	Y (ppm)	U (ppm)
	17940	3531	257	547	1.68	0.04
	17470	3579	23.70	542	1560	0.02
	17130	3500	48	538	1.21	0.01
	18260	3713	450	569	2.51	0.05
	17980	3501	25.80	572	1.69	0.00
	17120	3564	33	546	1.31	0.00
	17170	3523	24.90	540	1.58	0.00
	17440	2541	22.20	631	0.95	0.03
Calcite	18360	2726	25	665	1.12	0.04
S14	19040	2426	37	651	0.90	0.03
	18150	2379	23	647	1.00	0.03
	17030	2603	20.70	583	1.19	0.02
	17400	2665	16	637	1.83	0.04
	16670	2599	18.20	607	1.98	0.04
	16680	2591	28.60	596	1.80	0.03
	18550	2474	18	646	0.43	0.02
	16810	2589	20.30	583	0.99	0.03
	18810	2682	17	687	1.13	0.02
	12860	2120	7040	653	11.40	0.21
	15840	2135	3227	612	5.86	0.12
	15810	2132	2611	581	6.61	0.08
	16410	2140	2667	600	6.01	0.07
Calcite	19420	2360	1760	526	3.94	0.17
S16	19320	2174	10.40	565	2.41	0.03
	16900	2279	13.50	519	4.03	0.05
	17910	2163	20.50	538	7.51	0.05
	18950	2321	22.10	548	5.78	0.05
	17510	2274	45	520	4.65	0.04

Cem./Sam.	Mg (ppm)	Mn (ppm)	Fe (ppm)	Sr (ppm)	Y (ppm)	U (ppm)
	3065	2212	14540	974	3.35	0.02
	3365	2228	15410	903	6.50	0.03
	3130	2234	14680	619	9.40	na
	2810	2124	13390	790	13.86	0.04
	3034	2212	14580	685	3.15	0.00
	3519	2292	16190	883	1.90	0.00
Ferroan	3370	2305	16090	890	3.56	0.00
Calcite	3119	2185	14730	922	4.42	0.01
S15	3027	1991	13680	1074	3.47	0.01
	2798	2047	13120	871	7.03	0.01
	3368	2312	15550	696	3.39	0.02
	3175	2287	15530	812	4.05	0.01
	2511	1941	12560	1180	1.62	0.01
	2620	2010	12990	1077	6.12	0.03
	2118	1874	13330	1703	3.09	0.01
	1460	1965	6370	704	80.10	1.62
	1684	2066	7140	637	43.60	0.53
	1610	2052	6820	573	28.90	0.17
	1286	2033	5870	680	33.40	0.17
	1319	1811	6540	569	28.90	0.17
	3244	2034	13530	1021	40.40	0.62
	2178	2354	9310	399	13.40	0.06
Ferroan	2910	1910	12960	923	32.50	0.43
Caclite	3170	1857	13500	903	24.90	0.25
S16	2738	2560	11780	442	10.08	0.02
	751	1601	4310	476	21.26	na
	2300	2100	9740	522	24.50	0.48
	2586	2708	10530	448	13.42	0.03
	4880	1889	17390	722	50.80	1.02
	4590	1847	16560	687	32.00	0.52
	3850	2035	14290	790	24.10	0.23

Cem./Sam.	Mg (ppm)	Mn (ppm)	Fe (ppm)	Sr (ppm)	Y (ppm)	U (ppm)
Ferroan Dolomite S12	76400	2558	71200	338.30	14.06	0.92
	77100	2540	49200	385.30	12.38	0.55
	73800	2236	50700	389.70	10.51	0.50
	83700	2196	48500	321.20	20.30	1.66
	76500	1952	43100	567	11.32	0.46
	71000	2405	48200	589	10.47	0.64
	71300	2433	48700	462	9.38	0.70
	38000	1343	38500	590	18.02	0.56
	76300	2497	42800	586	12.23	0.86
	71200	2620	46900	451	9.31	0.68
	70300	2267	52800	427	9.39	0.59
Saddle Ferroan Dolomite S10	81600	1751	81400	411	35.9	1.66
	82800	1769	86000	352	44.2	2.27
	84600	1787	84800	435	47.0	2.59
	86700	1755	84000	387.50	39.6	na
	88900	1760	77500	352	43.7	3.55
	86900	1770	78900	331	40.9	3.03
	79600	1791	84300	351	43.1	2.37
	84000	1907	90300	322.2	40.2	1.63
	88100	1761	80400	336.4	41.5	2.91
	95900	1894	78600	280.7	45.1	3.68
	93700	1964	80100	285.7	34.0	2.19
	86800	1900	91800	253	50.6	2.72
	84800	1802	86700	281.7	43.6	2.13
	81300	1723	77300	394.6	35.7	2.21
	82700	1751	83100	307.0	43.3	2.20
	89700	1757	72200	384.8	39.7	3.93
	82300	1699	74200	511	38.4	2.96

Cem./Sam.	Mg (ppm)	Mn (ppm)	Fe (ppm)	Sr (ppm)	Y (ppm)	U (ppm)
Siderite S16	25900	14200	425000	96.90	80.80	1.21
	36900	7960	433000	108.60	75.40	1.79
	46700	7890	433000	102.10	99.70	2.89
	40000	8200	409000	121	126	2.82
	39900	7970	428000	121	89.90	2.08
	21200	8000	300000	335	72.50	0.99
Siderite 10	19000	3910	377000	172.40	10.23	3.77
	18640	3590	391000	171.80	8.30	3.71
	20240	3560	396000	160.90	10.12	2.67
	19730	3840	401000	143.30	9.83	2.93
	18590	3690	401000	138.90	9.05	2.88
	17400	3460	289000	338	12.25	4.89
	18000	3650	380000	171.50	9.57	3.81
	19200	3630	360000	196.50	9.92	4.61
	18800	3660	393000	154.70	8.79	3.25
	19790	3920	408000	136.20	9.38	2.79
	19210	3550	386000	190.20	8.52	3.63
	19330	3508	376000	180.40	8.69	3.82
	20190	3615	378000	179.20	9.29	3.57
	20020	3660	390000	173.80	8.61	3.29
	20100	3690	380000	175.10	7.90	3.40

Appendix 2

REE concentrations of carbonate cements by LA-ICP-MS

Cem./Sam.	La (ppm)	Ce (ppm)	Pr (ppm)	Nd (ppm)	Sm (ppm)	Eu (ppm)	Gd (ppm)	Tb (ppm)	Dy (ppm)	Ho (ppm)	Er (ppm)	Tm (ppm)	Yb (ppm)	Lu (ppm)
Calcite S14	0.43	0.93	0.13	0.60	0.10	0.06	0.19	na	0.16	0.04	0.12	0.03	0.08	0.02
	0.17	0.40	0.06	0.29	0.08	0.03	0.17	0.04	0.18	0.06	0.11	na	0.08	0.02
	0.13	0.35	0.04	0.27	0.09	0.02	na	0.03	0.15	na	0.07	0.01	0.10	na
	0.92	2.00	0.25	1.02	0.27	0.14	0.52	0.05	0.41	0.11	0.13	0.04	0.17	na
	0.19	0.49	0.06	0.29	0.14	0.04	0.26	0.04	0.21	0.05	0.11	0.01	0.09	0.04
	0.20	0.32	0.06	0.25	0.04	na	na	na	0.18	0.04	0.06	0.01	0.07	na
	0.19	0.38	0.04	0.26	0.07	na	0.17	0.03	0.17	0.05	0.07	na	0.06	na
	0.23	0.61	0.07	0.41	0.12	na	0.22	na	0.21	0.05	0.09	0.01	0.05	na
	0.30	0.58	0.10	0.43	na	na	na	0.02	0.20	0.03	0.09	0.01	na	0.01
	0.19	0.48	0.08	0.41	0.12	0.02	0.30	0.03	0.19	0.04	0.10	0.01	0.07	0.01
	0.19	0.49	0.06	0.38	0.14	na	0.20	0.04	0.14	0.04	0.08	0.01	0.03	0.01
	0.25	0.63	0.09	0.38	0.14	na	0.15	0.03	0.23	0.03	0.06	na	0.05	na
	0.39	1099	0.19	0.71	0.27	0.09	0.39	0.06	0.38	0.05	0.18	0.02	0.14	0.02
	0.35	1036	0.16	0.75	0.23	0.09	0.42	0.06	0.34	0.06	0.18	0.02	0.07	na
	0.35	1.03	0.13	0.53	0.33	0.08	0.37	0.08	0.35	0.07	0.14	0.02	0.19	0.02
	0.12	0.25	0.03	0.13	na	na	0.06	na	0.07	0.01	na	na	na	0.02
	0.23	0.52	0.08	0.36	0.17	na	0.21	0.02	0.17	0.03	0.05	na	na	0.01
	0.22	0.56	0.11	0.51	0.12	0.05	0.25	0.03	0.24	0.03	0.06	0.02	0.08	na
Calcite S16	3.07	9.60	1.31	7.19	2.23	0.71	3.94	0.38	1.99	0.35	0.79	0.11	0.73	0.07
	1.80	5.21	0.76	3.49	1.26	0.35	1.70	0.21	1.11	0.20	0.48	0.06	0.35	0.04
	1.83	5.56	0.86	4.05	1.31	0.40	1.73	0.22	1.27	0.22	0.64	0.07	0.50	0.06
	2.02	5.55	0.74	3.88	1.29	0.38	1.64	0.21	1.25	0.23	0.52	0.06	0.41	0.05
	3.32	6.35	0.68	2.60	0.75	0.19	1.02	0.15	0.72	0.13	0.38	0.04	0.17	0.04
	0.76	1.88	0.32	1.42	0.49	0.13	0.67	0.08	0.43	0.08	0.16	0.03	0.13	0.01
	1060	2.90	0.43	2.19	0.79	0.22	1.02	0.15	0.79	0.14	0.32	0.04	0.19	0.04
	1.77	5.87	0.89	4.53	1.49	0.40	2.03	0.24	1.39	0.27	0.70	0.08	0.41	0.08
	1563	4.48	0.66	3.04	1.10	0.29	1.43	0.20	1.01	0.22	0.51	0.05	0.34	0.05
	1191	3.40	0.48	2.69	0.89	0.25	1.13	0.17	0.89	0.15	0.41	0.05	0.25	0.04

Cem./Sam.	La (ppm)	Ce (ppm)	Pr (ppm)	Nd (ppm)	Sm (ppm)	Eu (ppm)	Gd (ppm)	Tb (ppm)	Dy (ppm)	Ho (ppm)	Er (ppm)	Tm (ppm)	Yb (ppm)	Lu (ppm)
Ferroan Calcite S15	2.70	3.71	0.37	1.66	0.33	0.13	0.73	0.09	0.37	0.08	0.17	0.02	0.05	0.02
	2.32	4.69	0.59	3.03	0.94	0.30	1.30	0.21	1.15	0.24	0.64	0.08	0.37	0.06
	3.61	7.25	0.81	4.20	1.30	0.36	2.14	0.25	1.50	0.26	0.53	0.09	0.33	0.07
	5.23	11.55	1.39	6.53	1.91	0.55	3.11	0.46	2.51	0.44	1.26	0.14	0.74	0.09
	1.96	3.06	0.35	1.48	0.32	0.11	0.62	0.08	0.32	0.08	0.18	0.02	0.08	0.01
	0.82	1452	0.18	1.05	0.18	0.06	0.42	0.04	0.20	0.05	0.09	0.01	na	0.01
	1.42	2.80	0.33	1.66	0.46	0.14	0.54	0.10	0.49	0.10	0.31	0.03	0.11	0.02
	2.26	4.22	0.47	2.17	0.61	0.17	1.01	0.16	0.72	0.12	0.31	0.04	0.12	0.03
	2.49	3.89	0.35	1.66	0.45	0.10	0.59	0.10	0.45	0.09	0.23	0.03	0.13	0.02
	4.42	8.11	0.79	3.83	0.98	0.26	1.31	0.18	1.24	0.18	0.50	0.04	0.30	0.04
	1.70	2.99	0.34	1.59	0.43	0.14	0.69	0.10	0.51	0.09	0.22	0.01	0.12	0.02
	2.04	3.29	0.37	1.84	0.42	0.14	0.81	0.10	0.59	0.11	0.22	0.02	0.06	0.03
	1176	1.61	0.16	0.88	0.23	0.08	0.37	0.03	0.15	0.04	0.08	0.00	na	0.01
	3.07	6.12	0.66	3.09	0.81	0.27	1.28	0.17	1.05	0.20	0.45	0.07	0.23	0.06
	1022	2.24	0.29	1.39	0.51	0.12	0.71	0.11	0.58	0.09	0.29	0.03	0.17	0.02
Ferroan Caclite S16	14.33	64.10	11.88	72.60	29.00	8.41	40.50	4.07	17.50	2.63	4.77	0.48	2.05	0.20
	6.88	30.50	5.46	33.20	12.10	3.64	17.50	1.99	9.21	1.20	2.61	0.23	1.31	0.13
	4.24	20.00	3.74	20.62	8.73	2.44	12.59	1.25	5.46	0.82	1.61	0.19	0.77	0.11
	5.14	24.90	4.55	28.60	11.50	3.34	16.10	1.65	6.44	1.02	1.91	0.22	0.95	0.17
	2.32	12.20	2.22	14.10	6.76	1.99	9.73	1.21	5.31	0.80	1.61	0.20	1.01	0.13
	7.13	21.27	2.99	17.10	6.41	2.07	10.12	1.48	6.33	1.15	3.06	0.47	2.01	0.27
	1.71	7.49	1.39	7.98	3.37	1.03	5.08	0.57	2.61	0.38	0.91	0.10	0.48	0.07
	6.66	22.40	3.38	18.80	7.70	2.10	11.20	1.07	5.73	1.03	2.31	0.28	1.27	0.18
	6.50	19.05	2.70	12.86	4.42	1.05	6.11	0.80	4.48	0.89	2.08	0.29	1.60	0.23
	1.40	5.54	1.07	5.92	2.53	0.77	4.01	0.46	2.33	0.32	0.69	0.05	0.32	0.04
	3.37	16.62	2.98	17.60	6.58	1.94	9.73	1066	4.36	0.67	1.35	0.16	0.94	0.14
	4.83	19.70	3.25	19.30	8.80	2.31	12.10	0.99	4.90	0.91	1.59	0.18	1.07	0.11
	1.39	6.49	1.22	7.78	3.15	1.18	4.71	0.53	2.47	0.44	0.85	0.09	0.49	0.07
	10.14	34.20	5.56	31.70	12.80	3.43	17.30	1.99	9.16	1.49	3.49	0.43	1.93	0.27
	5.44	17.30	2.99	17.10	6.62	1.84	10.50	1.04	5.92	0.94	2.33	0.24	1.58	0.22
	4.02	12.23	1.69	8.73	3.85	1.15	5.60	0.76	4.04	0.70	1.76	0.24	1.47	0.18

Cem./Sam.	La (ppm)	Ce (ppm)	Pr (ppm)	Nd (ppm)	Sm (ppm)	Eu (ppm)	Gd (ppm)	Tb (ppm)	Dy (ppm)	Ho (ppm)	Er (ppm)	Tm (ppm)	Yb (ppm)	Lu (ppm)
	4.00	5.30	0.54	2.35	0.52	0.14	0.78	0.11	0.73	0.18	0.42	0.06	0.26	0.04
	4.06	5.65	0.55	2.24	0.42	0.16	0.95	0.13	0.85	0.20	0.56	0.08	0.37	0.05
	8.80	11.89	1.05	4.23	1.14	0.41	2.14	0.41	3.40	0.88	2.60	0.44	2.70	0.38
	8.29	9.78	0.83	2.83	0.63	0.17	1.21	0.15	1.01	0.21	0.51	0.07	0.45	0.05
Ferroan	8.40	13.95	1.44	6.01	1.25	0.42	1.86	0.32	2.02	0.41	1.00	0.13	0.73	0.13
Calcite S17	6.06	7.73	0.72	2.74	0.54	0.19	1.04	0.19	1.07	0.24	0.56	0.08	0.52	0.08
	11.40	18.20	1.85	6.50	1.20	0.27	1.55	0.18	1.36	0.29	0.78	0.08	0.40	0.08
	20.00	39.70	5.11	19.90	5.20	1.50	5.80	0.76	3.38	0.56	1.46	0.10	0.49	0.12
	5.44	7.00	0.61	2.27	0.47	0.16	1.02	0.15	1.02	0.21	0.58	0.05	0.38	0.05
	6.42	8.06	0.75	3.02	0.72	0.18	1.43	0.18	0.97	0.20	0.48	0.05	0.29	0.03
	8.22	15.20	1.86	7.42	1.64	0.35	1.75	0.22	1.40	0.24	0.61	0.09	0.49	0.08
	12.67	27.40	3.10	13.90	3.43	0.70	3.64	0.54	2.99	0.48	1.47	0.19	0.95	0.14
	12.00	25.00	3.03	13.40	3.09	0.67	3.35	0.43	2.59	0.46	1.06	0.16	0.88	0.14
	13.88	30.40	3.53	15.00	3.54	0.72	3.79	0.58	2.79	0.51	1.44	0.16	1.27	0.18
	16.00	34.70	4.23	17.80	4.19	0.96	4.48	0.63	3.66	0.69	1.91	0.25	1.48	0.20
Dolomite	14.17	31.50	3.76	16.04	3.98	0.82	4.26	0.60	3.31	0.62	1.77	0.21	1.29	0.20
S12	13.75	30.13	3.59	14.85	3.67	0.82	3.92	0.61	3.43	0.66	1.58	0.27	1.30	0.22
	16.17	36.60	4.32	18.04	4.71	1032	5.25	0.73	4.31	0.83	2.18	0.30	1.57	0.26
	11.22	22.53	2.60	11.07	2.70	0.56	2.99	0.37	2.03	0.39	1.06	0.18	0.84	0.15
	12.13	25.60	3.06	12.32	3.10	0.69	3.15	0.44	2.45	0.48	1.23	0.16	0.91	0.15
	13.11	28.50	3.31	14.30	3.66	0.75	3.82	0.56	3.34	0.63	1.64	0.22	1.34	0.20

Cem./Sam.	La (ppm)	Ce (ppm)	Pr (ppm)	Nd (ppm)	Sm (ppm)	Eu (ppm)	Gd (ppm)	Tb (ppm)	Dy (ppm)	Ho (ppm)	Er (ppm)	Tm (ppm)	Yb (ppm)	Lu (ppm)
	22.20	48.70	5.68	23.10	4.64	0.90	4.86	0.57	3.23	0.61	1.52	0.19	0.92	0.19
	18.36	40.00	4.73	18.68	4.53	0.90	3.72	0.55	2.97	0.55	1250	0.18	1.06	0.14
	18.47	41.16	4.73	18.38	4.07	0.81	3.48	0.48	2.54	0.45	1056	0.14	0.77	0.10
	19.10	43.10	5.06	20.10	4.87	1.05	5.00	0.68	3.44	0.77	2.07	0.34	2.08	0.32
Ferroan	15.47	33.50	4.08	16.72	3.78	0.81	3.42	0.46	2.81	0.46	1239	0.16	0.80	0.11
Dolomite	19.17	42.50	4.83	18.46	3.81	0.82	3.56	0.45	2.49	0.44	1.13	0.15	0.75	0.10
S12	18.16	41.93	4.54	17.59	3.72	0.76	3.03	0.43	2.28	0.40	1010	0.11	0.76	0.10
	27.28	58.60	6.79	27.44	6.39	1.37	5.74	0.82	4.00	0.68	1.67	0.20	1.14	0.13
	19.85	43.80	5.15	20.66	4.66	0.90	4.05	0.54	2.82	0.51	1.25	0.16	0.79	0.13
	18.05	41.20	4.69	17.41	3.64	0.67	3.14	0.44	2.12	0.39	0.93	0.13	0.66	0.11
	18.27	40.68	4.52	17.59	3.57	0.71	2.92	0.44	2.29	0.40	0.98	0.11	0.73	0.10
	11.73	44.50	7.58	40.30	13.10	3.44	15.22	2.07	9.46	1506	3.49	0.42	2.44	0.27
	13.26	51.80	8.77	48.10	17.29	4.23	18.90	2.42	12.03	1.92	4.27	0.50	2.59	0.41
	12.85	51.00	8.58	46.90	17.91	4.61	18.86	2.60	12.43	1.87	4.63	0.50	2.65	0.42
	12.73	46.80	8.28	42.60	15.21	3.82	16.76	2.17	10.79	1.60	3.68	0.42	2.32	0.29
	13.39	51.30	8.67	45.10	16.86	4.13	18.60	2.28	12.52	1.99	4.03	0.55	2.69	0.39
	12.73	47.60	7.93	42.50	15.40	3.67	16.41	2.12	11.95	1.80	4.00	0.44	2.47	0.37
Saddle	11.66	45.50	7.51	41.60	15.80	4.00	16.87	2.28	11.66	1.75	4.30	0.46	2.37	0.38
Ferroan	12.08	45.70	7.94	41.20	14.60	3.78	17.07	2.09	10.16	1.70	3.64	0.44	2.43	0.34
Dolomite	12.90	48.20	8.16	42.00	15.17	3.75	16.50	2.19	10.79	1.74	3.94	0.44	2.94	0.34
S10	14.42	53.60	8.93	45.80	16.29	4.04	17.21	2.34	12.68	1.95	4.46	0.49	3.13	0.44
	11.27	41.40	6.99	35.90	13.26	3.07	13.90	1.89	9.78	1.43	3.39	0.42	2.37	0.33
	14.21	53.30	9.31	50.20	18.55	4.72	21.38	2.85	13.58	2.15	4.53	0.56	3.13	0.41
	13.22	51.20	8.73	45.40	16.50	4.10	18.10	2.39	11.84	1.89	4.17	0.48	2.72	0.35
	11.86	43.20	7.45	38.60	13.67	3.37	14.92	1.98	9.12	1.48	3.25	0.37	2.09	0.31
	12.96	49.20	8.46	43.80	17.10	4.19	17.94	2.32	10.63	1.69	3.95	0.42	2.56	0.35
	12.41	46.40	7.66	40.30	13.74	3.58	15.65	2.05	10.73	1.84	4.06	0.47	2.63	0.38
	11.85	45.80	7.83	42.10	14.61	3.80	15.38	2.17	10.33	1.69	3.76	0.46	2.41	0.45

Cem./Sam.	La (ppm)	Ce (ppm)	Pr (ppm)	Nd (ppm)	Sm (ppm)	Eu (ppm)	Gd (ppm)	Tb (ppm)	Dy (ppm)	Ho (ppm)	Er (ppm)	Tm (ppm)	Yb (ppm)	Lu (ppm)
Siderite S16	28.20	102.00	10.30	46.90	14.70	4.14	19.40	2.57	17.20	3.18	8.10	1.40	6.97	1.32
	9.90	26.80	3.52	17.30	7.80	2.04	12.60	2.33	14.40	2.49	8.10	1.20	8.70	1.30
	15.00	47.00	6.11	29.60	12.20	3.42	18.60	3.11	19.20	3.73	9.60	1.36	8.90	1.39
	20.70	58.00	8.30	41.00	23.00	3.70	27.00	2.73	22.30	4.40	10.40	1.56	13.50	1.13
	24.50	65.00	7.70	33.00	10.90	2.88	13.80	2.24	16.70	3.28	9.40	1.75	7.60	1.39
	19.20	52.00	5.90	29.00	10.40	3.17	14.50	2.53	14.00	2.83	8.10	0.87	7.30	0.96
Siderite 10	3.30	7.20	1.05	5.38	2.12	0.57	3.37	0.41	1.94	0.35	1.14	0.11	0.73	0.13
	3.74	8.12	1.06	4.91	1.99	0.48	2.05	0.28	1.46	0.31	0.70	0.10	0.72	0.12
	3.27	7.83	1.18	5.38	2.60	0.62	2.69	0.36	1.98	0.40	0.89	0.14	0.84	0.15
	2.61	6.18	0.90	4.86	2.13	0.52	2.85	0.33	2.00	0.43	0.91	0.10	0.67	0.12
	2.41	5.43	0.86	4.52	1.98	0.54	2.53	0.33	1.56	0.31	0.87	0.10	0.62	0.08
	6.38	15.00	1.97	9.19	3.50	0.88	3.73	0.56	2.32	0.47	0.96	0.14	0.77	0.15
	2.42	5.54	0.92	4.45	2.32	0.62	2.63	0.31	2.07	0.30	0.89	0.12	0.91	0.11
	3.68	8.78	1.29	6.09	2.61	0.67	2.73	0.41	2.28	0.43	1.08	0.11	0.79	0.10
	2.86	6.17	0.83	4.26	1.98	0.54	2.46	0.33	1.71	0.33	0.99	0.11	0.64	0.12
	2.59	6.34	1.00	4.14	2.41	0.48	2.56	0.37	1.99	0.31	0.87	0.12	0.82	0.10
	3.84	9.20	1.33	6.03	2.21	0.66	2.61	0.32	1.62	0.34	0.83	0.13	0.58	0.15
	3.28	7.76	1.02	5.16	2.19	0.49	2.57	0.33	1.68	0.33	0.89	0.12	0.66	0.09
	4.25	9.98	1.51	7.30	3.25	0.75	3.48	0.48	1.83	0.38	0.91	0.11	0.75	0.13
	7.05	16.30	2.21	9.90	3.58	0.81	2.73	0.34	2.03	0.29	0.82	0.14	0.75	0.12
	4.13	10.31	1.57	6.56	2.50	0.60	2.71	0.36	1.89	0.24	0.84	0.11	0.72	0.07